

The Pennsylvania State University

The Graduate School

College of Engineering

**EXPERIMENTS IN HYDROGEN DISTRIBUTION IN THERMAL
GRADIENTS CALCULATED USING BISON**

A Paper in

Nuclear Engineering

by

John T. Merlino

© 2019 John T. Merlino

Submitted in Partial Fulfillment
of the Requirements
for the Degree of

Master of Engineering

April 2019

We approve the paper of John T. Merlino as fulfillment of the paper requirement of a Master of Engineering degree in Nuclear Engineering.

Date of Signature

Dr. Arthur T. Motta
Pennsylvania State University
Professor of Nuclear Engineering and Materials Science Engineering
Chair of the Nuclear Engineering Program

Dr. William J. Walters
Pennsylvania State University
Assistant Professor of Nuclear Engineering

Bruce F. Kammenzind
Naval Nuclear Laboratory
Manager, Core Structural Materials Technology

Abstract

In pressurized waters reactors, zirconium alloys are used as cladding to provide structural support for the fuel and prevent fission product release into the coolant. At the cladding-coolant interface, zirconium reacts with water to form zirconium oxide and hydrogen, some of which transports into the cladding and migrates as soluble hydrogen. This hydrogen preferentially diffuses in solid solution to areas of low concentration, low temperature, and high tensile stress. As the hydrogen concentration in a localized area increases, the zirconium matrix becomes supersaturated and zirconium hydrides precipitate out of solution. As hydrides form, strain fields are created and the zirconium matrix becomes more brittle.

The two experiment sets presented in this paper and modeled with the BISON code demonstrate the behavior of hydrogen in stress-free thermal environments. The first experiment set and corresponding simulations involve specimens with homogeneously-distributed hydrogen in a steep, linearly-increasing temperature gradient. The second experiment set and corresponding simulations involve specimens with a cathodically-plated hydride rim at one end in a shallow, asymmetric temperature gradient with a centralized peak temperature. The results of this paper not only provide much needed hydrogen diffusion and precipitation data for Zircaloy-4, Zircaloy-2.5% Niobium, and Zircaloy-1% Niobium, but also expand upon hypotheses explaining hydride precipitation. Specifically, scatter in the terminal solid solubility of precipitation data (hydrogen concentration at which the zirconium matrix is saturated) may indicate that this trend cannot easily be predicted, as precipitation kinetics, zirconium alloy microstructure, and temperature all strongly affect the ability of supersaturated soluble hydrogen to exist in the zirconium matrix. On the other hand, BISON uses mathematical models with empirically-determined constants to predict hydrogen behavior in zirconium alloys, and consistently over predicts the amount of hydrides in the coldest part of the specimen and under predicts the amount of hydrides in neighboring regions. This consistent mismatch between experimental and simulation results and the actual hydrogen distribution observed experimentally may indicate that hydrides can reach a point of saturation, in which the amount of hydrogen in solid solution must increase in order for additional precipitation to occur.

Table of Contents

1. Introduction.....	1
1.1. Hydrogen Presence during Manufacturing of Zirconium Alloys.....	3
1.2. Hydrogen Uptake	6
1.3. Hydrogen Diffusion.....	7
1.4. Hydride Precipitation and Dissolution Mechanics	9
2. Experimental Method	11
3. Hydrogen Distribution After Annealing.....	15
3.1. Experiment 1 Data Set.....	16
3.2. Experiment 2 Data Sets	21
4. Calculation of Hydrogen Distribution using BISON.....	24
4.1. BISON Model Setup	24
4.2. BISON Model Results.....	28
<i>4.2.1. Experiment 1 Data Models.....</i>	<i>28</i>
<i>4.2.2. Experiment 2 Data Models.....</i>	<i>43</i>
5. Conclusion and Future Work	48
6. Acknowledgments	49
7. Appendix A	50
8. References.....	71

1. Introduction

Currently in the United States, about 20% of the electrical energy is produced via nuclear reactors [1]. During energy production, thermal neutrons primarily interact with the uranium-235 of the nuclear fuel, which can create an unstable isotopic state, split uranium into two or more fission products, free additional neutrons, and release energy proportional to the difference in masses between the reactants and the products. The heat from nuclear fission is then transferred to the coolant, which is used to expand a working fluid through a turbine generator for energy production [2].

In commercial light water nuclear power plants, fuel is in the form of ceramic uranium dioxide pellets that are about 1 centimeter in diameter by 1 centimeter in length and enriched to about 3-5% fissile uranium-235. Hundreds of fuel pellets are stacked and sealed in a zirconium alloy tube that is backfilled with helium to create a four or five-meter-long fuel rod. The zirconium alloy tube is hundreds of micrometers thick and forms the cladding that supports the fuel pellets and prevents the release of radioactive fission products to the coolant. A standard pressurized water reactor has hundreds of fuel bundles (e.g., 193 bundles per core), each composed of hundreds of fuel rods arranged in a square pattern (e.g., 17 x 17 rods per bundle) [3]. In order to support the fuel bundle (broken down in Figure 1), maximize heat transfer from the fuel to the coolant by promoting turbulent flow with swirl veins, and provide structural integrity by limiting the amplitude of vibrations, fuel rods pass through structural zirconium alloy spacer grids that are positioned every couple of feet along the height of the core. In pressurized water reactors, coolant temperatures range from 270°C to 330°C and mass flow rates reach thousands of kilograms per second [4].

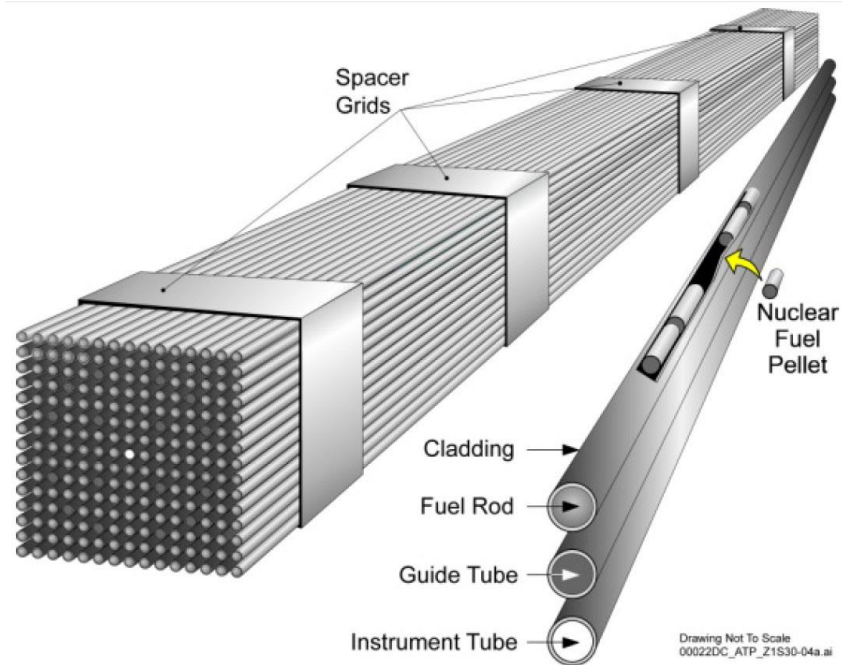


Figure 1: Schematic of standard pressurized water reactor fuel bundle [5].

As a result of the thin, long, and numerous fuel rods in combination with the high operating temperatures, pressures, flow rates, and neutron fluxes, the nuclear core needs to be designed in such a way that minimizes plastic deformation and fission product release both in normal operations and disposal. The ceramic uranium dioxide fuel pellets are fabricated with high strength to limit deformation from both gaseous and nongaseous fission product buildup. The helium-filled gaps between adjacent fuel pellets and between the fuel pellets and the cladding promote heat conduction, allow for detection of primary coolant leakage, and provide additional space for fuel pellet growth. The zirconium alloys used in cladding and core structural materials provide good mechanical properties, resistance to high-temperature corrosion, and low neutron cross sections to promote neutron use for fission [6].

Reactor stresses during normal operation and dry storage are of particular importance for the fuel cladding, which serves as the primary boundary between fission products and the environment, and the effects can be observed on both the microscopic and macroscopic levels throughout core lifetime. On the microscopic level, irradiation damage caused by neutron interaction with the zirconium matrix results in a harder, more brittle cladding from atomic displacement, dislocation loop entanglement, and intermetallic particle precipitation [7]. At the same time, continual fast neutron-induced movement of the zirconium matrix in elevated temperatures can lead to ductile effects such as creep and growth. Finally, primary coolant interaction with the zirconium alloy surface results in a slow, uniform zirconium oxide corrosion layer buildup. As a part of the corrosion process, hydrogen is absorbed into the corroding material. Once in the cladding, hydrogen diffuses in solid solution to areas of lower hydrogen concentrations, lower

temperatures, and higher localized tensile stresses. At the critical solubility concentration of a given location, hydrogen precipitates out of solid solution to form zirconium hydride particles, which embrittle the cladding, decrease fracture toughness, create localized stress-strain fields from an increased hydride volume, and increase the potential for crack propagation [8]. These mechanical property effects on the cladding microstructure need to be considered when accounting for the macroscopic thermal and mechanical-induced stresses seen by the core. During normal operation, macroscopic stresses result from temperature gradients, flow-induced vibrations, and variations in fuel and cladding growth. While in service, pressure buildup internal to the fuel cladding is counteracted by the pressure of the coolant surrounding the cladding; however, during extended dry storage, hoop stresses develop in the cladding from the internal pressure created by decay heat and the pressure differential created by the vacuum drying process [9].

Since technology of the 1970s, fuel rod material and modeling improvements have allowed for fuel burnup levels to increase from 30 to around 60 gigawatt-days per metric ton of heavy metal uranium [10]. With this increase in fuel utilization, the core can see fluence levels of more than 10^{22} neutrons per square centimeter and cladding oxide thicknesses of around 100 micrometers (approximately 15% of the through-wall cladding thickness) [8]. Although experimentation shows that the cumulative rate at which irradiation damage affects the mechanical properties of the cladding greatly decreases after about a month of service, corrosion layer buildup continues throughout the core life [11]. Furthermore, the rate of hydrogen pickup increases as the oxide layer thickness increases and varies with the type of zirconium alloy used [12]. Finally, brittle hydrides more readily precipitate as the bulk concentration of hydrogen increases.

Prior to core operation, the hydrogen concentration of the fabricated cladding tube is on the order of ten parts per million by weight (wt. ppm). At the end of the core life, average through-thickness hydrogen concentration increases on the order of 800 wt. ppm can occur, depending on the cladding alloy and its service environment [13]. As longer core lives are pursued and cladding hydrogen concentrations increase, additional material examinations and model improvements are needed to increase understanding of the behavior of hydrogen, limitations that exist due to hydrogen, and effects of hydrogen on mechanical properties and cladding integrity. It can be assumed that some hydrogen will always migrate into the cladding. This paper explores the fundamental behavior of hydrogen once in the cladding in stress-free thermal gradients and compares simulations generated by the BISON code with physical experimentations to understand where model improvements may be useful for commercial applications.

1.1. Hydrogen Presence during Manufacturing of Zirconium Alloys

Zirconium alloys are studied and implemented in industry based on compromise between corrosion resistance, strength, manufacturability, and cost. Although boiling water reactors

primarily use nickel-containing Zircaloy-2 because of its superior corrosion resistance to steam and nodular corrosion, pressurized water reactors primarily use claddings more similar to Zircaloy-4 due to its comparable corrosion-resistant properties and its decreased propensity to uptake hydrogen. Zircaloy-4 contains 0.18-0.24 weight-percent (w/o) iron, 0.07-0.13 w/o chromium, and 1.2-1.7 w/o tin. In an effort to further increase corrosion resistance, improve strength, and decrease hydrogen uptake, tin concentrations have been decreased in applications such as Westinghouse's ZIRLO cladding (zirconium low oxidation) and niobium additions have been studied and implemented in separate cladding applications such as CANDU (Canadian Deuterium Uranium) reactors [14].

At temperatures below 810°C, Zircaloy-4 exists in the alpha phase, which has a hexagonal-close packed (hcp) atomic structure. As a result of this hcp structure where the c-axis length is longer than the a-axis length, Zircaloy-4 exhibits preferential crystallographic orientation and anisotropic mechanical properties due to the texturing that occurs during cold working [15]. As a result of the pilgering processes in cladding manufacturing, the crystallographic zirconium atomic structure is oriented with the c-axis pointed in the radial direction such that under stress-free conditions hydrides precipitate and coalesce in the circumferential direction [16]. This orientation occurs because zirconium hydride most often precipitates in the stable face-centered cubic-delta phase, $ZrH_{1.6}$, which forms as a disc along the basal plane of the zirconium alloy matrix [17]. As seen in post-irradiation metallography examinations involving microstructure analysis using chemical etching, these hydride discs are known to overlap along the colder, outer circumference of the cladding to form long platelets in conjunction with the textured zirconium matrix. These hydride platelet strands along the colder regions of the cladding form what is known as the hydride rim, shown in Figure 2 [18].

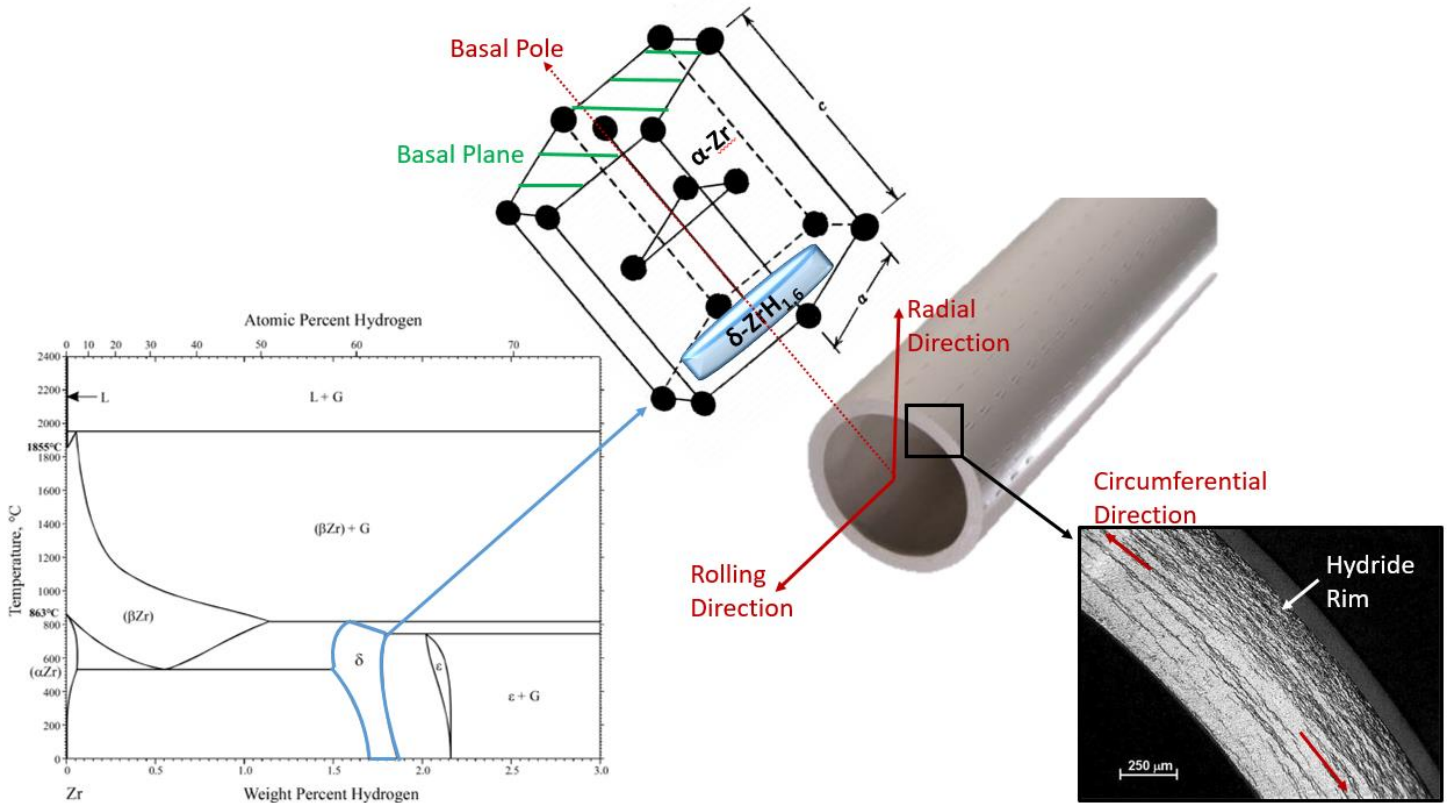


Figure 2: This schematic displays the circumferential direction along the curvature of the cladding, the radial direction through the wall of the cladding, and the rolling direction along the length of the cladding. The preferred circumferential orientation of precipitated hydrides occurs when the basal pole and basal plane of the zirconium alloy are in the radial and rolling direction, respectively. Platelets of the hydride rim are formed from overlapping hydrides, which are most often observed in the delta phase.

Under post-service conditions such as dry storage, hoop stresses and temperatures can increase such that in-service circumferential hydrides can dissolve and subsequently re-precipitate normal to the stress direction as cooling occurs over time. At these threshold stress values, hydrides can preferentially orient in the radial, vice circumferential, direction [9]. As hydrides grow and coalesce in the radial direction, brittle fracture and delayed hydride cracking (DHC) in a through-wall manner become a concern. During the DHC process, hydrogen in solid solution migrates to areas of high hydrostatic stress which occur at an existing crack tip, a localized terminal solubility is reached, and hydrides precipitate out of solution embrittling the material at the crack tip [19]. This process propagates the crack and attracts more hydrogen in solid solution.

Although radially-oriented zirconium hydride particles and through-wall crack propagation are primary concerns in regards to cladding failure, a greater fundamental understanding of hydrogen diffusion and precipitation in stress-free environments is needed to better model the entire lifecycle of hydrogen in cladding and subsequent effects of stress.

1.2. Hydrogen Uptake

Hydrogen can enter the cladding and exist in solid solution as a result of two processes. In both of these processes, hydrogen ions (H^+) are created and have the potential to combine with electrons or hydroxide ions (OH^-) in the water outside of the cladding, combine with electrons in the oxide layer, or diffuse across the zirconium oxide layer to combine with electrons in the base metal. If hydrogen ions manage to diffuse across the zirconium oxide layer, hydrogen, at least initially, exists in solid solution and resides in interstitial sites of the zirconium lattice [20].

The first process that creates hydrogen ions is the radiolysis of water. During radiolysis, water separates into H^+ and OH^- as a result of neutron or gamma ray interaction. Overall, the hydrogen ions that are formed from water radiolysis contribute to practically no hydrogen uptake in the cladding because of the high probability of hydrogen ion interaction prior to reaching the oxide layer [21].

Therefore, the primary mechanism that contributes to hydrogen uptake in the cladding is the oxidation of the zirconium shown in Equation 1. During the formation of the corrosive zirconium oxide layer, hydrogen ions are created at the water-oxide interface, and about 10-20% of which diffuse into the cladding.

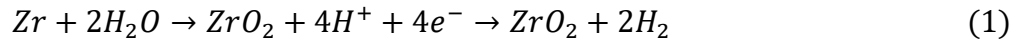


Figure 3 shows how the thickness of the oxide layer affects hydrogen uptake [12]. This data demonstrates that thicker oxide layers lead to increased rates of hydrogen uptake. Here, the weight gain measurement accounts for introduction of oxygen to the zirconium alloy, is proportional to the oxide layer thickness, provides an average of the oxide layer thickness, and does not involve specimen sectioning and metallography work. This figure also demonstrates that different zirconium alloys lead to varying amounts of hydrogen uptake [22]. To explain this observation, it is hypothesized that hydrogen ions can more easily travel across zirconium oxide layers with lower electrical conductivities due to the decreased probability of electron interaction [20].

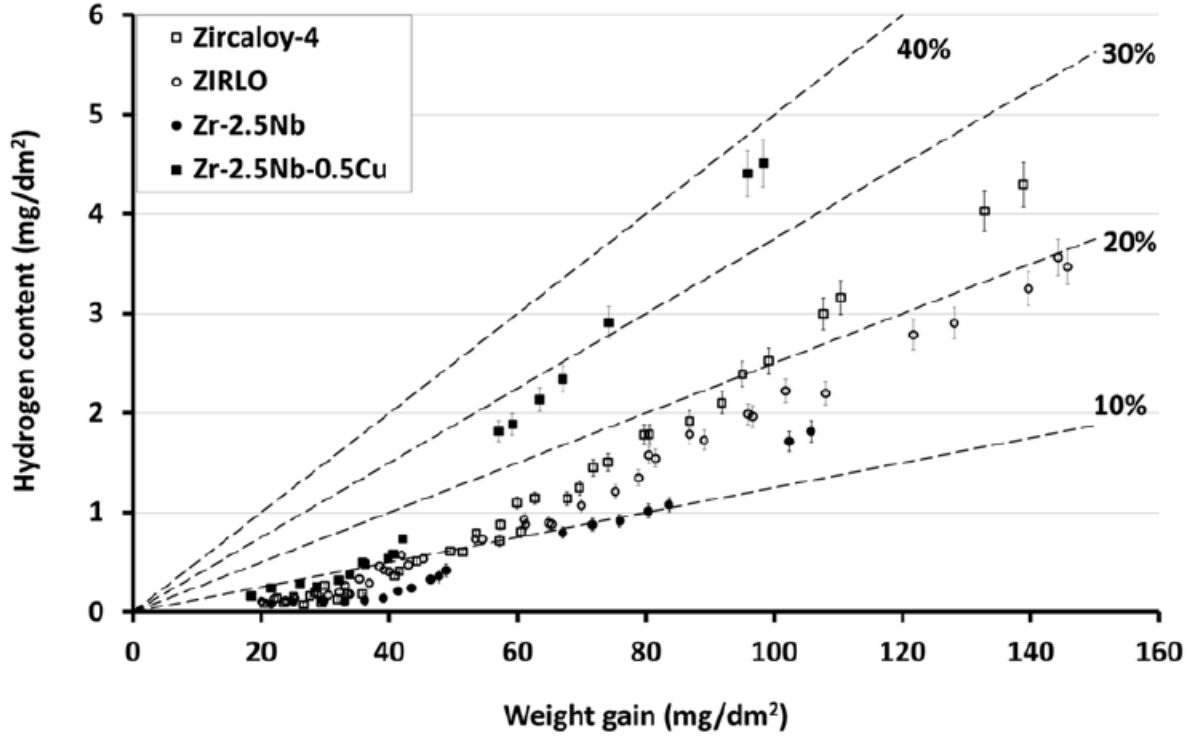


Figure 3: Hydrogen content as a function of corrosion weight gain when tested in an autoclave at 360°C [12]. The rate of hydrogen uptake increases as the oxide layer thickness increases, which needs to be considered when extending the life of fuel.

1.3. Hydrogen Diffusion

As stated above and explained mathematically in Equation 2, once in solid solution in the base cladding, hydrogen diffuses from areas of high concentration to low concentration per Fick's Law, from areas of high temperature to low temperature per the Soret Effect, and from areas of low tensile stress to high tensile stress [23]. In this equation, J represents hydrogen flux due to various driving forces.

$$J_{Diffusion} = J_{Fick} + J_{Soret} + J_{Stress} = -D\nabla C_{ss} - \frac{DC_{ss}Q^*}{RT^2}\nabla T + \frac{DC_{ss}V_H}{RT}\nabla\sigma \quad (2)$$

The first term, J_{Fick} , describes hydrogen flux due to the concentration of hydrogen in solid solution (C_{ss}), which behaves the same way as gases diffusing through air [24]. The diffusion coefficient (D) of hydrogen in a zirconium alloy describes how readily hydrogen disperses, is a function of temperature, and can be determined with the Arrhenius equation shown in Equation 3. The gradient is a vector derivative that points in the direction of greatest increase for a given function, here hydrogen concentration. As a result, J_{Fick} is negative because hydrogen will diffuse opposite of the gradient direction.

$$D = A_D \exp\left(-\frac{Q_D}{RT}\right) \quad (3)$$

As shown in Equation 3, the diffusion coefficient has the same dependence on temperature as a generic reaction rate. Here, R is the universal gas constant equal to 8.3145 J/(mole*K) and T is the temperature in Kelvin. Likewise, A_D is the diffusion frequency factor with units of cm²/s and Q_D is the diffusion activation energy with units of J/mole. The values of A_D and Q_D can be determined experimentally by obtaining a specimen, charging half of the specimen with a homogeneous distribution of hydrogen, ensuring the other half of the specimen has no hydrogen, annealing the specimen at an elevated temperature to confirm the hydrogen is in solid solution, measuring and plotting hydrogen concentrations along the length of the specimen as a result of diffusion during the annealing time, and determining the equation of the slope at the position of the original hydrogen/no-hydrogen interface [25].

The second term, J_{Soret} , describes hydrogen flux due to a temperature gradient. This term is also negative because hydrogen particles will diffuse opposite of the direction of the temperature gradient towards the colder regions, in the same way that the driving force, heat, flows from hot to cold [26]. In this term, Q^* is the heat of transport in J/mole, which describes how much energy in the form of heat is needed to drive hydrogen diffusion.

The third and final term, J_{Stress} , describes the tendency of hydrogen to redistribute to areas of high tensile stress, which usually involves stress concentrators such as a crack tip or a notch [27]. Here, V_H is the partial molar volume of hydrogen in the zirconium matrix and σ is the applied hydrostatic stress. Because the experiments and simulations presented in this paper were done under stress-free conditions, this term is zero and will not be considered to attribute to hydrogen diffusion.

Therefore, the final equation to describe hydrogen diffusion in a stress-free environment is $J_{\text{Diffusion}} = J_{\text{Fick}} + J_{\text{Soret}}$. In a specimen containing homogeneously-distributed hydrogen introduced to a temperature gradient, hydrogen in solid solution will gradually migrate to the colder side. This hydrogen diffusion induced by heat flow causes a concentration gradient to develop, which creates counterbalance driving forces that increase until the system eventually reaches equilibrium. At equilibrium, the distribution of hydrogen in solid solution in the zirconium alloy can be described by Equation 4 [25].

$$C_{ss} = C_o \exp\left(\frac{Q^*}{RT}\right) \quad (4)$$

In Equation 4 and the experiments discussed in this paper, temperature changes with position of the specimen, and hydrogen concentrations depend on the temperature profile. Once hydrogen

precipitates, the resulting zirconium hydride becomes integral to the zirconium atomic structure and can no longer freely diffuse while in this form [28].

1.4. Hydride Precipitation and Dissolution Mechanics

Once the concentration of hydrogen in a localized area reaches saturation, zirconium hydride particles precipitate out of solution. This concentration, the terminal solid solubility of precipitation (TSSp), primarily depends on temperature but can also be affected by irradiation damage and microstructure factors such as grain boundaries, alloying elements, and internal stresses [29]. Values of TSSp range from less than 1 wt. ppm at room temperature to around 100 wt. ppm at an average coolant temperature of 300°C [30]. Similarly, at the terminal solid solubility of dissolution (TSSd), zirconium hydride particles are in abundance, will dissociate, and hydrogen will dissolve back into solid solution in the zirconium matrix. As shown in Figure 4, the values of TSSp are greater than the values of TSSd. This hysteresis effect exists because at a given temperature, more energy and, therefore, a higher concentration of hydrogen is needed for precipitation to occur due to the 17% volume increase [25] associated with creating zirconium hydride [31].

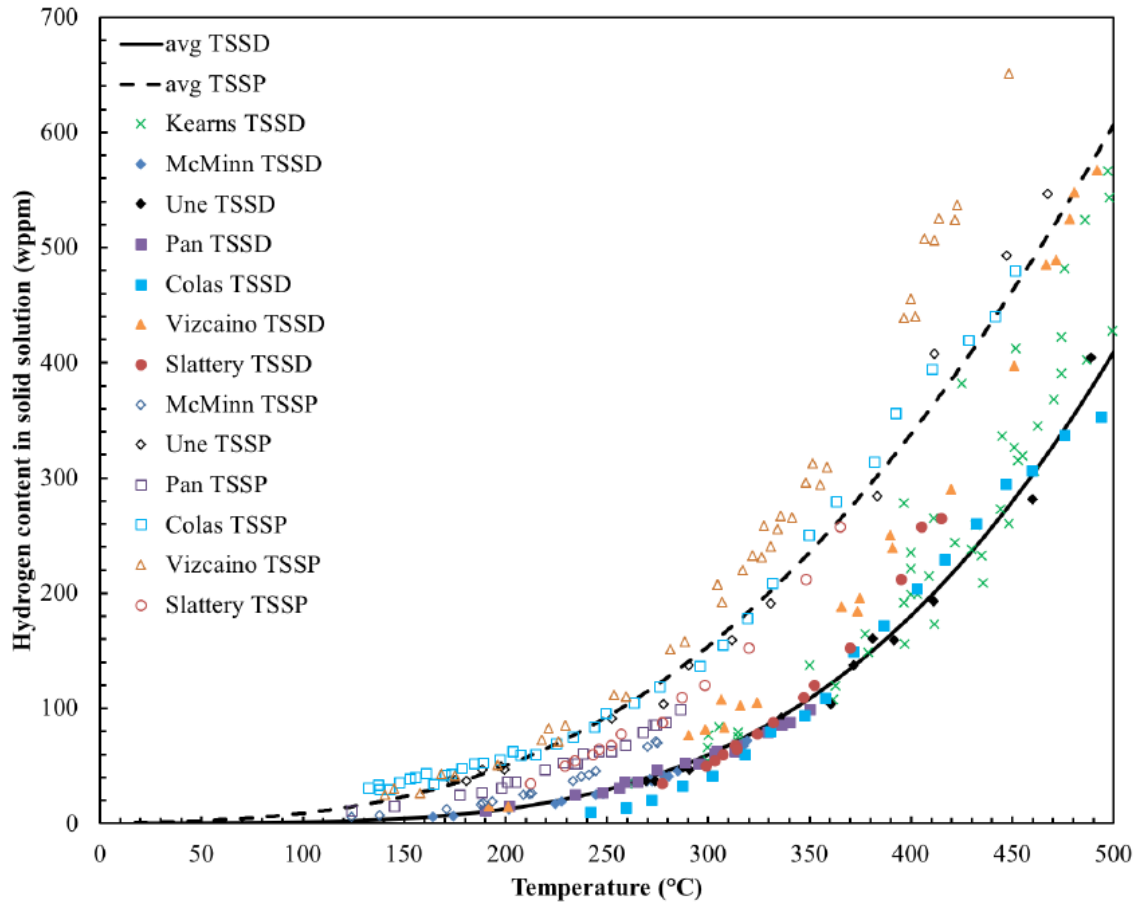


Figure 4: Experimental values of TSSp and TSSd based on a literature review [24] [30] [32] [33] [34] [35].

Figure 4 represents equilibrium conditions for TSSp and TSSd where the curves can be described by the Arrhenius formulas of Equations 5 and 6.

$$TSS_p = A_p \exp\left(-\frac{Q_p}{RT}\right) \quad (5)$$

$$TSS_d = A_d \exp\left(-\frac{Q_d}{RT}\right) \quad (6)$$

Important observations to note are that hydrogen diffuses from hot to cold and that TSSp decreases as temperature decreases. Therefore, it is expected and observed that hydrides precipitate to form the hydride rim in the coldest portions of the cladding near the interface of the cladding and the coolant [36]. However, by only considering the equilibrium equations above, hydrides would be expected to precipitate out of solution almost immediately upon entering the cladding and little hydrogen would be expected to diffuse into the cladding towards the fuel. To better reflect reality where hydrogen is observed in the hotter regions of the cladding, kinetic equations are needed to account for the transient behavior of hydrogen in supersaturated and subsaturated solid solution [13]. The rate of precipitation and dissolution are provided in Equations 7 and 8, where the constants are determined empirically and follow the same Arrhenius law described in previous formulas. Of these reaction rates, dissolution kinetics occur much faster than precipitation kinetics.

$$R_{Precipitation} = \alpha^2(C_{ss} - TSS_p); \quad \alpha = A_\alpha \exp\left(\frac{Q_\alpha}{RT}\right) \quad (7)$$

$$R_{Dissolution} = \beta^2(TSS_d - C_{ss}); \quad \beta = A_\beta \exp\left(\frac{Q_\beta}{RT}\right) \gg \alpha \quad (8)$$

The differential equations that describe precipitation and dissolution kinetics depend on localized hydrogen concentration. Equation 9 describes hydrogen supersaturated in solid solution (the portion of Figure 4 above TSSp). In this case, the time rate of change of hydrogen in solid solution is a result of the rate of precipitation and the net hydrogen diffusion flux.

$$C_{ss} > TSS_p \rightarrow \frac{C_{ss}}{dt} = -\alpha^2(C_{ss} - TSS_p) - \nabla J_{Diffusion} \quad (9)$$

Equation 10 describes a hydrogen concentration between TSSp and TSSd, where neither precipitation nor dissolution occurs. In this case, the time rate of change of hydrogen in solid solution is only dependent on the hydrogen flux due to temperature and concentration.

$$TSS_p \geq C_{ss} > TSS_d \rightarrow \frac{dC_{ss}}{dt} = -\nabla J_{Diffusion} \quad (10)$$

Equation 11 describes a hydrogen concentration below TSSd, where dissolution will occur if any hydrides are present. In this case, the time rate of change of hydrogen is a result of the rate of hydrides dissolving into solid solution and the net hydrogen diffusion flux. If no hydrides are present, the dissolution term is zero [13].

$$TSS_d \geq C_{ss} \rightarrow \frac{dC_{ss}}{dt} = \beta^2(TSS_d - C_{ss}) - \nabla J_{Diffusion} \quad (11)$$

Under normal operations, the processes involved with hydrogen uptake, hydrogen diffusion, and zirconium hydride formation can be summarized by Figure 5.

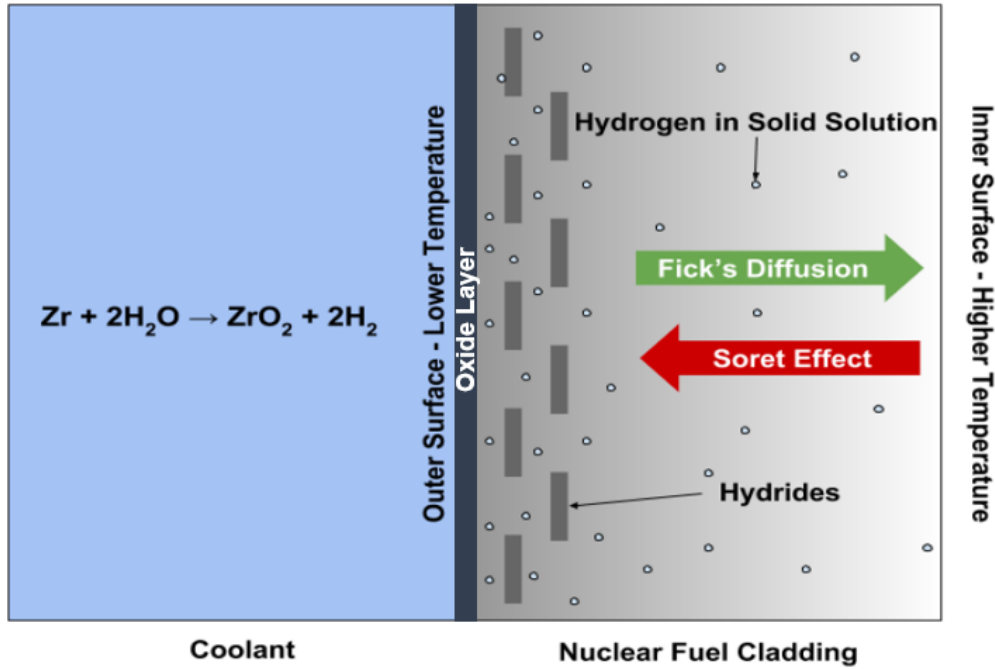


Figure 5: Summary of mechanisms for migration, redistribution, and morphology of hydrogen in zirconium alloy cladding.

2. Experimental Method

The two experiments of hydrogen diffusion and precipitation discussed in this paper were conducted by Kammenzind around the same time as the experiments presented in [25] and have not yet been published. In both of these experiments, specimens containing various amounts of hydrogen were annealed while subjected to various temperature gradients. The anneals were conducted for periods of time ranging from weeks to months in order to approach equilibrium. The specimens were then removed from heat, sectioned, and analyzed for total hydrogen content

as a result of hydrogen redistribution and precipitation. The unirradiated zirconium alloys investigated include alpha-annealed Zircaloy-4 (specimens identified as AXX), Zircaloy-1% Niobium (specimens identified as BXX), and Zircaloy-2.5% Niobium (specimens identified as CXX). Note that these specimens were created by cutting larger specimens in half. If both halves were analyzed, then the specimen identifier ends in an “a” or a “b”.

The first experiment set included twenty-eight rectangular specimens, each measuring 2.54 cm long, 1.27 cm wide, and 0.127 cm thick. The specimens were precharged with homogeneously-distributed hydrogen using a process similar to that described in [37], as shown in Figure 6. In order to precharge a specimen, the specimen was weighed, and placed in a quartz bulb with a pre-weighed amount of zirconium hydride chips. The amount of zirconium hydride chips put into the bulb depended on the weight and desired hydrogen content of the specimen at final system equilibrium. A vacuum was drawn on the bulb, and the bulb was then flushed with argon, re-evacuated, and sealed. The bulbs containing Zircaloy-4 specimens were annealed at 600°C for 8 hours, allowing hydrogen from the zirconium hydride chips to transfer as a gas to the Zircaloy specimen until an overall system equilibrium was reached. The bulbs containing Zircaloy-niobium specimens were annealed at 565°C for 27 hours to stay below the monotectoid temperature. At the end of the annealing process, the bulbs were quickly furnace cooled to prevent further hydrogen migration.

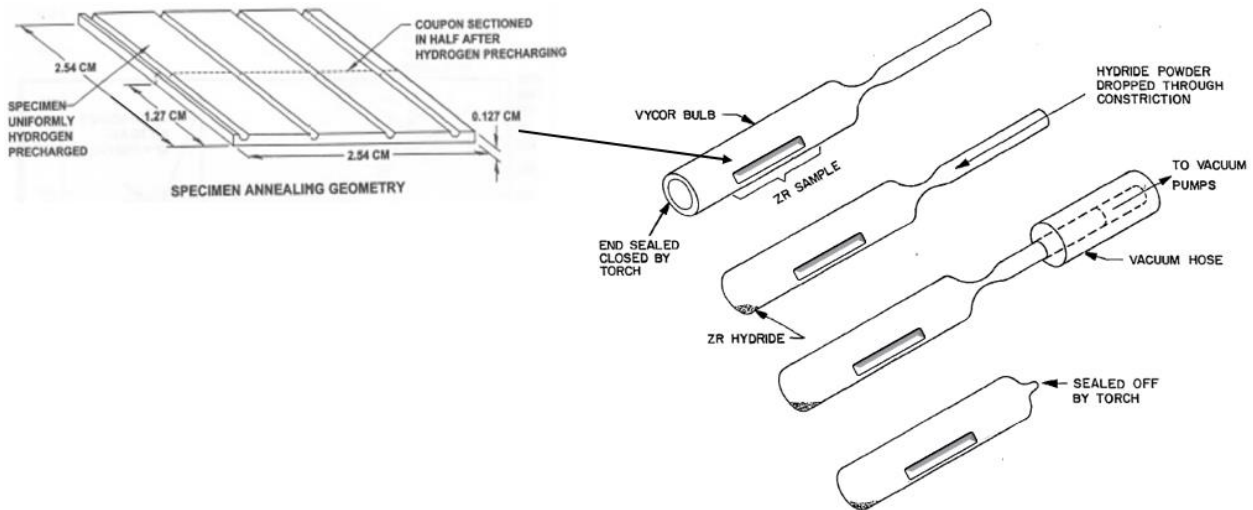


Figure 6: Experiment 1 setup to homogeneously precharge specimens with hydrogen.

Once all of the specimens were precharged with a homogeneous distribution of hydrogen, two specimens at a time were annealed in a linear thermal gradient with the setup shown in Figure 7. The specimen temperatures were directly measured with four to eight thermocouples that were positioned in the four slots of the specimens at distances of 0.089 cm, 0.838 cm, 1.676 cm, and 2.451 cm from the cold end. The cold end of the specimens was targeted at either 260°C, 316°C, 371°C, or 427°C, and the rate of temperature increase was targeted at either 66°C/cm or

87°C/cm. The annealing time for experiment 1 specimens ranged from about ten to eighty days depending on the overall specimen temperature, as less time for diffusion was needed as specimen temperature increased. The initial hydrogen concentration of each specimen was targeted to be below TSSp for the lowest specimen temperature.

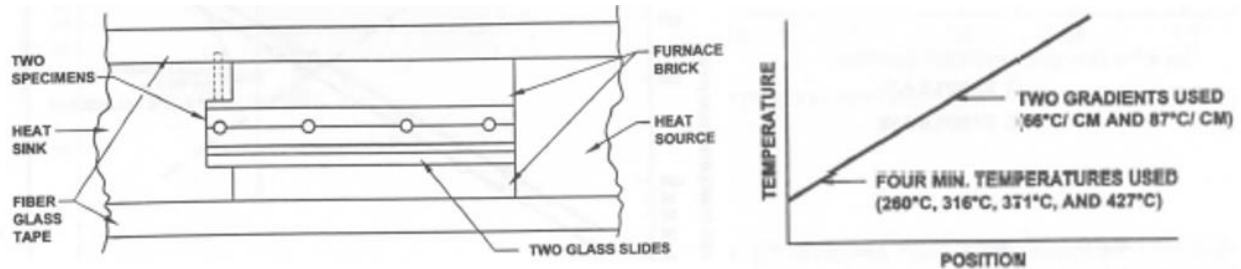


Figure 7: Experiment 1 setup for annealing in a linear temperature gradient.

The second experiment set included five rectangular specimens that were annealed in a setup similar to experiment 1, each measuring 3.81 cm long, 1.27 cm wide, and 0.127 cm thick. However, during this set of experiments, the annealing temperature gradient did not increase linearly but had a colder side temperature of either 260°C or 316°C, a peak temperature of 371°C about 2.54 cm from the colder side, and a hotter side temperature at the opposite end of the specimen with a temperature between the colder side and the peak temperature. Likewise, instead of being homogeneously distributed with hydrogen, these specimens were plated with a hydride rim on the hotter end of the specimen. Similar to the process described in [38], the hydride rim was precipitated onto the specimens by using a cathodic reaction at a current of 100 milliamps/cm² in a 1 Normal H₂SO₄ solution at 80°C, where the zirconium alloy was the cathode and platinum was the anode. Each specimen's hydride rim was about 75 micrometers thick, coating approximately the last one millimeter of the hotter end of the specimen. In order to control the location of the plating, the remainder of the specimen was covered in a lacquer coating to electrically insulate the hydrogen-free areas of the specimen during the cathodic process. In this experiment set, temperatures were measured at ten locations along the specimens with approximately fifteen thermocouples. The position of these thermocouples and an example temperature profile is given in Figure 8. Because the heavily concentrated hydride rim needed to dissolve into solid solution before any further redistribution and precipitation could take place and diffusion had to occur across a distance of approximately 3.8 cm in the same direction as the local temperature gradient, these specimens were annealed for periods between 100 and 200 days.

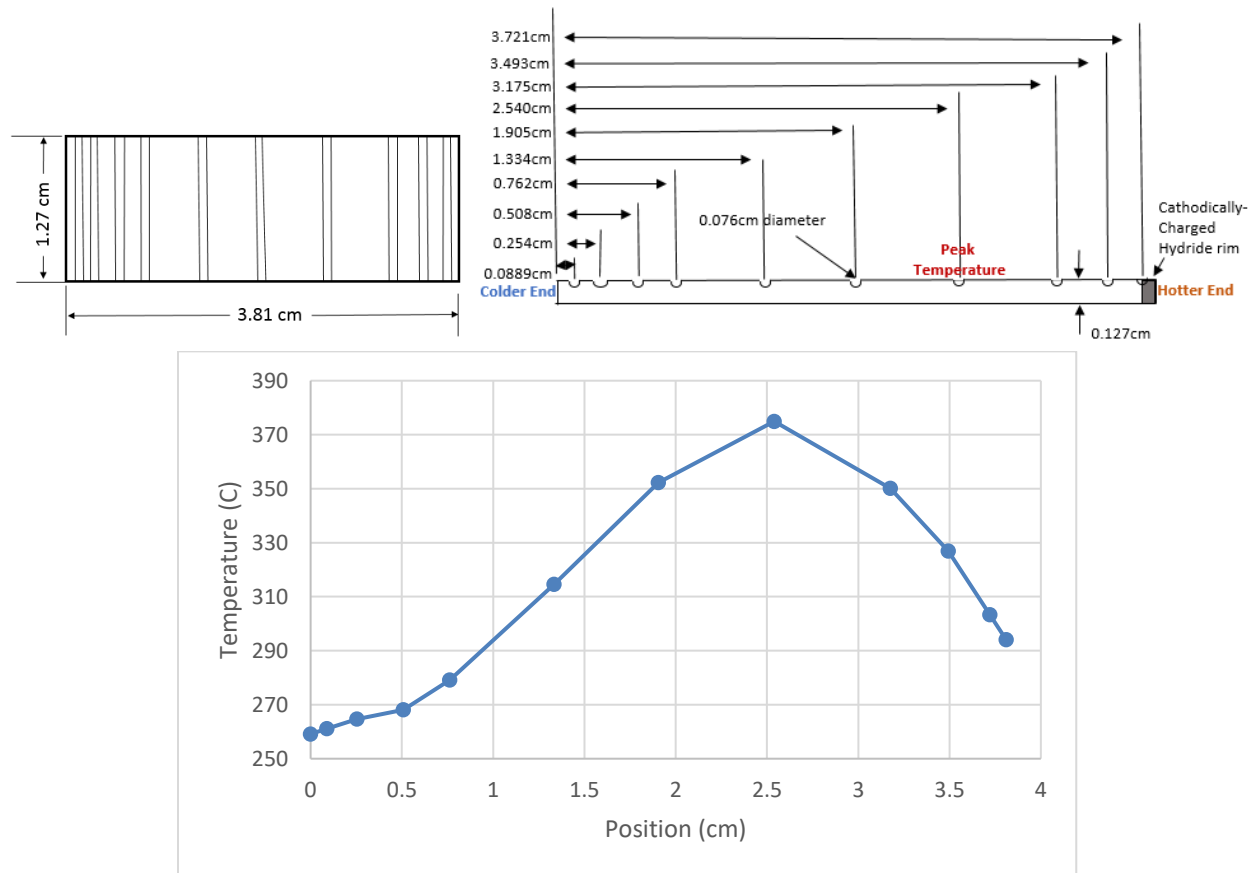


Figure 8: Experiment 2 thermocouple positions and example asymmetric temperature distribution. This experiment can be used to understand hydrogen behavior in a strong concentration gradient with a thermal gradient acting in the opposite direction.

Following annealing for both sets of experiments, the specimens were brought to room temperature to cause zirconium hydride precipitation and fix the hydrogen distribution. The specimens were then sectioned into eight to thirteen samples for the experiment 1 data set, and nineteen or twenty samples for the experiment 2 data set for hydrogen concentration analysis. The total hydrogen concentration (hydrides plus hydrogen in solid solution) for each sample was determined by LECO (Laboratory Equipment Corporation) analysis. LECO analysis is used to measure combustion gases such as carbon, sulfur, oxygen, nitrogen, or hydrogen in a metallic sample. For hydrogen, LECO relies on gas fusion in a graphite crucible under a flowing Argon gas stream, and the measurement of combustion gases by infrared absorption and thermal conductivity. During fusion, oxygen combines with carbon to form CO_2 , which is filtered out with other gases so that only hydrogen volume is measured. By knowing the volume of each sample, the volume of hydrogen gas can then be related to a hydrogen concentration at the center of the sample. Figure 9 shows the sectioning patterns for both experiment 1 and experiment 2 specimens.

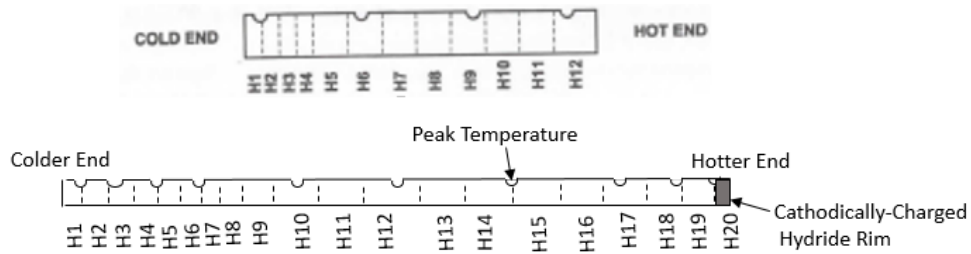


Figure 9: Upper sectioning template shows samples for experiment 1 data set and lower sectioning template shows samples for experiment 2 data set.

3. Hydrogen Distribution After Annealing

As stated previously, specimens from experiments 1 and 2 were annealed two at a time. In Appendix A, data is presented in tables based on annealing runs. Each table is prefaced by thermocouple data and provides specimen and sample identifiers, the length of each sample post sectioning, the location of the midpoint of each sample as it relates to the assembled specimen (note that this location must account for the amount of material removed by the sectioning process), the specimen temperature at each sample's midpoint location, and the hydrogen concentration of the sample as determined by LECO analysis. Although thermocouples provided continuous measurements, temperatures were recorded hourly and only averaged values are used for data analyses. All sample midpoint temperatures are linearly interpolated based on the previous and subsequent average thermocouple temperatures.

From the data provided in Appendix A, one can graph hydrogen concentration (wt. ppm) as a function of inverse temperature ($1/K$) at each sample's midpoint to understand the effect of temperature on hydrogen migration and morphology. The section of the graph that behaves exponentially corresponds to the distribution of hydrogen in solid solution and can be described by Equation 4. Furthermore, by using a least squares fit of this data, Equation 4 can be used to determine the heat of transport, Q^* , for each specimen by multiplying the number in the exponential by the universal gas constant, R . At lower temperatures (higher inverse temperature values), hydrogen concentrations in the samples are higher and no longer follow the exponential trend because hydrogen exists both in solid solution and as hydrides. The point at which precipitation begins can more easily be identified if hydrogen concentration is graphed on a logarithmic scale so that the exponential portion of the data appears linear. The first data point that breaks away from the exponential trend can be used to denote the first time that hydrides were present during the high-temperature anneal. At this corresponding temperature, TSSp can be inferred by using Equation 4 to extrapolate to the amount of hydrogen that was present in solid solution as precipitation occurred at temperature, under the influence of the thermal gradient.

Because the values of Q^* may vary slightly with annealing temperature and zirconium alloy composition, data is provided based on specimen cold side temperature for both Zircaloy-4 and Zircaloy-niobium alloys.

3.1. Experiment 1 Data Set

Figures 10 – 13 and Table 1 present diffusion and precipitation data for specimens involved with experiment 1.

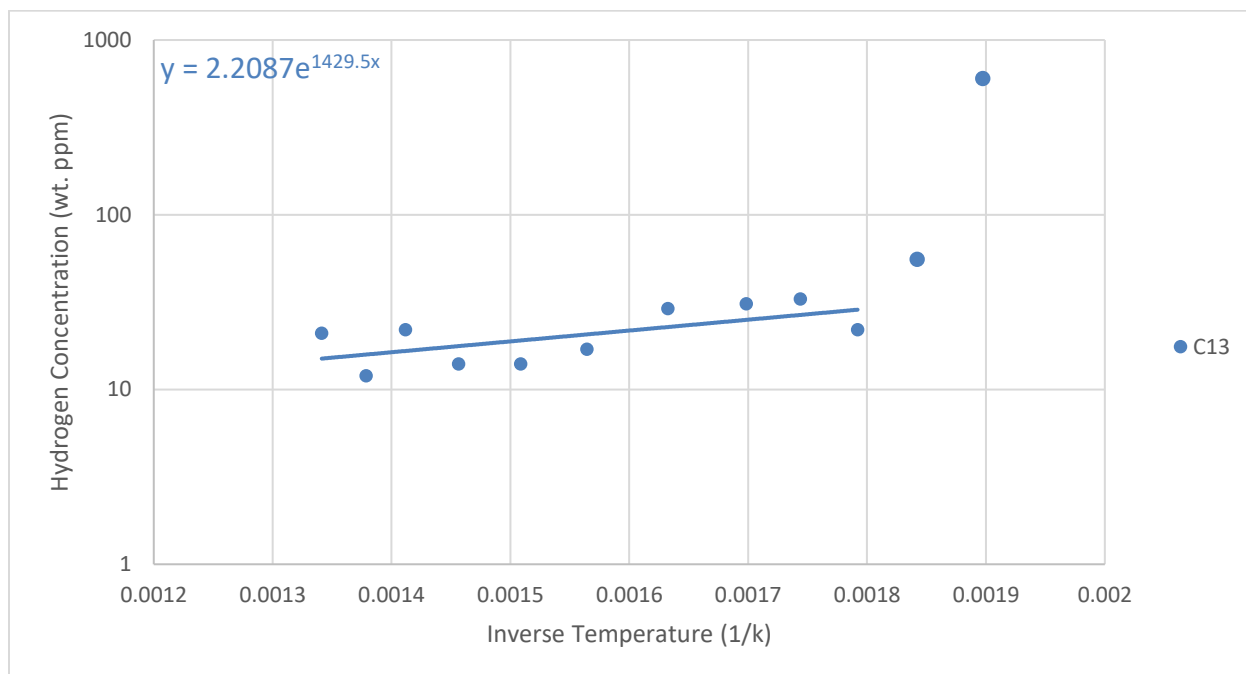
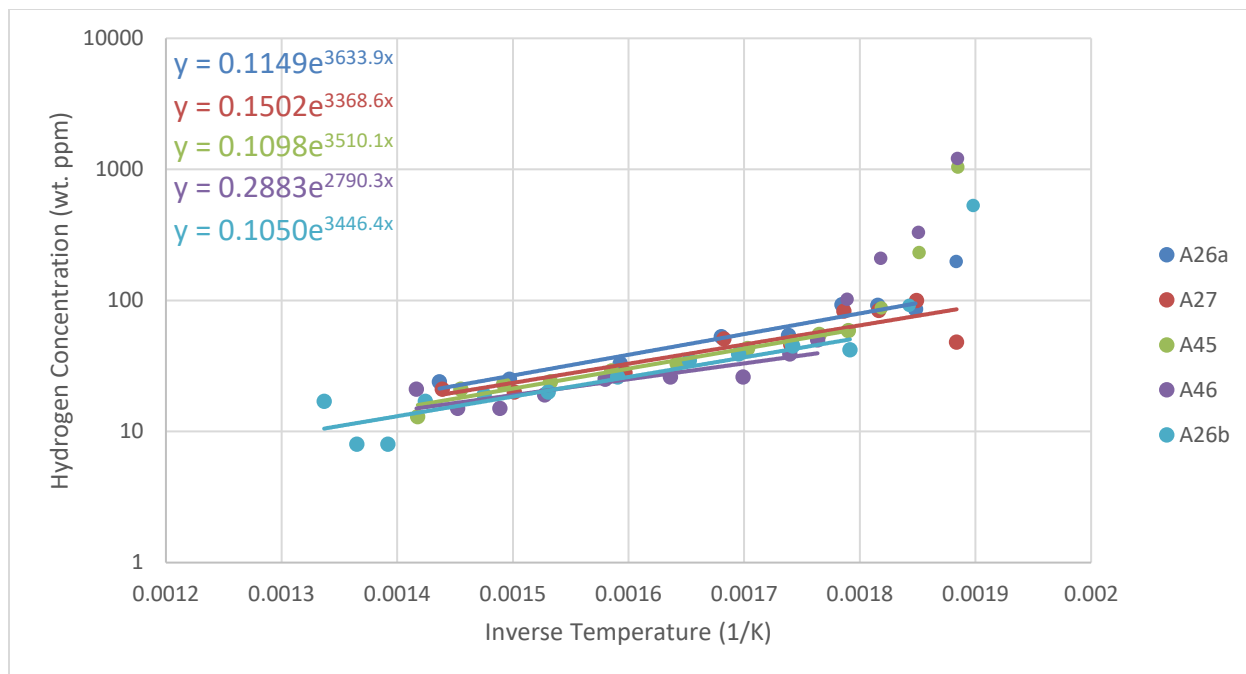


Figure 10: Hydrogen concentration as a function of inverse temperature for Zircaloy-4 (top) and alloys containing niobium (bottom) for cold side temperature of 260°C.

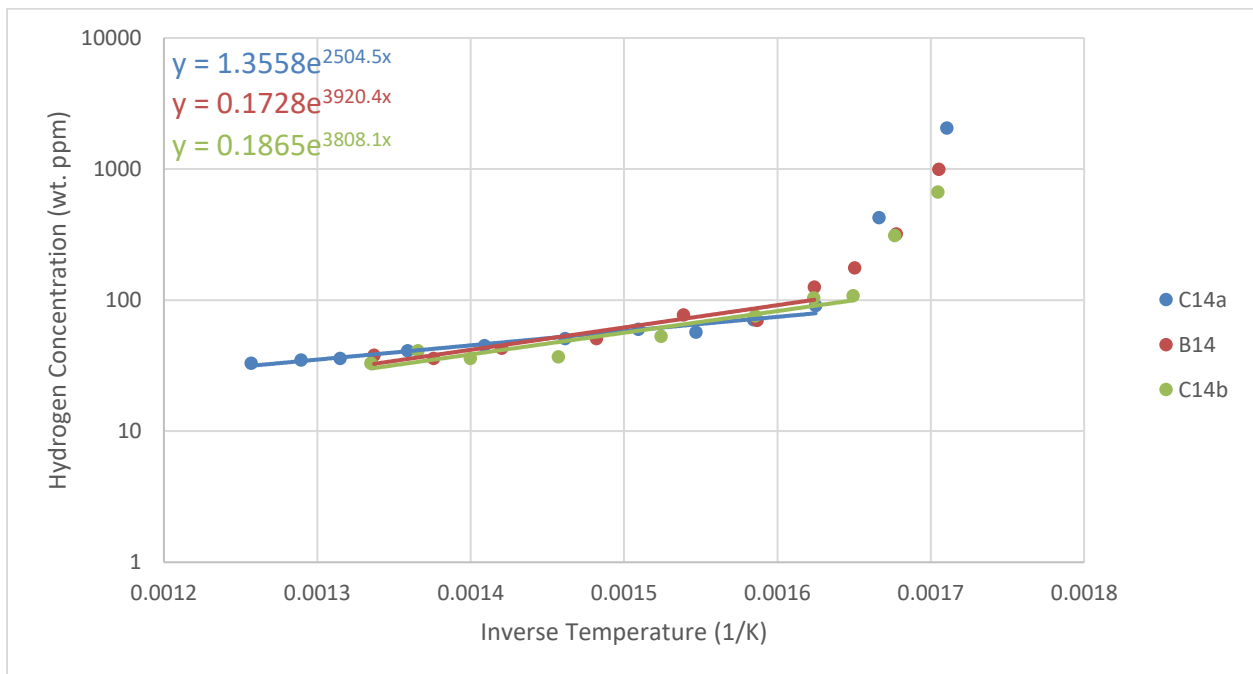
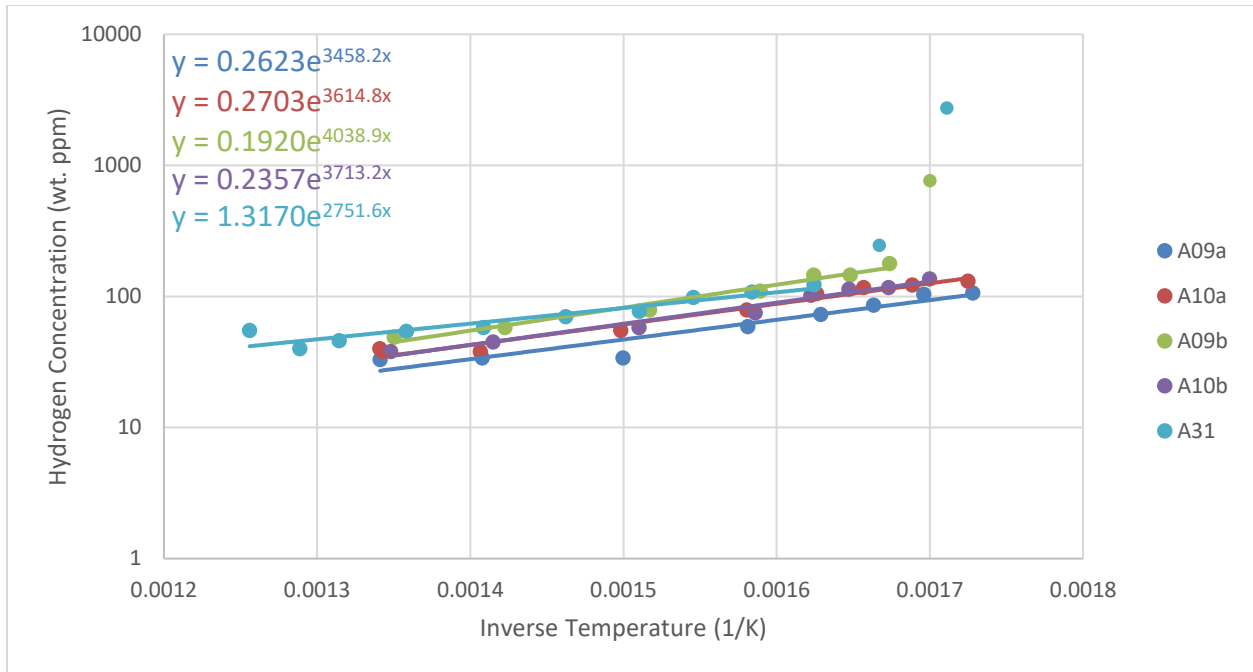


Figure 11: Hydrogen concentration as a function of inverse temperature for Zircaloy-4 (top) and alloys containing niobium (bottom) for cold side temperature of 316°C.

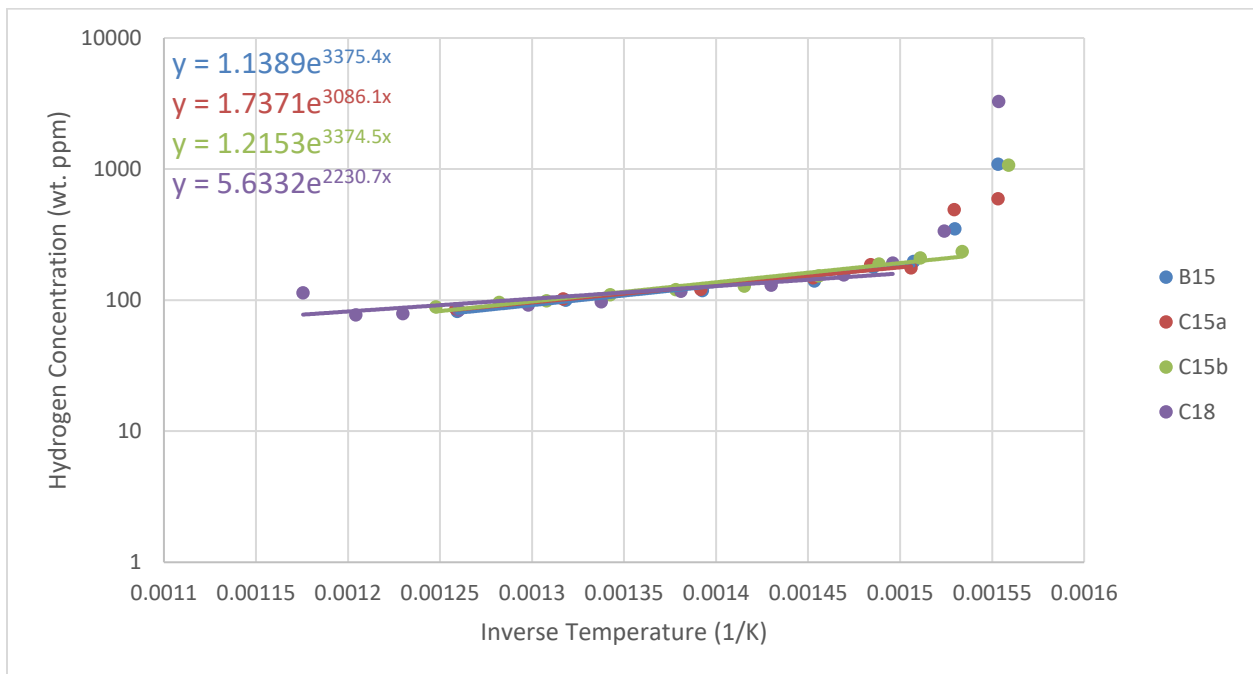
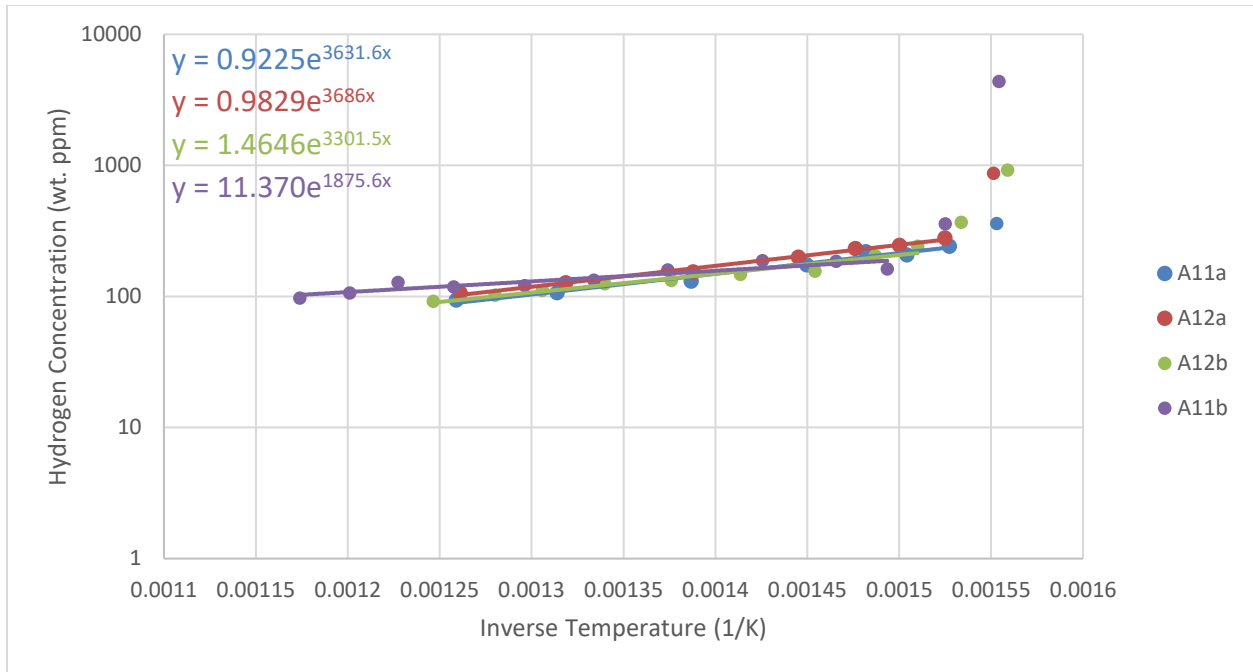


Figure 12: Hydrogen concentration as a function of inverse temperature for Zircaloy-4 (top) and alloys containing niobium (bottom) for cold side temperature of 371°C.

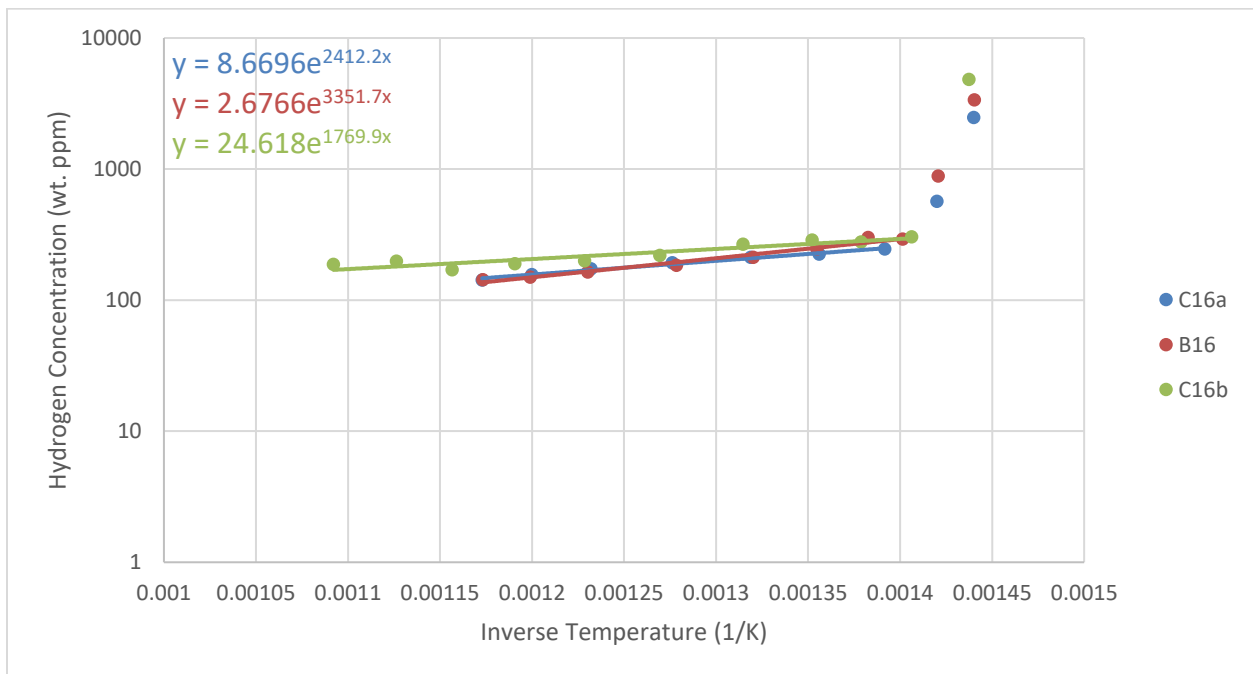
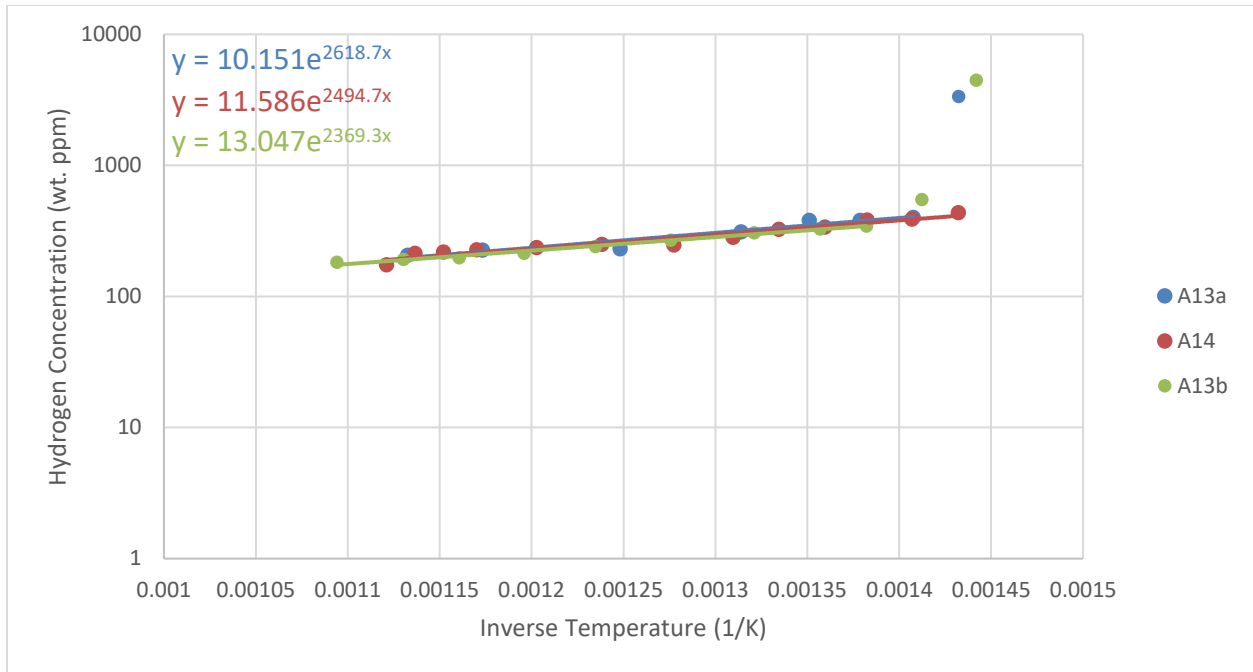


Figure 13: Hydrogen concentration as a function of inverse temperature for Zircaloy-4 (top) and alloys containing niobium (bottom) for cold side temperature of 427°C.

Table 1: Values of Q^* and TSSp determined from Figures 10 – 13 for various cold side temperatures and zirconium alloy compositions.

Specimen	Cold Temperature (°C)	Rate of Temp Increase (°C/cm)	Q^* (J/(mole K))	TSSp (wt. ppm)	Temperature at TSSp (°C)
A26a	260	66	30214	108	257.8
A27	260	66	28008	-	-
A45	260	66	29185	65	276.8
A46	260	66	23200	42	285.9
A26b	260	87	28655	60	269.5
C13	260	87	11886	31	269.7
A09a	316	66	28753	-	-
A10a	316	66	30055	-	-
A09b	316	66	33581	184	315.1
A10b	316	66	30873	-	-
A31	316	87	22878	129	326.7
C14a	316	87	20824	88	327.0
B14	316	66	32596	112	332.7
C14b	316	66	31662	110	323.3
A11a	371	66	30195	260	370.8
A12a	371	66	30647	299	371.5
A12b	371	66	27450	232	378.9
A11b	371	87	15595	199	382.6
B15	371	66	28065	199	380.5
C15a	371	66	25659	195	380.7
C15b	371	66	28057	234	368.3
C18	371	87	18547	169	383.0
A13a	427	77	21773	432	425.0
A14	427	77	20742	-	-
A13b	427	87	19699	370	434.9
C16a	427	66	20056	266	431.0
B16	427	66	27868	313	430.8
C16b	427	87	14716	313	422.5

3.2. Experiment 2 Data Sets

Figures 14 - 15 and Table 2 present diffusion and precipitation data for specimens involved with experiment 2.

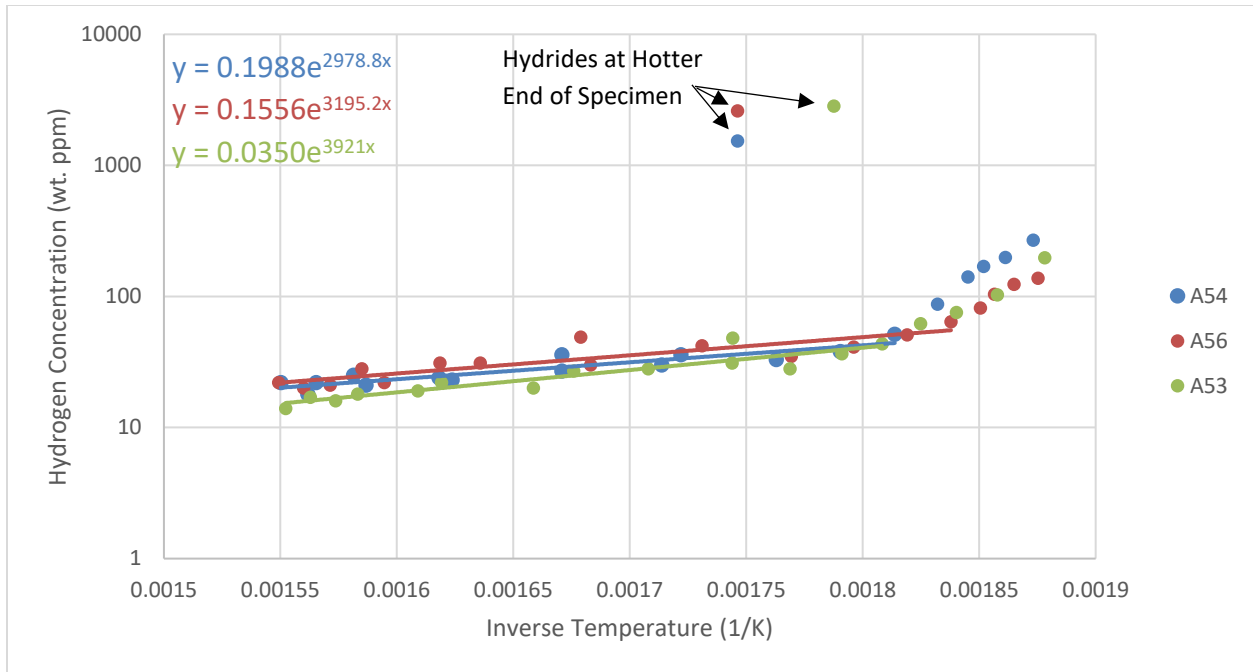


Figure 14: Hydrogen concentration as a function of inverse temperature for Zircaloy-4 for cold side temperature of 260°C and asymmetric temperature gradient.

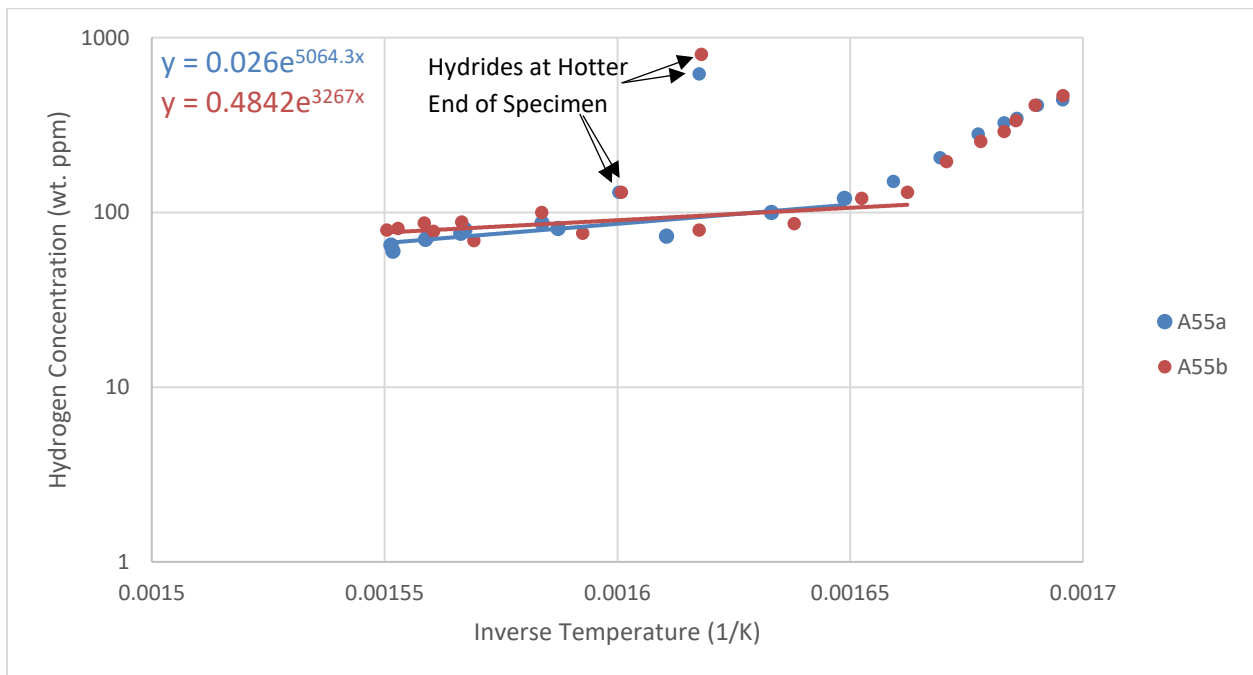


Figure 15: Hydrogen concentration as a function of inverse temperature for Zircaloy-4 for cold side temperature of 316°C and asymmetric temperature gradient.

Table 2: Values of Q^* and TSSp determined from Figures 14 – 15 for various cold side temperatures for Zircaloy-4.

Specimen	Cold End Temperature (°C)	Q^* (J/(mole K))	TSSp (wt. ppm)	Temperature at TSSp (°C)
A54	260	24767	47	272.6
A56	260	26566	58	267.3
A53	260	32601	45	274.8
A55a	316	42107	116	329.5
A55b	316	27163	114	325.4

Figure 16 demonstrates the experimental distribution of Q^* for Zircaloy-4 and Zircaloy-niobium alloys, and shows that Q^* has little dependence on temperature or zirconium alloy composition. From Tables 1 and 2, the average Q^* values for Zircaloy-4 and Zircaloy-niobium alloys are 27,487 and 23,630 J/(mole K) with a standard deviation of 5,500 and 6,800 J/(mole K), respectively. Although the average experimental values agree with values presented in literature, the standard deviation of the experimental data is large. One potential source of error is uncertainty in the hydrogen concentration measurements. However, except for the occasional measurement that is considerably out of line with expectations, this source of error is typically small. These fluctuations likely indicate that microstructure composition plays a notable role in how hydrogen diffuses and precipitates. Table 3 compares average Q^* data from Tables 1 and 2 with data from literature.

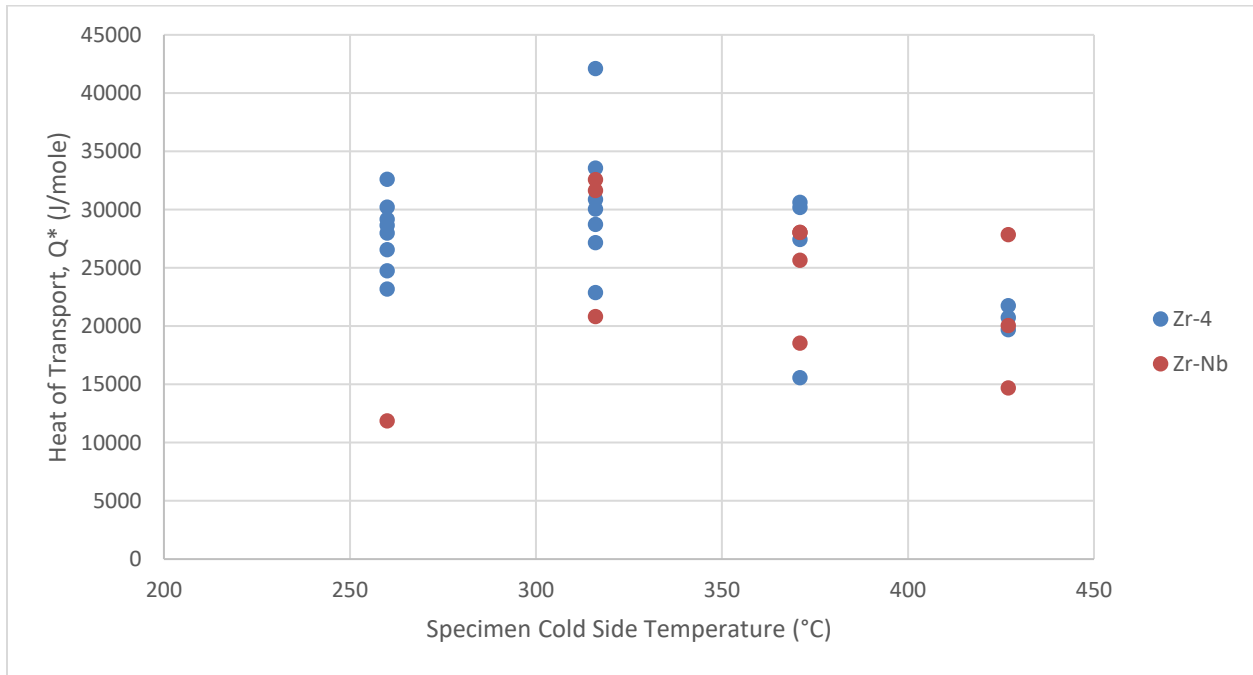


Figure 16: Heat of transport values determined by experimentation.

Table 3: Comparison of average experimental heat of transport values (green and orange) with values from literature.

Reference	Material	Cold End Temperature (°C)	Q* (J/mole K)
A. Sawatzsky [39]	Zr	300	24300
A. Sawatzsky [39]	Zr	500	25100
A. Sawatzsky [39]	Zr-2/0.6% Y	300	23800
A. Sawatzsky [39]	Zr-2/0.6% Y	496	24300
B. Kammenzind [25]	Zr-4	316	30500
B. Kammenzind [25]	Zr-4	482	31000
B. Kammenzind	Zr-4	260	27900
B. Kammenzind	Zr-Nb	260	11900
B. Kammenzind	Zr-4	316	30800
B. Kammenzind	Zr-Nb	316	28400
B. Kammenzind	Zr-4	371	26000
B. Kammenzind	Zr-Nb	371	25100
B. Kammenzind	Zr-4	427	20800
B. Kammenzind	Zr-Nb	427	20900

4. Calculation of Hydrogen Distribution using BISON

BISON is a nuclear fuel performance code that is used to model a variety of fuel forms such as light water reactor fuel rods and TRISO fuel particles, and can be used to simulate uranium dioxide fuel behavior, zirconium alloy cladding behavior, and gap behavior.

4.1. BISON Model Setup

The data in Appendix A has been modeled using the BISON code to predict hydrogen transport and morphology based on initial hydrogen concentration distribution and temperature profile. BISON operates on the MOOSE (Multiphysics Object Oriented Simulation Environment) framework, which is an open-source software developed by the Idaho National Laboratory. Specifically, MOOSE uses fully-coupled multiphysics solvers and the finite element method to algebraically solve the complex sets of partial differential equations that represent physical processes such as heat transfer and solid mechanics. BISON is an engineering-scale, finite element-based nuclear fuel performance code that implements material properties and focuses on thermomechanics and species diffusion for various simulation geometries [40]. A module was created in BISON to model hydrogen diffusion as described in [13] and [41].

The one-dimensional model created in BISON for these experiments assumes that the temperature gradient can be linearly interpolated between thermocouple readings, the total amount of hydrogen in the specimen never changes, and the hydrogen distribution does not depend on the width or thickness of the specimen. The initial hydrogen concentration was

determined by dividing the sum of the measured hydrogen concentrations (from LECO analysis) by the sum of the sample lengths. The time step was set at 1000 seconds and the simulations ran for the same amount of time as the experiment anneals. The smaller experiment 1 specimens were modeled with 275 elements, and the larger experiment 2 specimens were modeled with 500 elements. Figure 17 shows an example of initial conditions implemented in BISON for simulations of experiment 1 and experiment 2.

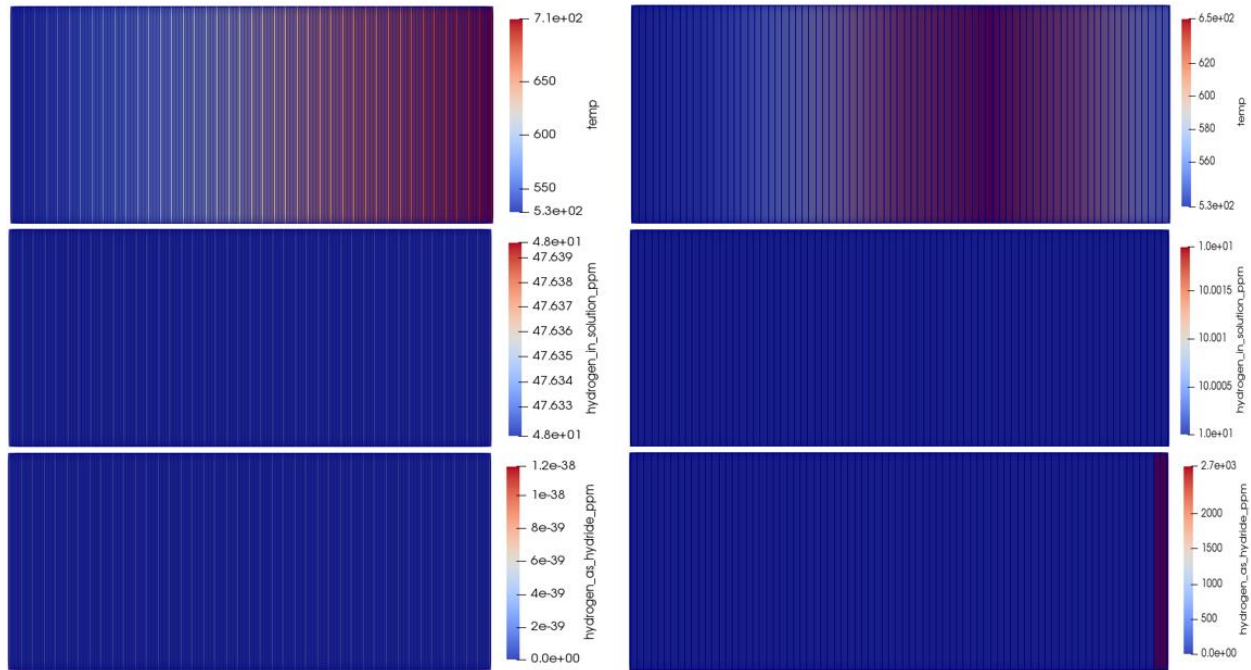


Figure 17: Initial conditions pertaining to temperature, hydrogen in solid solution, and hydrides for simulations of experiment 1 (left) and experiment 2 (right). For experiment 1, note the linearly increasing temperature distribution and the homogeneous hydrogen distribution. For experiment 2, note the asymmetric temperature distribution and the hydride rim concentrated at the hotter end of the specimen. Temperature inputs in BISON are in Kelvins.

When modeling hydrogen behavior in a zirconium alloy, BISON determines the concentrations of soluble hydrogen and zirconium hydrides by solving for Fickian diffusion, thermal diffusion, precipitation rates, dissolution rates, and the time derivatives of hydrogen in solid solution. BISON computes hydrogen concentrations by using kernels and material property inputs to evaluate integral values associated with Equations 2 – 11 above. Table 4 provides the material properties that are hard-coded into BISON and compares these values with associated values that were determined by the experiments above. By using the simplified CladdingHydrides Action to establish the model in BISON, the user can define values for the diffusion frequency factor (A_D), diffusion activation energy (Q_D), and heat of transport (Q^*) [40].

Table 4: Comparison of model constants used by BISON and physical constants determined by experiments 1 and 2.

Physical Phenomenon	Parameter	BISON Value	Experiment Value	Unit	Equation
Fick's Law	A_D	7.90×10^{-3}	-	cm ² /s	3
	Q_D	4.49×10^4	-	J/mole	3
Soret Effect	Q^*	2.51×10^4	2.62×10^4	J/mole	4
Precipitation	A_p	1.39×10^5	1.74×10^5	wt. ppm	5
	Q_p	3.45×10^4	3.64×10^4	J/mole	5
Dissolution	A_d	1.06×10^5	-	wt. ppm	6
	Q_d	3.60×10^4	-	J/mole	6
Precipitation Kinetics	A_α	6.23×10^1	-	s ^{-1/2}	7
	Q_α	4.12×10^4	-	J/mole	7

As seen in Table 4, the values of Q^* , A_p , and Q_p can be validated by the experimental data in Appendix A. From Tables 1 and 2, the average values of Q^* for all of the data and only the experiment 1 data is 26,200 J/mole and 25,400 J/mole, respectively, which are close to BISON's Q^* value of 25,100 J/mole. Likewise, only minor differences exist between BISON's values for A_p and Q_p , and those determined by a least squares fit through all of the experimental data. Figure 18 shows the equilibrium conditions for TSSp and TSSd; the associated equations are described by Equations 5 and 6.

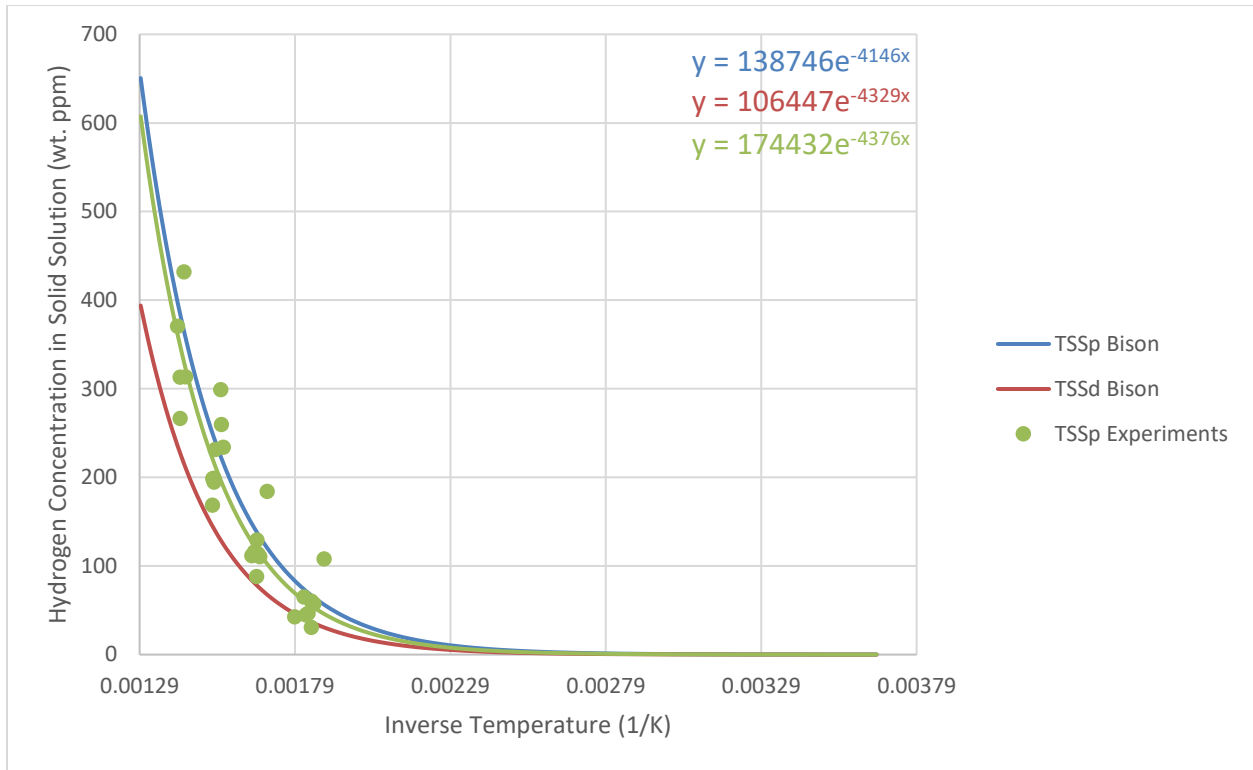


Figure 18: Equilibrium conditions for TSSp and TSSd, where the equation corresponding to “TSSp Experiments” can be used to solve for A_p and Q_p in Table 4.

Figure 19 compares the TSSp/TSSd data found during literature review (Figure 4) with the data hard-coded in BISON and determined by these experiments. It is interesting to note that the TSSp data displays much greater variation than is typically seen in a single set of Differential Scanning Calorimetry (DSC) data, which makes up the majority of the data sets illustrated in Figure 19. This may be an indication that there is no predictable TSSp value but that the kinetic and microstructural factors play heavily into the amount of supersaturation that the zirconium matrix can support.

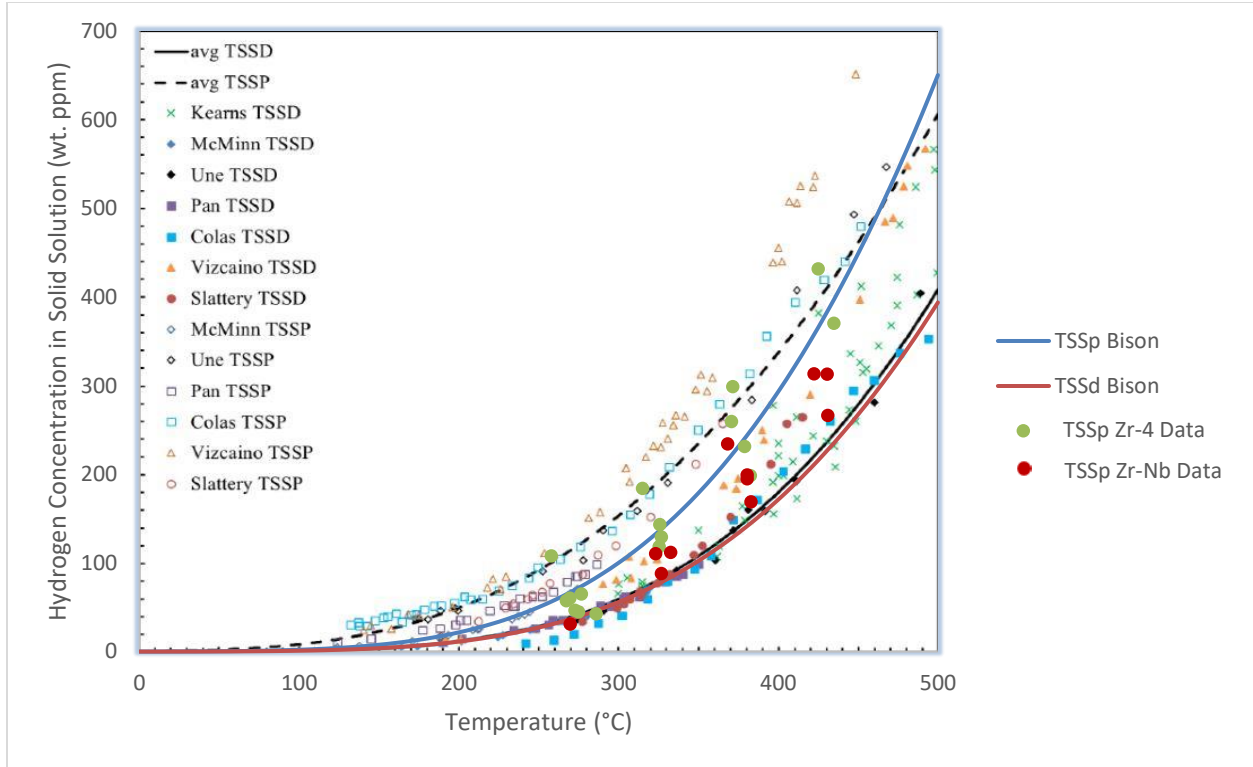


Figure 19: TSSp and TSSd data from experiments, BISON inputs, and literature review [24] [30] [32] [33] [34] [35].

4.2. BISON Model Results

4.2.1. Experiment 1 Data Models

Figures 20 – 47 compare hydrogen distribution simulations as a function of specimen position with the experiment 1 data found in Tables A1 – A14 of Appendix A. These figures demonstrate BISON’s ability to accurately simulate hydrogen distribution and morphology in steep temperature profiles, where thermal diffusion is much greater than Fickian diffusion. Furthermore, BISON simulation fidelity improves as the rate of temperature change and experiment annealing time increase. For each simulation, the model correctly predicts that hydrides coalesce in the coldest regions of the specimen. However, the model often under predicts the amount of hydrides in the regions adjacent to the coldest part of the specimen, where hydrides have been observed experimentally. This discrepancy between simulation and reality may occur for various reasons: (1) BISON may reach equilibrium faster than reality, and the specimen annealing time may not have been long enough to establish the distribution observed in the simulations, as longer anneals may promote more migration to the coldest part of the specimen. (2) The code may over predict the driving force due to thermal diffusion and under predict the driving force due to Fickian diffusion. (3) The code may need to incorporate microstructure composition details or machining practices. (4) The code may not accurately capture how the presence of hydrides affects additional precipitation.

In Figure 20, BISON Average corresponds to the simulation values averaged in conjunction with sample lengths. In Figures 20 and 21, the model was also run with the initial hydrogen concentration distributed as hydrides, which had little effect on the end result.

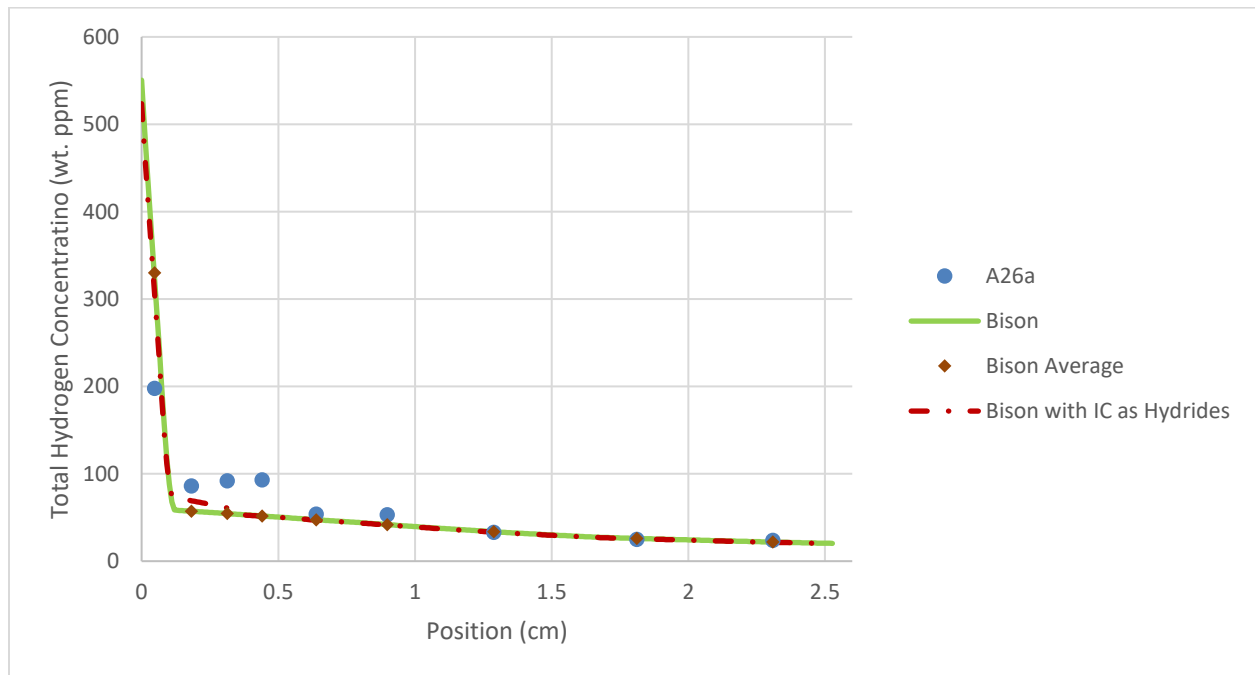


Figure 20: Specimen A26a annealed for 27 days in linear temperature gradient from 260°C to 427°C (66°C/cm) with initial homogeneous hydrogen concentration of 48 wt. ppm.

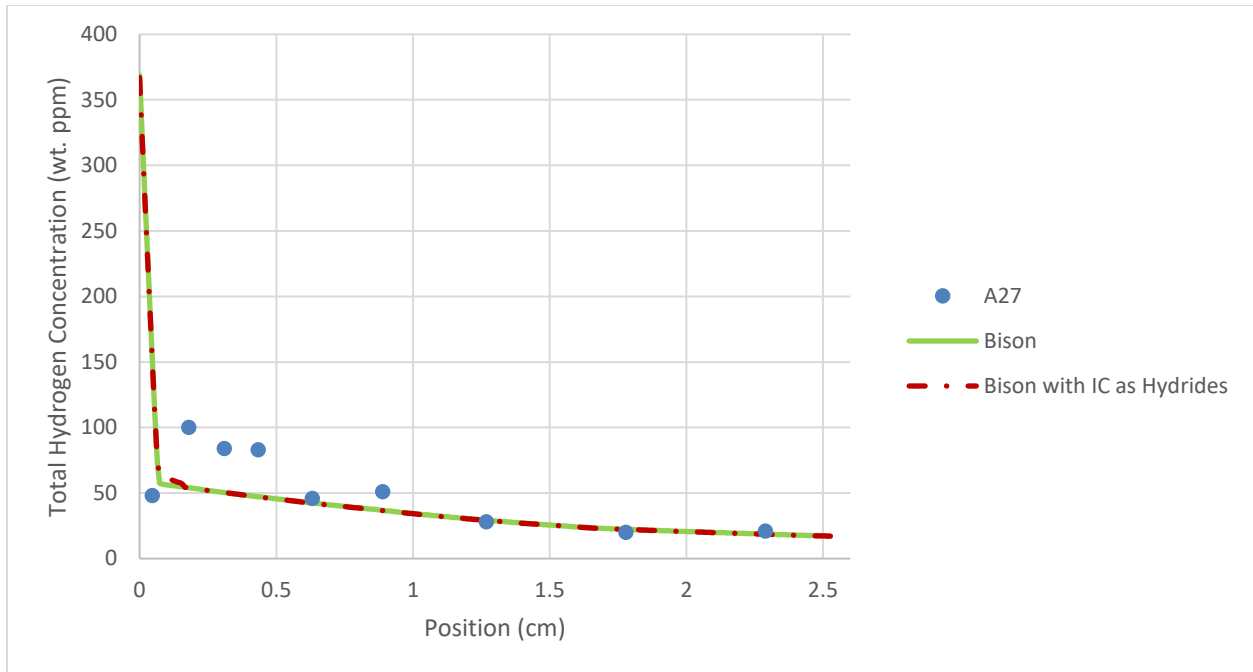


Figure 21: Specimen A27 annealed for 27 days in linear temperature gradient from 260°C to 427°C (66°C/cm) with initial homogeneous hydrogen concentration of 37 wt. ppm.

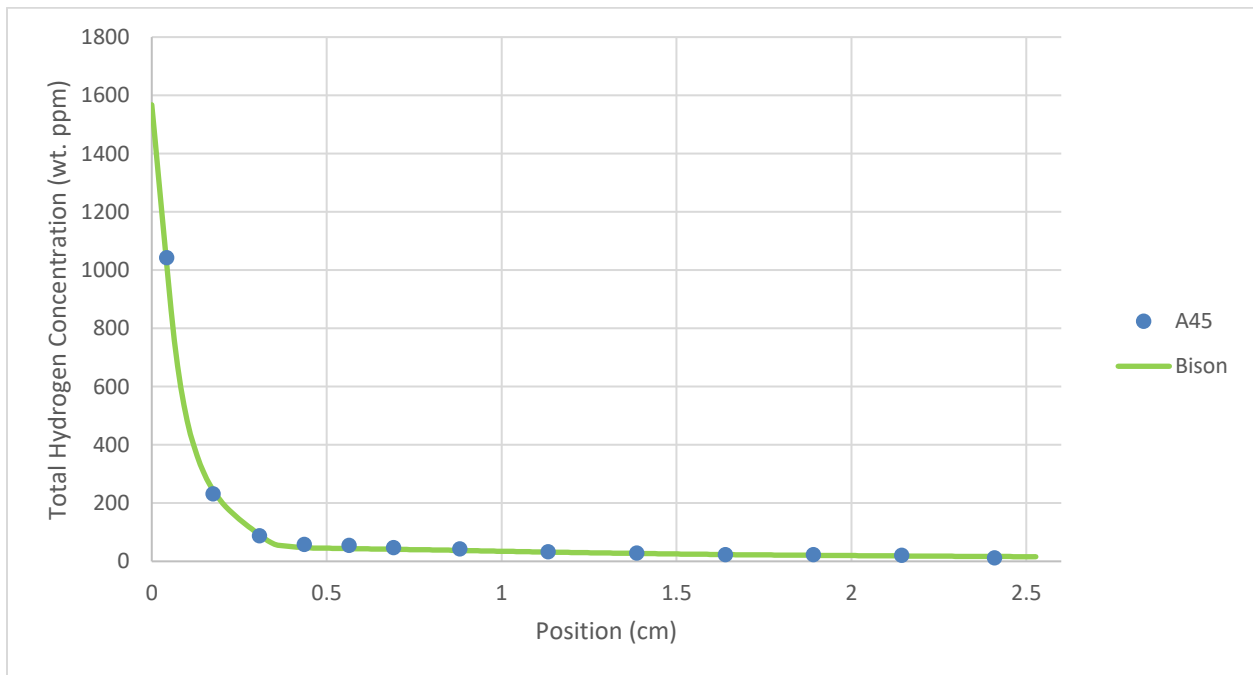


Figure 22: Specimen A45 annealed for 77 days in linear temperature gradient from 260°C to 427°C (66°C/cm) with initial homogeneous hydrogen concentration of 85 wt. ppm.

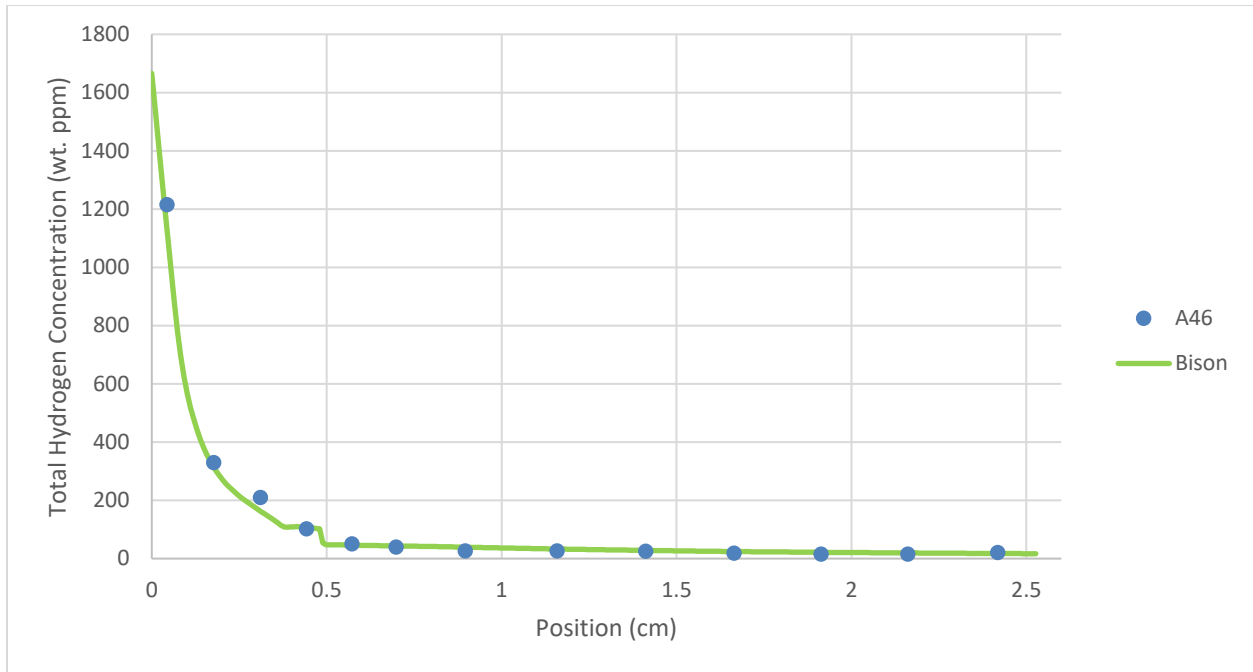


Figure 23: Specimen A46 annealed for 77 days in linear temperature gradient from 260°C to 427°C (66°C/cm) with initial homogeneous hydrogen concentration of 101 wt. ppm.

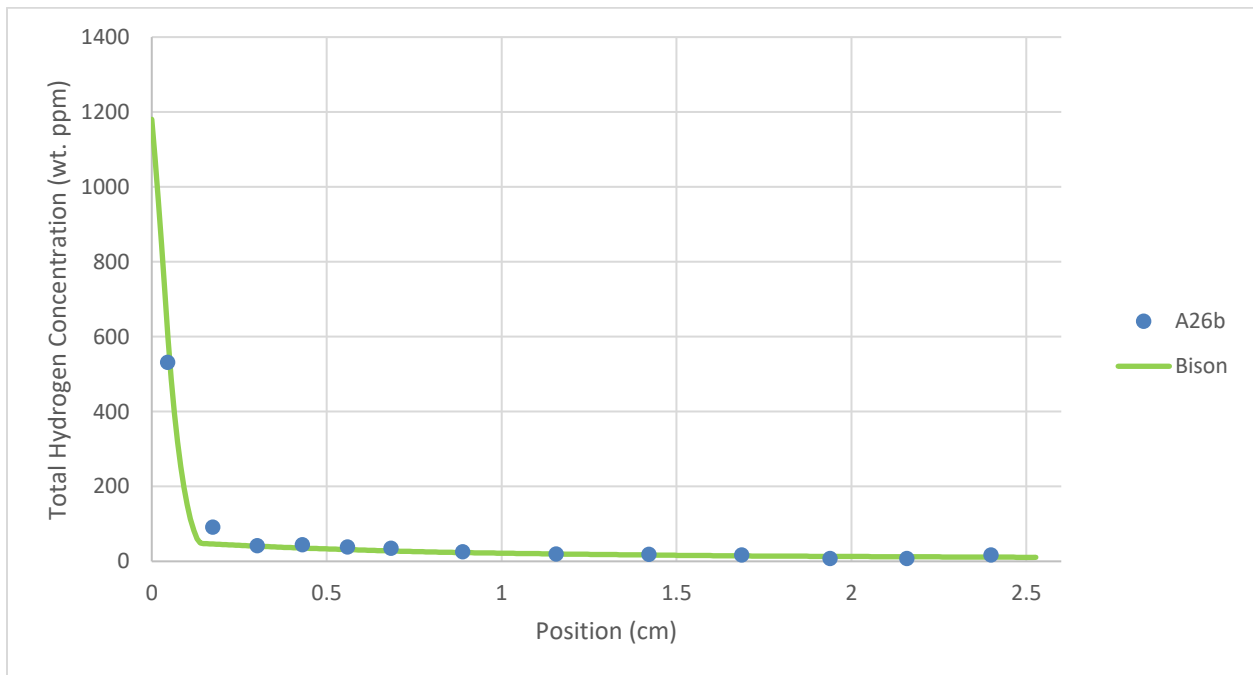


Figure 24: Specimen A26b annealed for 54 days in linear temperature gradient from 260°C to 482°C (87°C/cm) with initial homogeneous hydrogen concentration of 47 wt. ppm.

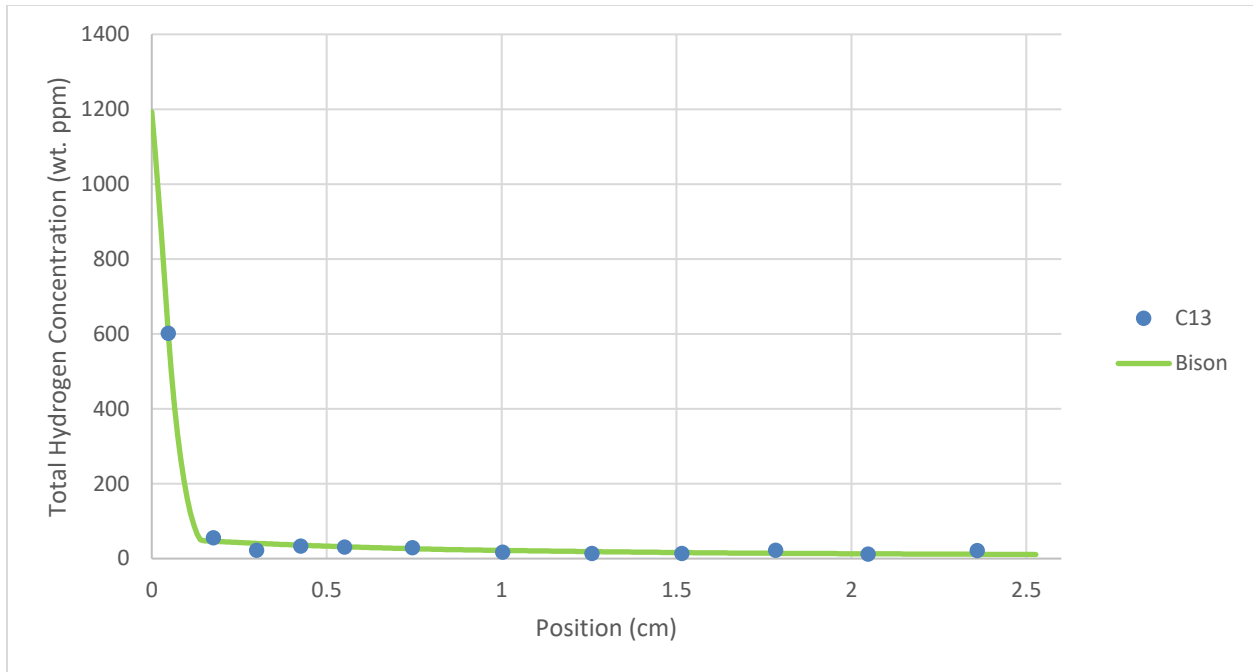


Figure 25: Specimen C13 annealed for 54 days in linear temperature gradient from 260°C to 482°C (87°C/cm) with initial homogeneous hydrogen concentration of 48 wt. ppm.

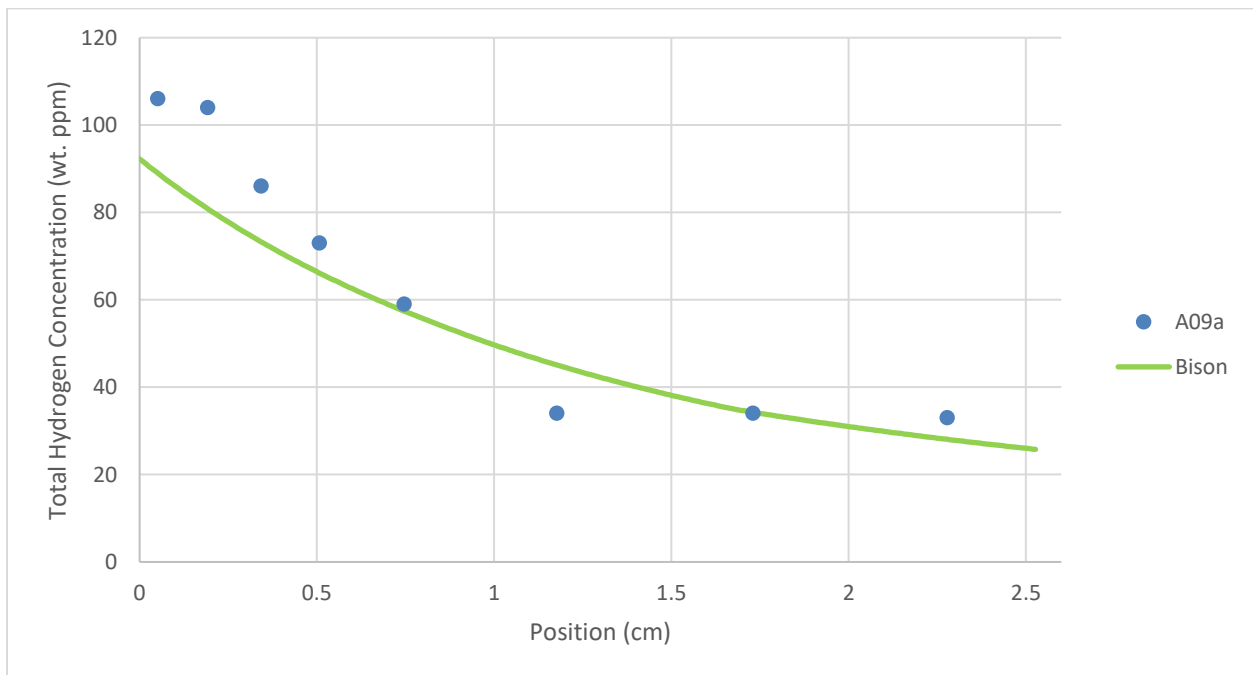


Figure 26: Specimen A09a annealed for 15 days in linear temperature gradient from 316°C to 482°C (66°C/cm) with initial homogeneous hydrogen concentration of 48 wt. ppm.

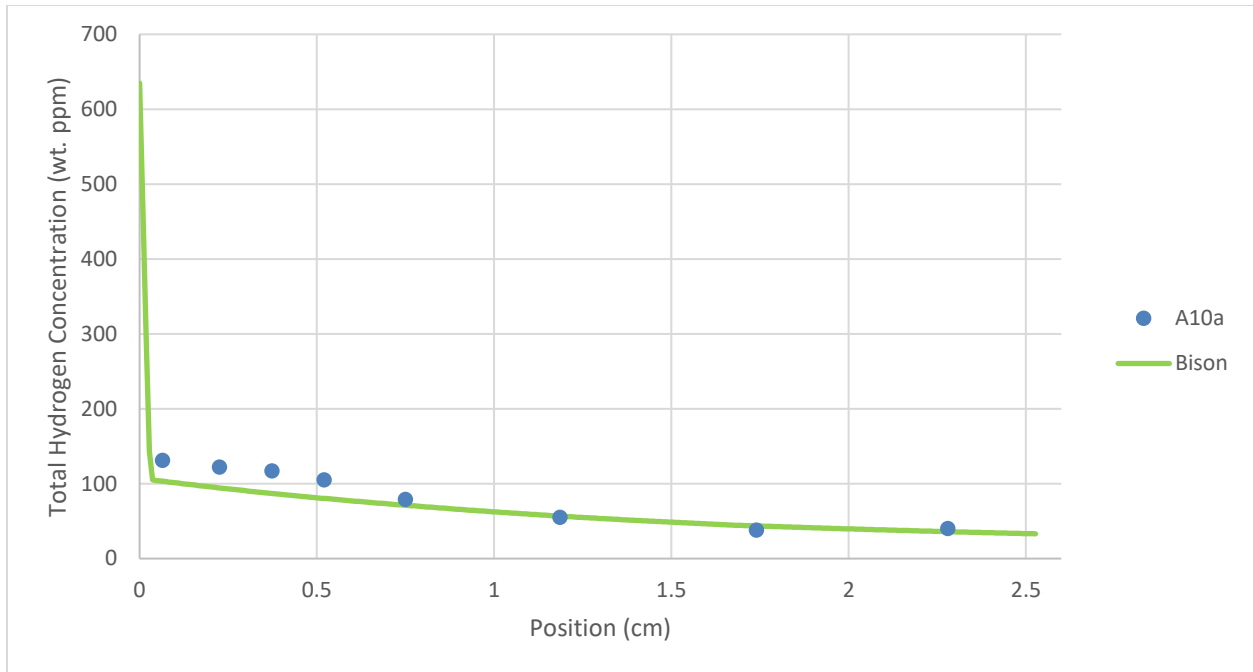


Figure 27: Specimen A10a annealed for 15 days in linear temperature gradient from 316°C to 482°C (66°C/cm) with initial homogeneous hydrogen concentration of 64 wt. ppm.

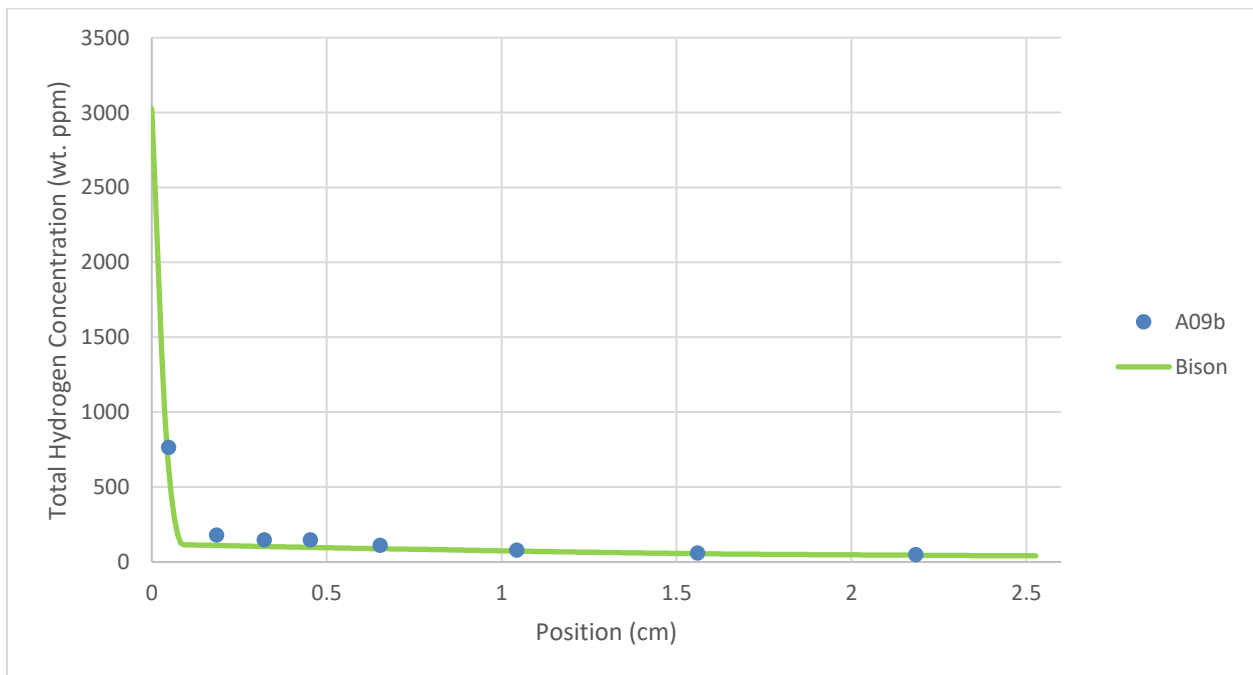


Figure 28: Specimen A09b annealed for 32 days in linear temperature gradient from 316°C to 482°C (66°C/cm) with initial homogeneous hydrogen concentration of 108 wt. ppm.

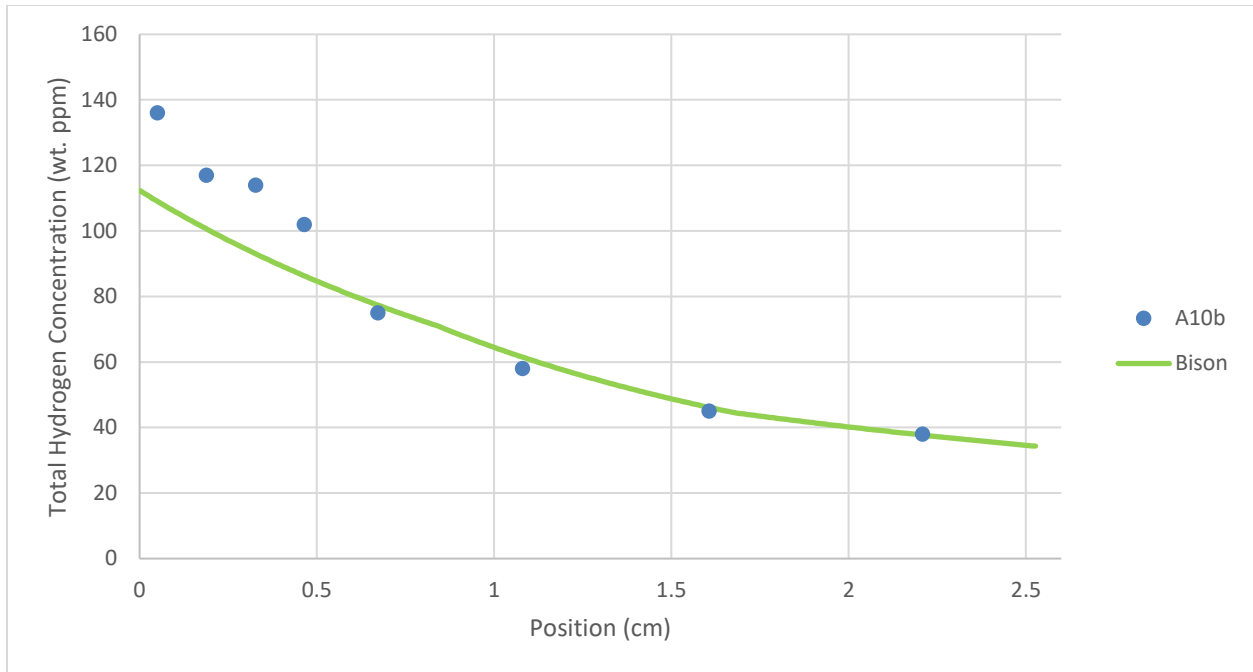


Figure 29: Specimen A10b annealed for 32 days in linear temperature gradient from 316°C to 482°C (66°C/cm) with initial homogeneous hydrogen concentration of 62 wt. ppm.

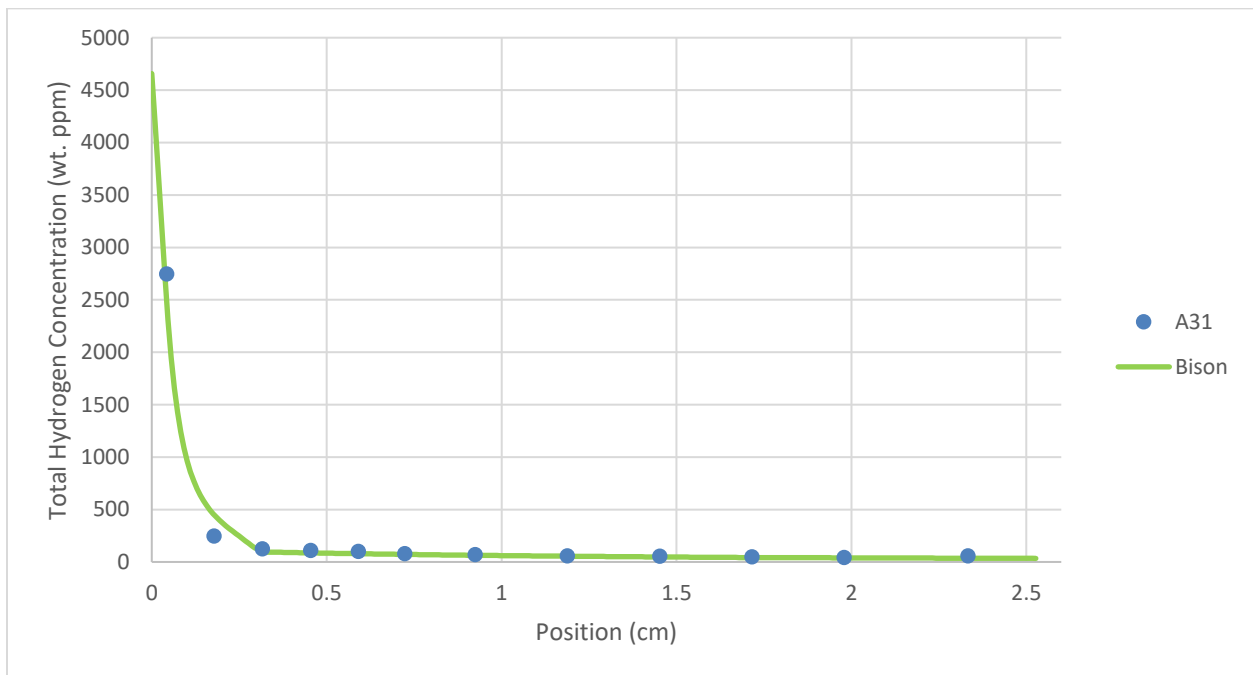


Figure 30: Specimen A31 annealed for 26 days in linear temperature gradient from 316°C to 538°C (87°C/cm) with initial homogeneous hydrogen concentration of 184 wt. ppm.

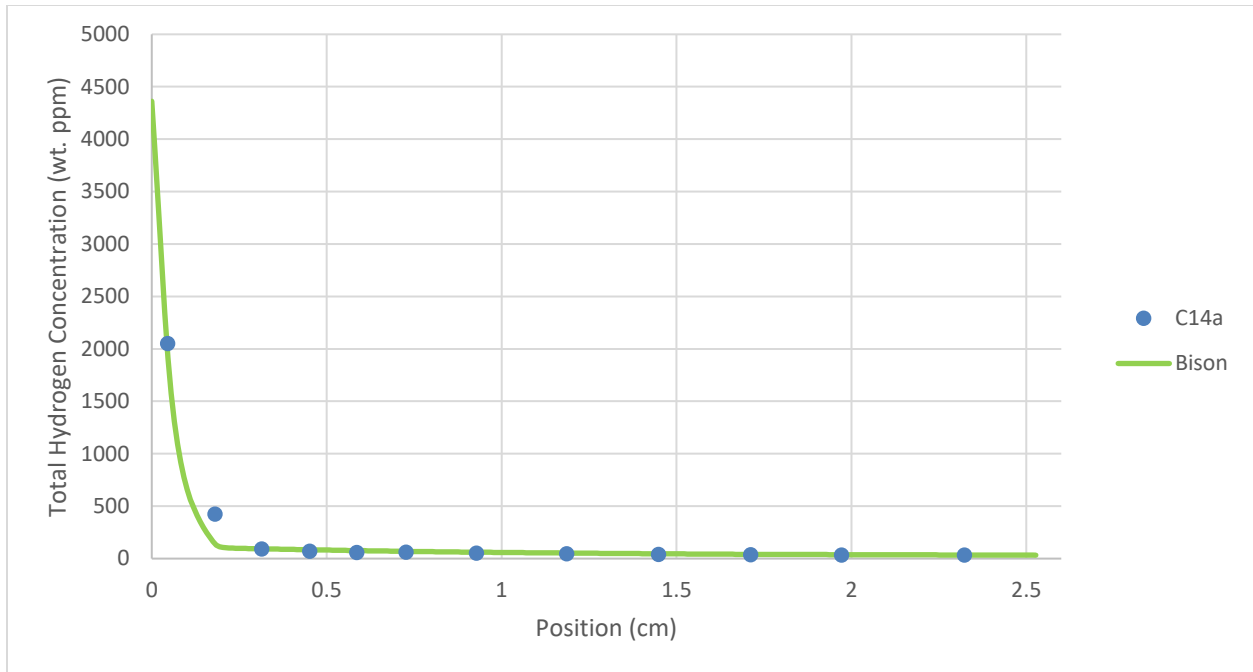


Figure 31: Specimen C14a annealed for 26 days in linear temperature gradient from 316°C to 538°C (87°C/cm) with initial homogeneous hydrogen concentration of 151 wt. ppm.

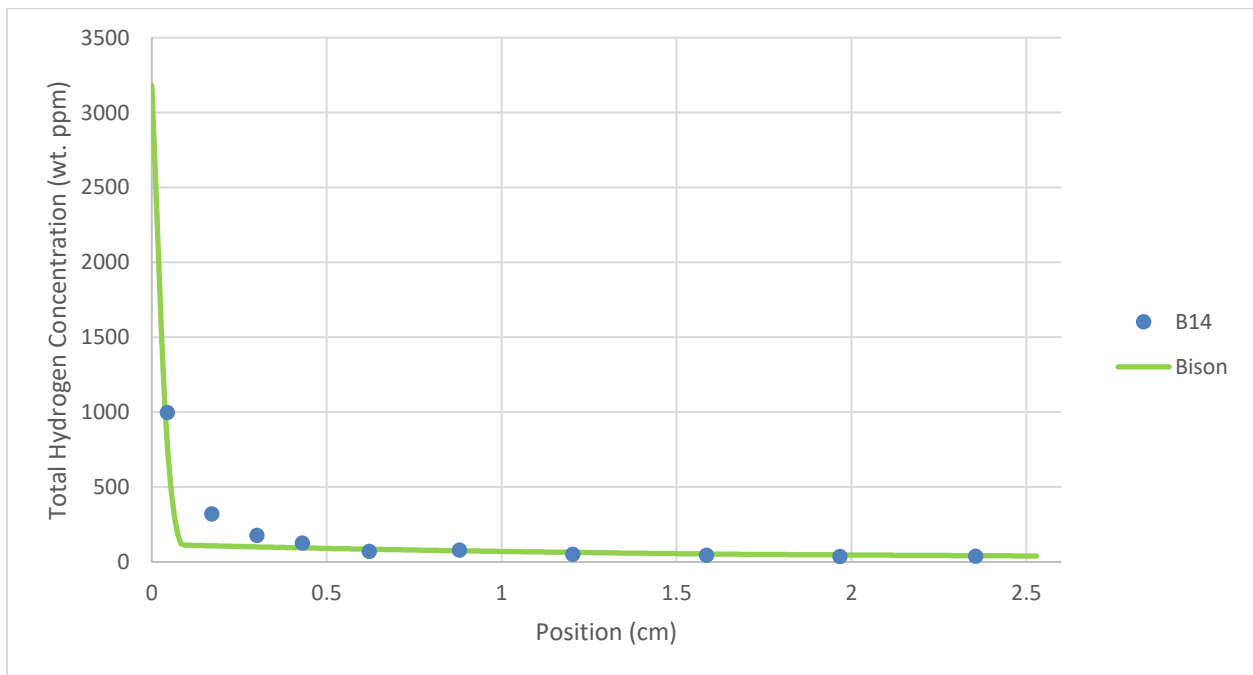


Figure 32: Specimen B14 annealed for 32 days in linear temperature gradient from 316°C to 482°C (66°C/cm) with initial homogeneous hydrogen concentration of 108 wt. ppm.

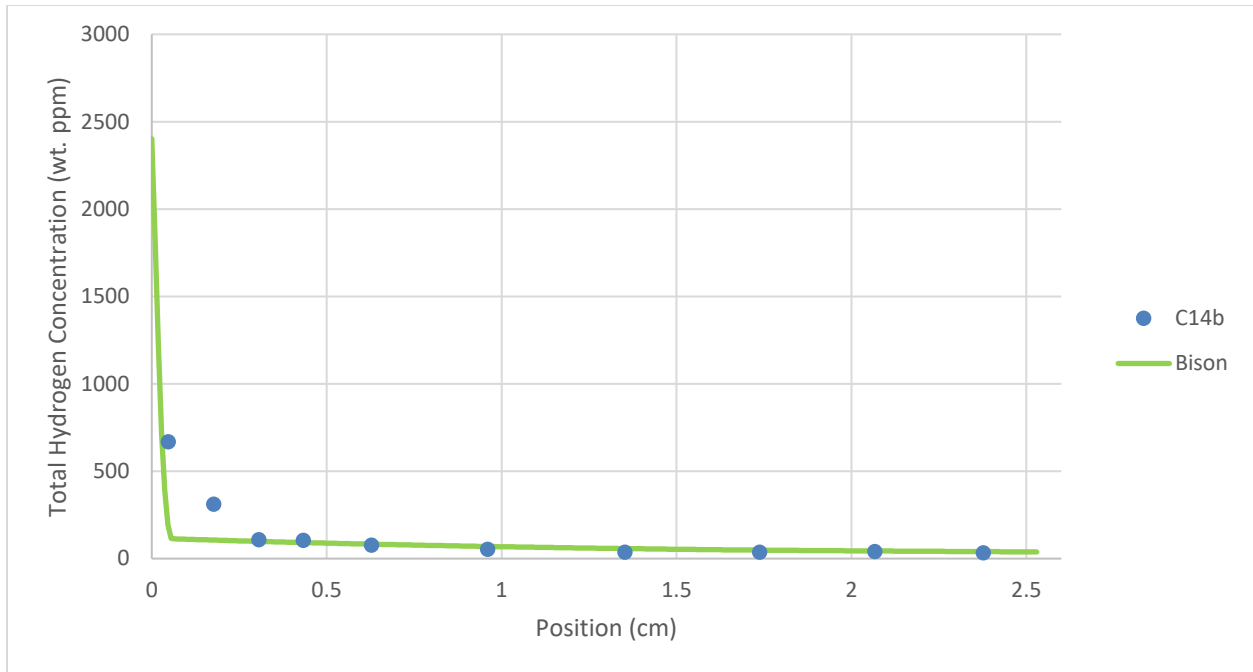


Figure 33: Specimen C14b annealed for 32 days in linear temperature gradient from 316°C to 482°C (66°C/cm) with initial homogeneous hydrogen concentration of 87 wt. ppm.

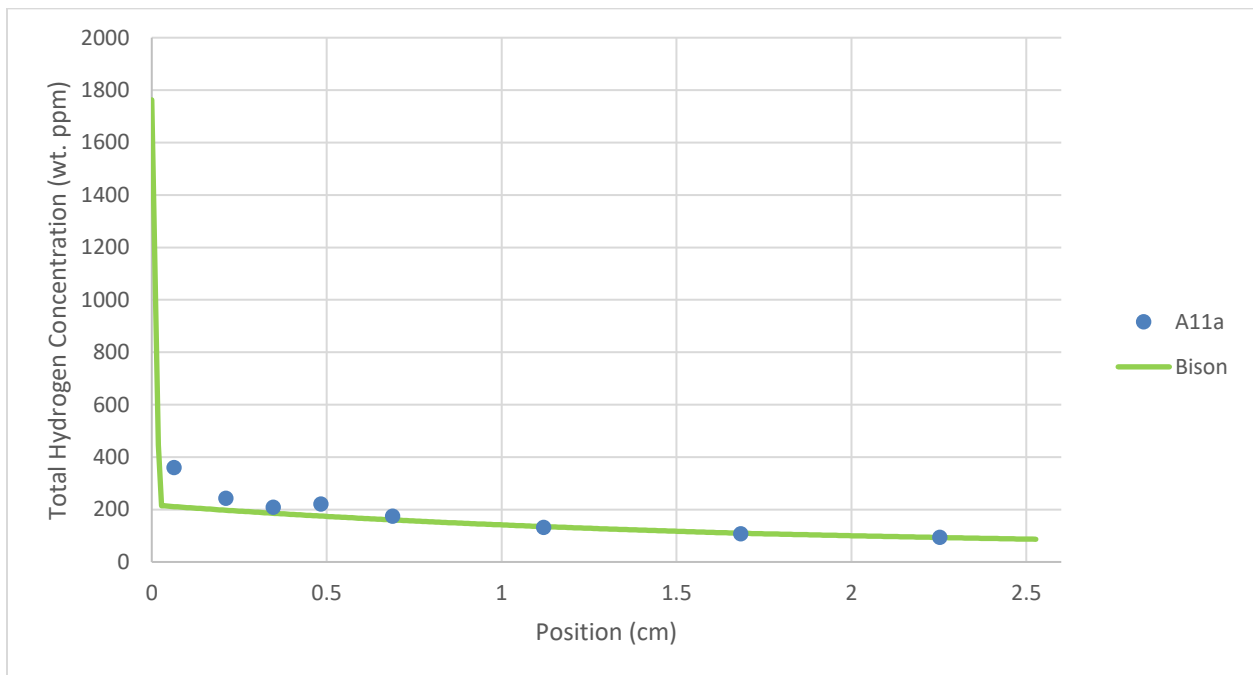


Figure 34: Specimen A11a annealed for 9 days in linear temperature gradient from 371°C to 538°C (66°C/cm) with initial homogeneous hydrogen concentration of 145 wt. ppm.

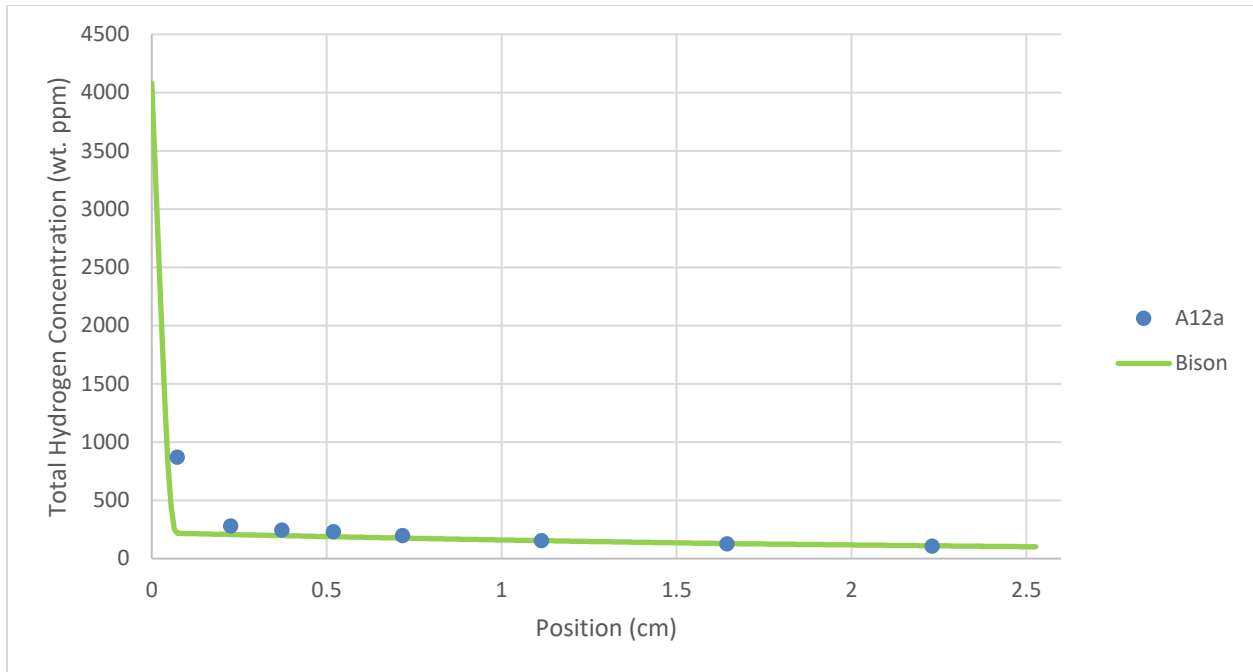


Figure 35: Specimen A12a annealed for 9 days in linear temperature gradient from 371°C to 538°C (66°C/cm) with initial homogeneous hydrogen concentration of 199 wt. ppm.

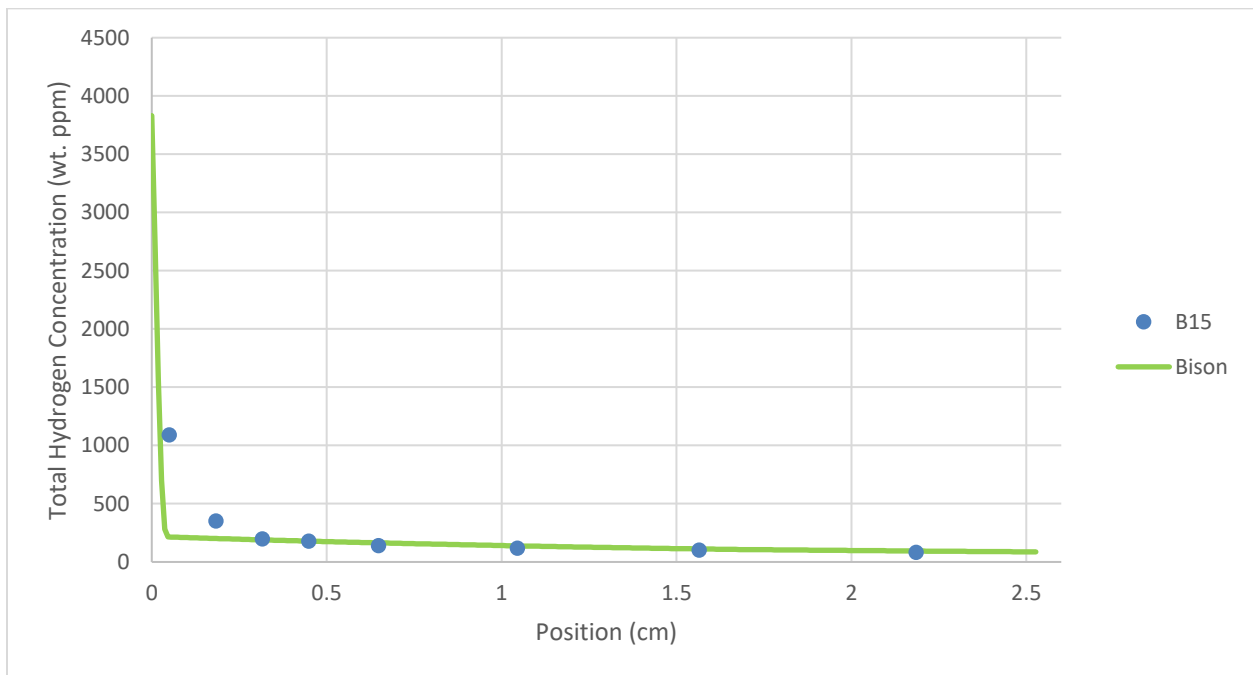


Figure 36: Specimen B15 annealed for 14 days in linear temperature gradient from 371°C to 538°C (66°C/cm) with initial homogeneous hydrogen concentration of 164 wt. ppm.

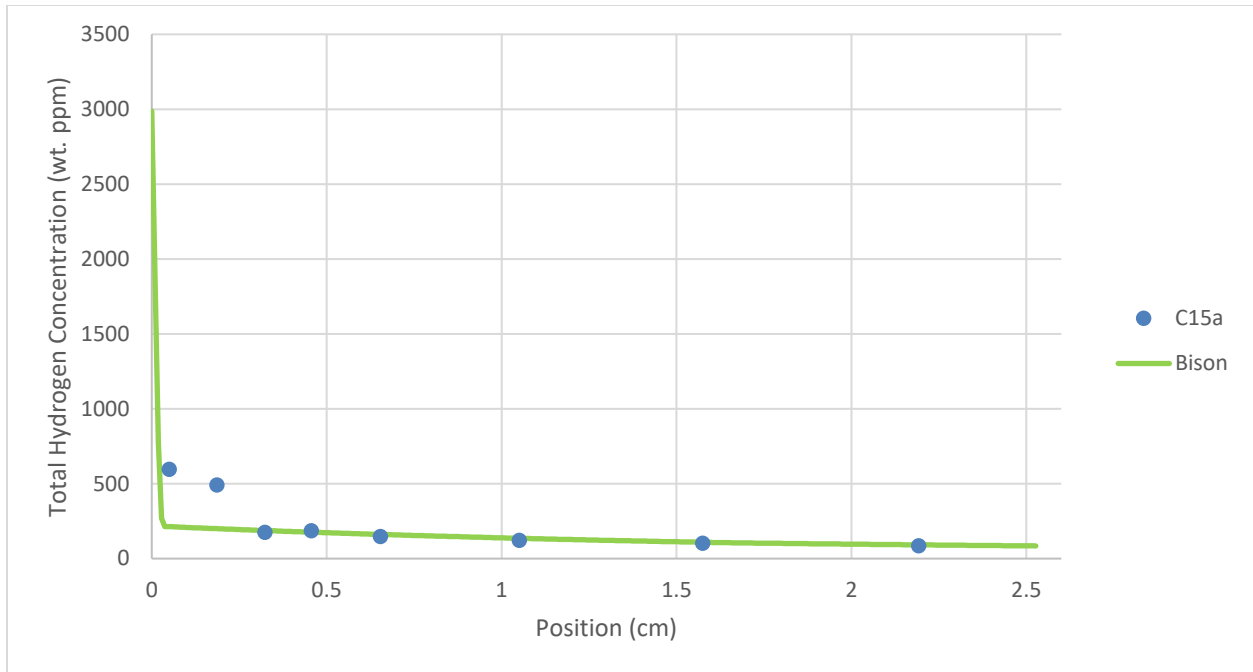


Figure 37: Specimen C15a annealed for 14 days in linear temperature gradient from 371°C to 538°C (66°C/cm) with initial homogeneous hydrogen concentration of 151 wt. ppm.

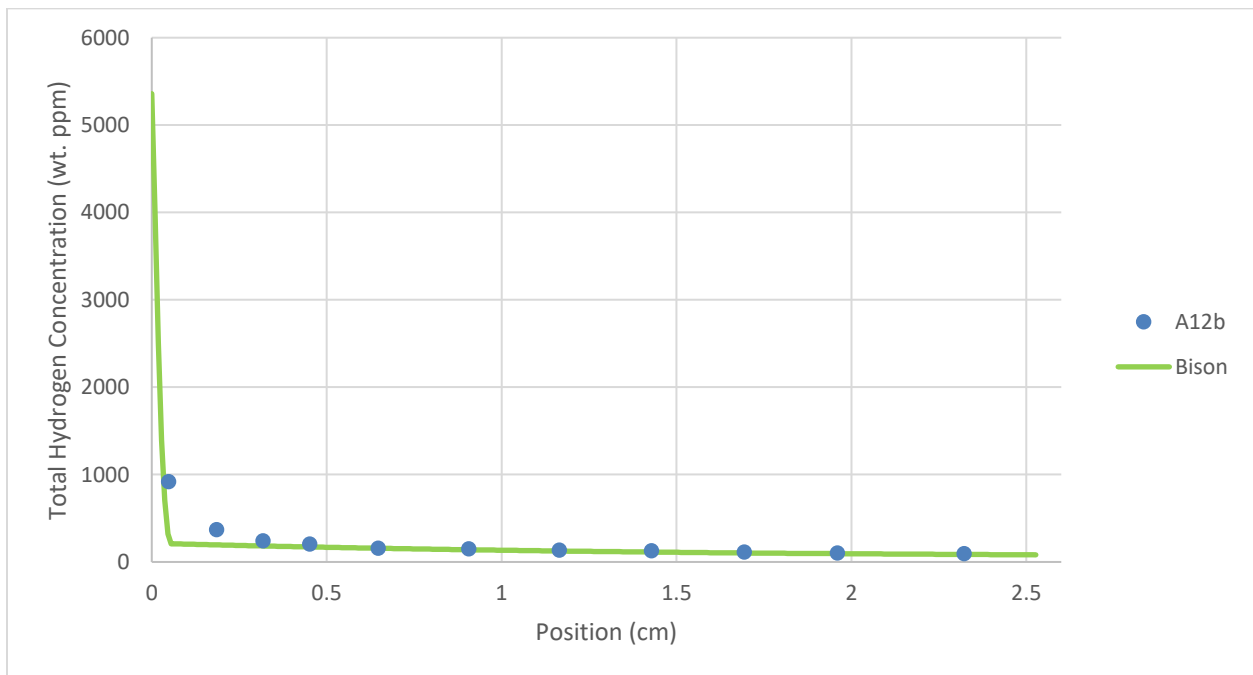


Figure 38: Specimen A12b annealed for 18 days in linear temperature gradient from 371°C to 538°C (66°C/cm) with initial homogeneous hydrogen concentration of 176 wt. ppm.

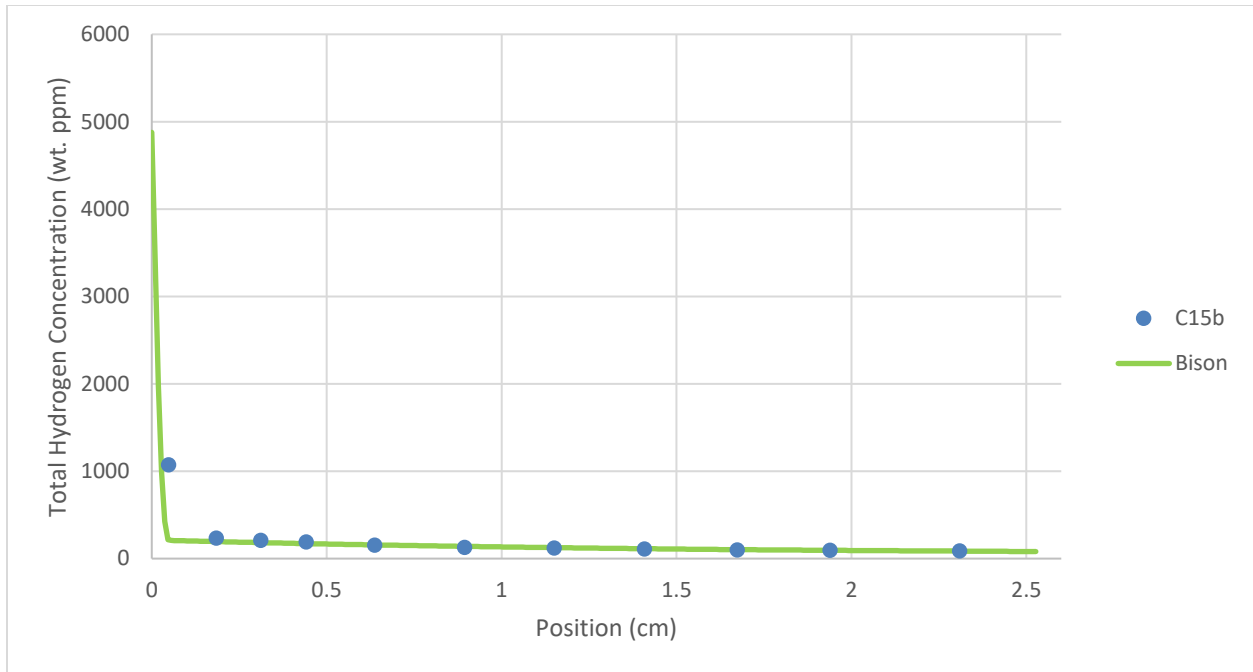


Figure 39: Specimen C15b annealed for 18 days in linear temperature gradient from 371°C to 538°C (66°C/cm) with initial homogeneous hydrogen concentration of 167 wt. ppm.

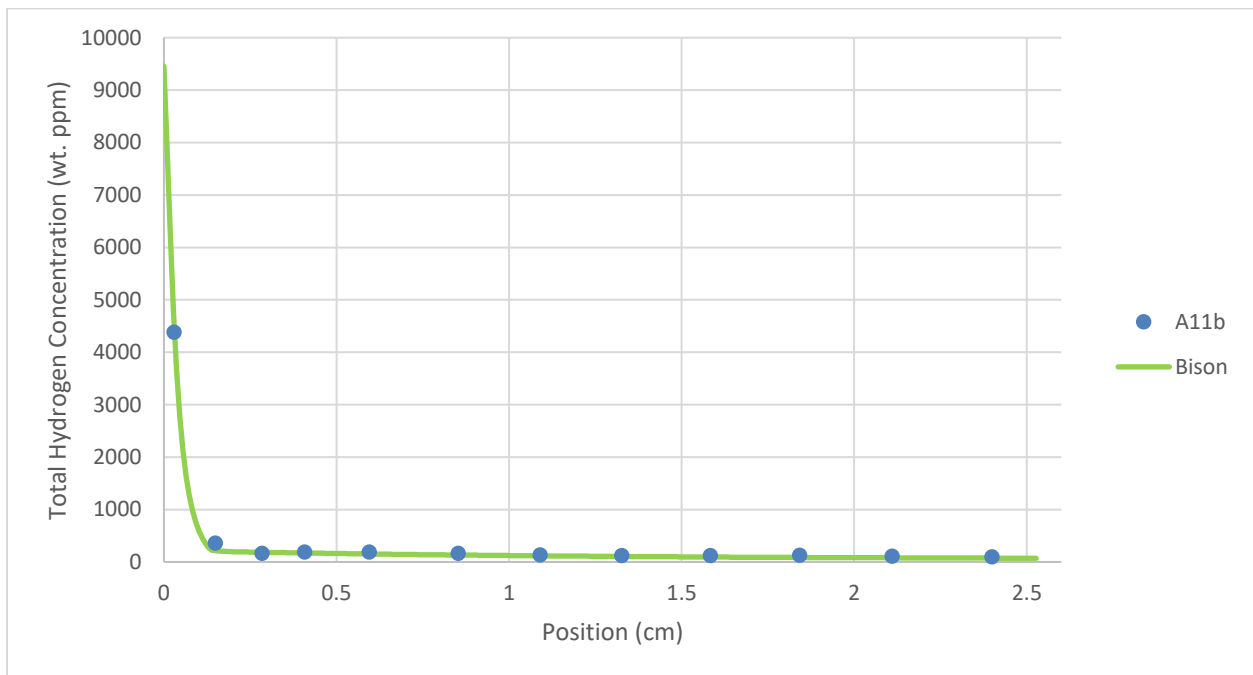


Figure 40: Specimen A11b annealed for 20 days in linear temperature gradient from 371°C to 593°C (87°C/cm) with initial homogeneous hydrogen concentration of 265 wt. ppm.

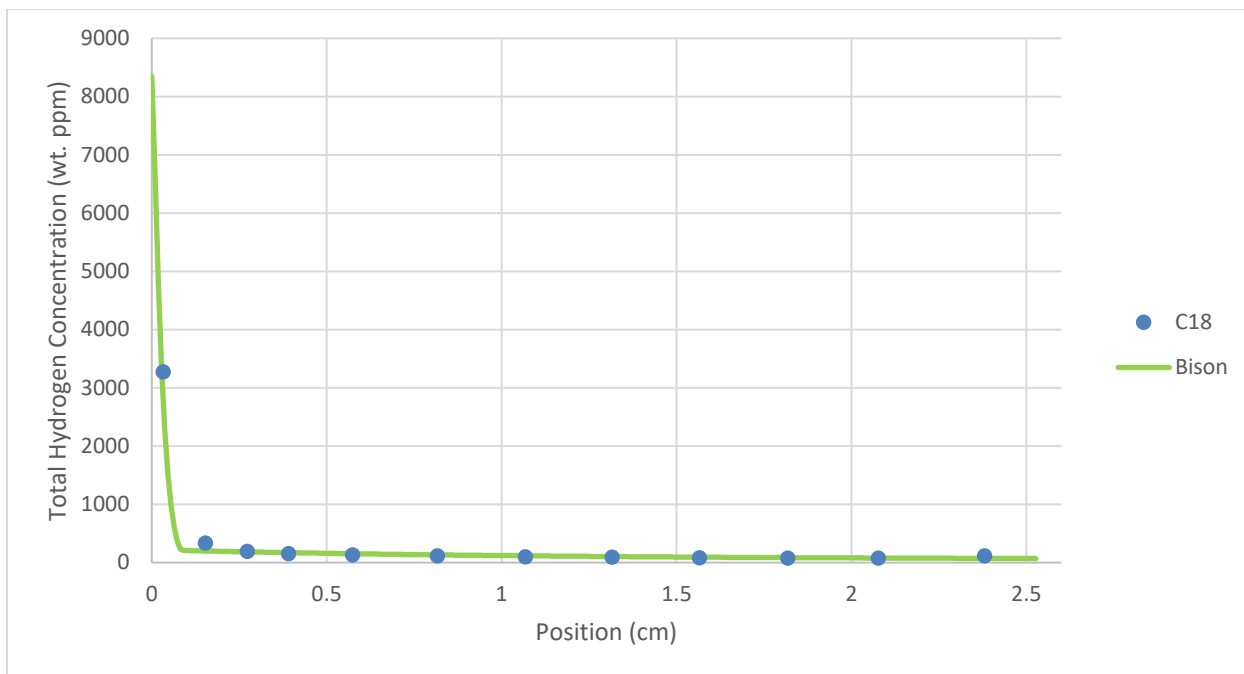


Figure 41: Specimen C18 annealed for 20 days in linear temperature gradient from 371°C to 593°C (87°C/cm) with initial homogeneous hydrogen concentration of 215 wt. ppm.

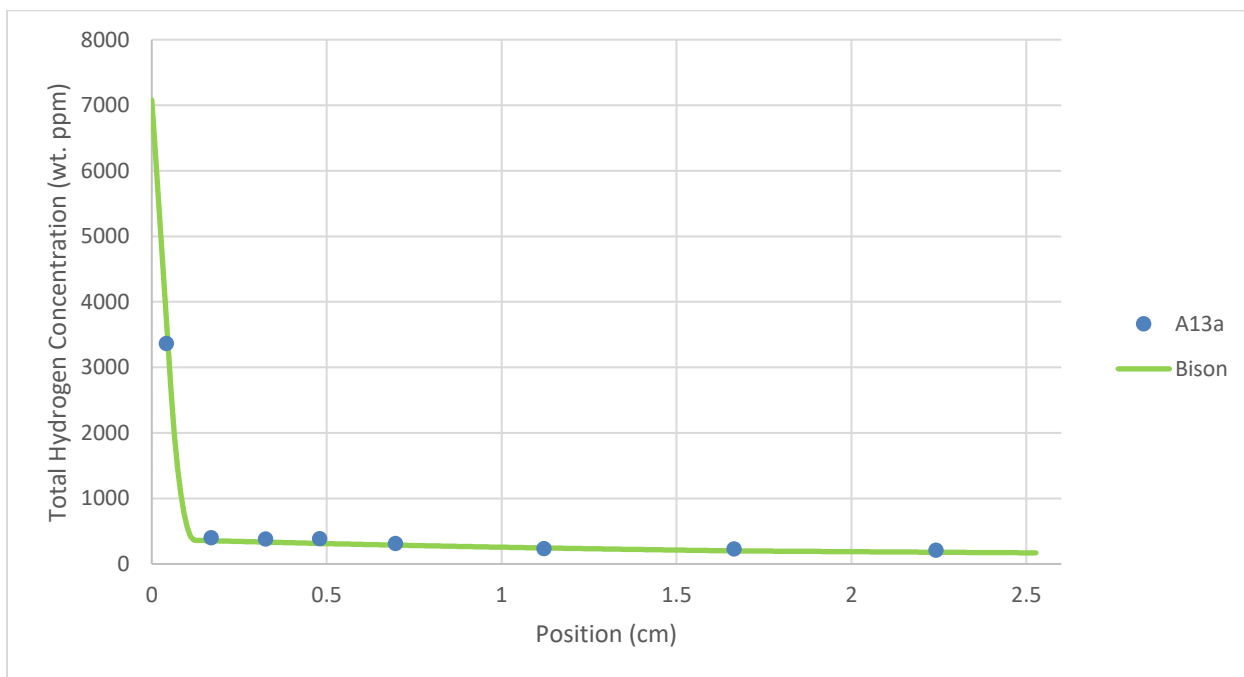


Figure 42: Specimen A13a annealed for 6 days in linear temperature gradient from 427°C to 621°C (77°C/cm) with initial homogeneous hydrogen concentration of 372 wt. ppm.

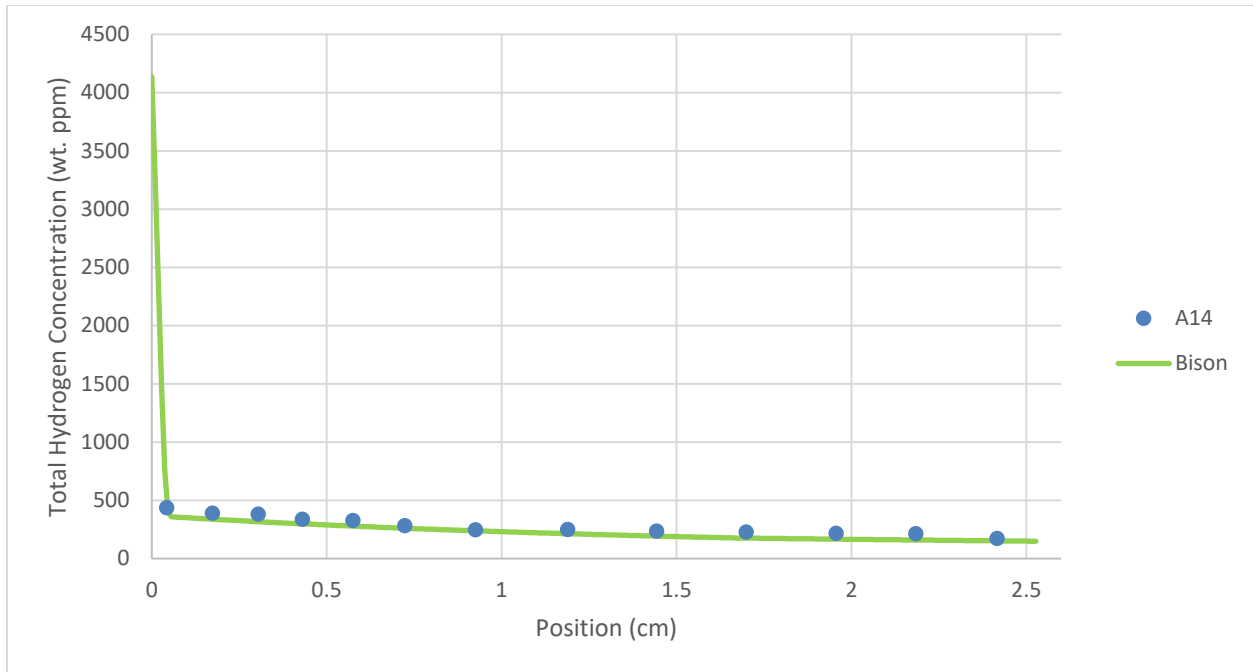


Figure 43: Specimen A14 annealed for 6 days in linear temperature gradient from 427°C to 621°C (77°C/cm) with initial homogeneous hydrogen concentration of 261 wt. ppm.

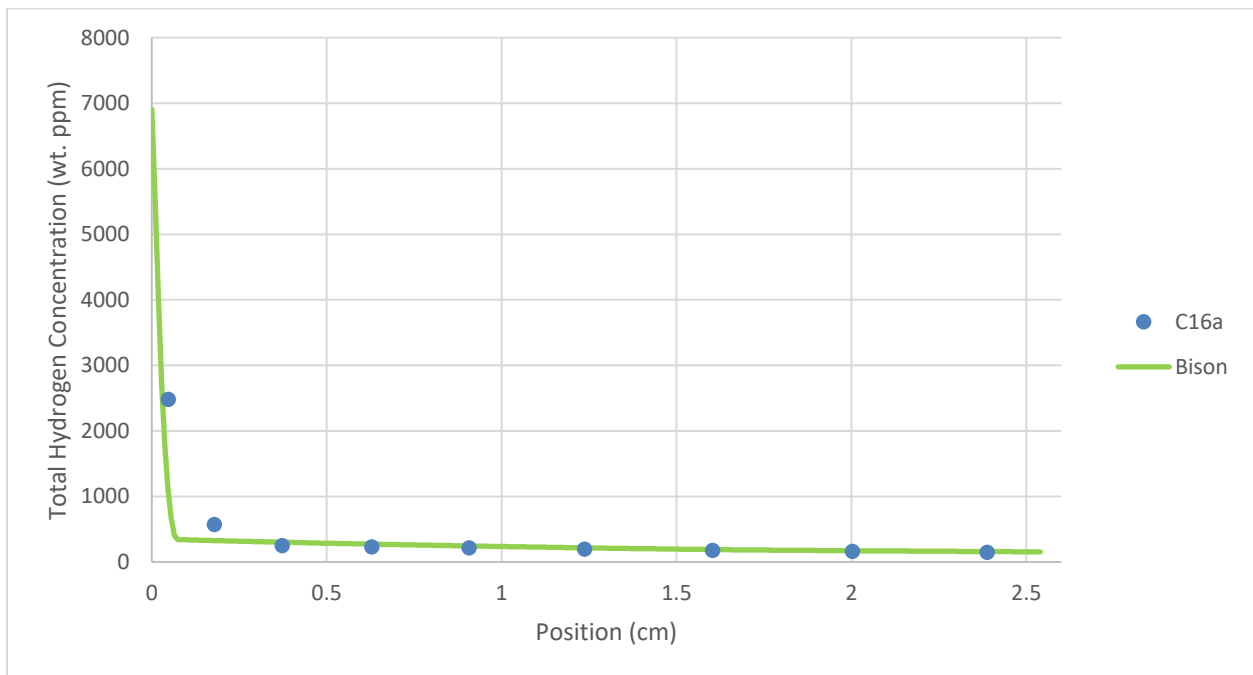


Figure 44: Specimen C16a annealed for 14 days in linear temperature gradient from 427°C to 593°C (66°C/cm) with initial homogeneous hydrogen concentration of 299 wt. ppm.

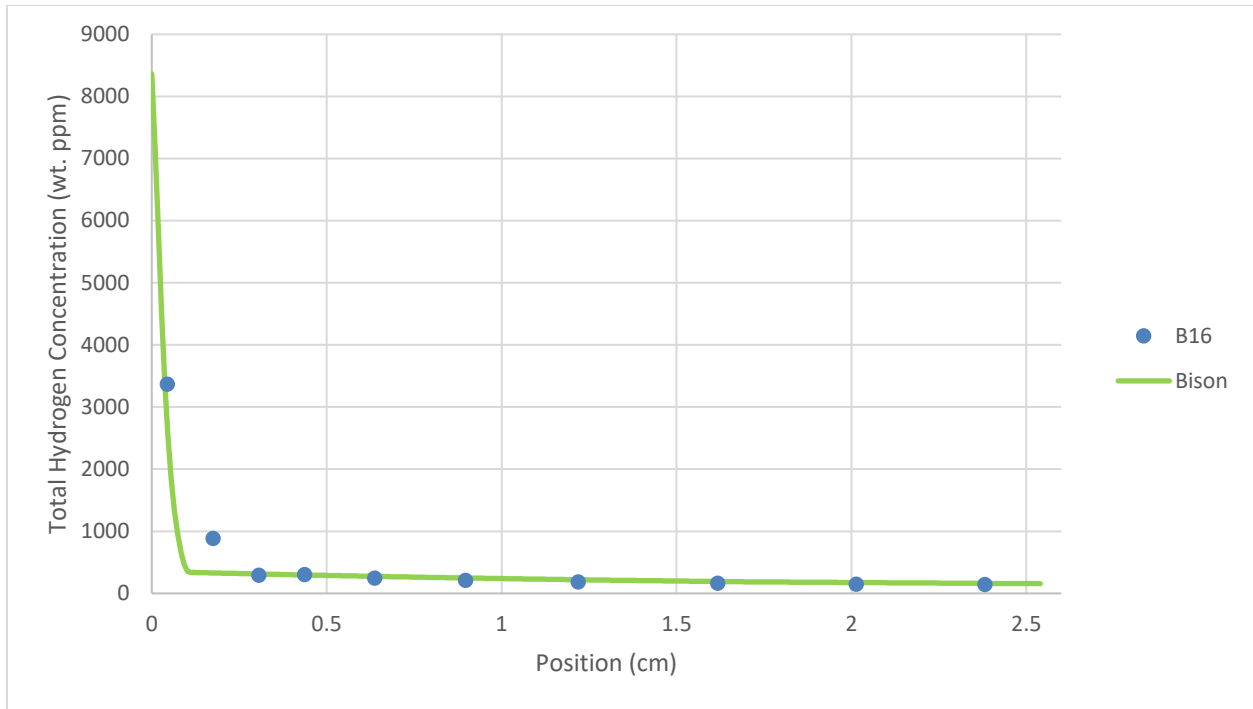


Figure 45: Specimen B16 annealed for 14 days in linear temperature gradient from 427°C to 593°C (66°C/cm) with initial homogeneous hydrogen concentration of 348 wt. ppm.

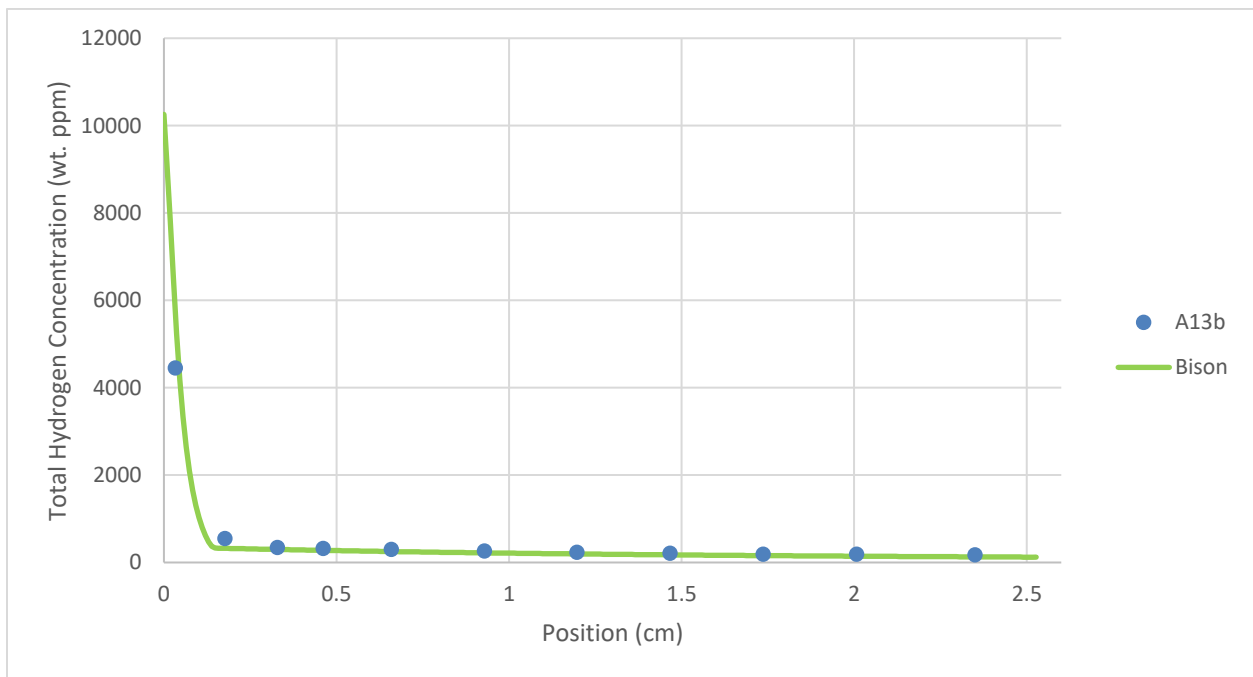


Figure 46: Specimen A13b annealed for 12 days in linear temperature gradient from 427°C to 649°C (87°C/cm) with initial homogeneous hydrogen concentration of 392 wt. ppm.

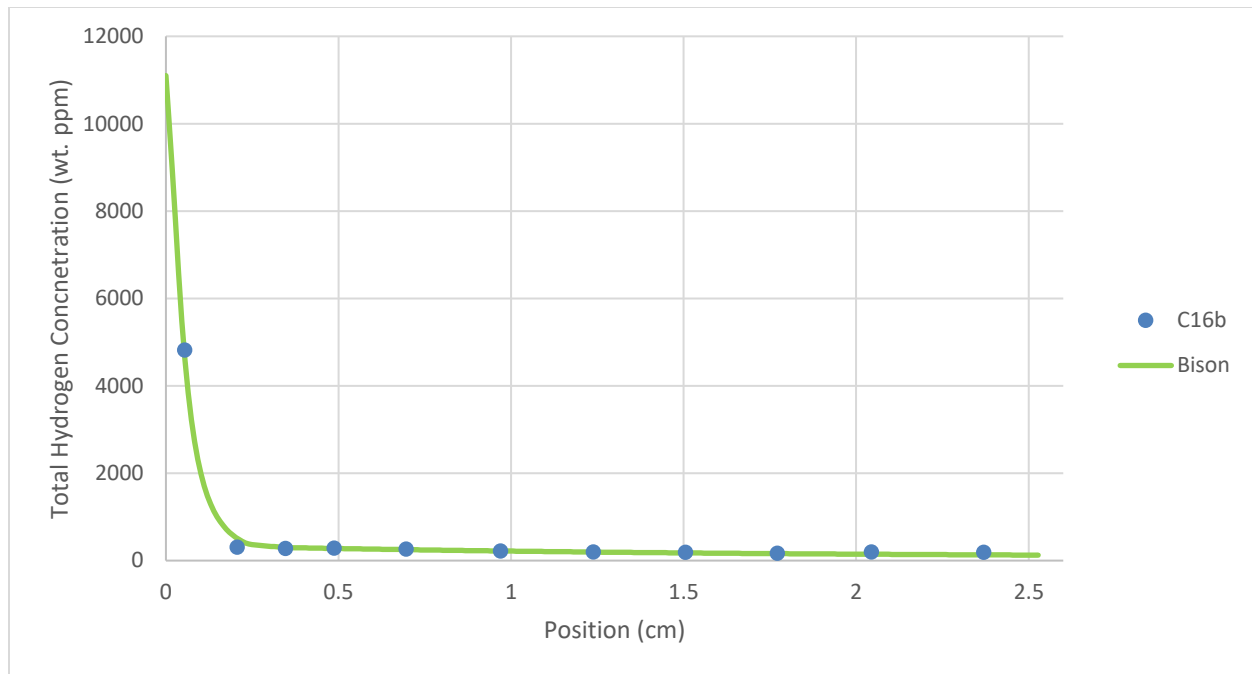


Figure 47: Specimen C16b annealed for 12 days in linear temperature gradient from 427°C to 649°C (87°C/cm) with initial homogeneous hydrogen concentration of 468 wt. ppm.

4.2.2. Experiment 2 Data Models

Figures 48 – 52 compare hydrogen distribution simulations as a function of specimen position with experiment 2 data found in Tables A15 – A18 of Appendix A. These figures continue to demonstrate how the accuracy of the BISON model decreases as the temperature distribution becomes more shallow and Fickian diffusion becomes a more important driving force. Because these specimens have a peak temperature towards the center of the specimen and a hotter end temperature with a hydride rim, hydrides should dissolve from the rim into solid solution to generate a concentration gradient that acts against the thermal gradient. As hydrogen is driven by the concentration gradient, more hydrides should dissolve into solid solution at the end of the specimen, further increasing the driving force of the concentration gradient. This should occur as hydrogen in solid solution diffuses to the peak temperature location. At this location, the thermal gradient should drive the hydrogen to the colder end of the specimen where increasing hydrogen concentrations should eventually lead to hydride precipitation in all specimens. If the annealing time is long enough (hundreds or thousands of days), equilibrium should eventually be reached in which hydrides exist at the colder side and hotter side in a manner inversely proportional to their temperatures.

Figures 48 and 49 are the only simulations that predict hydride formation at the colder side, despite a fairly large thermal gradient driving hydrogen from the peak temperature to the hotter end. Figure 49 represents the amount of simulated annealing time needed to start hydride precipitation (hydride concentration of about 5 wt. ppm present in the coldest part of specimen

A56 at the end of simulated annealing), and Figure 48 represents a much longer annealing time in which a colder-side hydride concentration of about 550 wt. ppm is simulated. However, BISON still did not predict the gradual increase in hydride formation that was experimentally observed with a shallow cold side thermal gradient. Figures 51 and 52 depict experiments with a long annealing time and small thermal gradients, which together lead to large concentration effects and hydride formation at the colder end of the specimen. However, this result was not predicted by BISON.

To explain the experiment 2 simulation results, consider the model at equilibrium, where the distribution of hydrogen in solid solution, TSSp, and TSSd can be determined by Equations 4, 5, and 6, respectively. At equilibrium, the amount of hydrogen in solid solution at the hotter end of the specimen ($C_{ss,hotter}$) will be equal to TSSd, as the hydride rim dissolves into soluble hydrogen. As hydrides dissolve, diffusion occurs and the equilibrium concentration of hydrogen in solid solution at the peak temperature ($C_{ss,peak}$) and colder end ($C_{ss,colder}$) can be determined by manipulating Equation 4, as seen in Equations 12 and 13. From Equation 12, as the temperature gradient between the peak temperature and the hotter end becomes more steep, the equilibrium concentration of soluble hydrogen at the peak temperature decreases. Likewise, from Equation 13, as the temperature gradient between the peak temperature and colder end becomes more steep, the equilibrium concentration of soluble hydrogen at the colder end increases. Note that the initial homogenous hydrogen concentration, C_o , was modeled as 10 wt. ppm for all specimens.

$$\frac{C_{ss,peak}}{C_{ss,hotter}} = \frac{C_o \exp\left(\frac{Q^*}{RT_{peak}}\right)}{C_o \exp\left(\frac{Q^*}{RT_{hotter}}\right)} \rightarrow C_{ss,peak} = C_{ss,hotter} \exp\left[\frac{Q^*}{R} \left(\frac{1}{T_{peak}} - \frac{1}{T_{hotter}}\right)\right] \quad (12)$$

$$\frac{C_{ss,colder}}{C_{ss,peak}} = \frac{C_o \exp\left(\frac{Q^*}{RT_{colder}}\right)}{C_o \exp\left(\frac{Q^*}{RT_{peak}}\right)} \rightarrow C_{ss,colder} = C_{ss,peak} \exp\left[\frac{Q^*}{R} \left(\frac{1}{T_{colder}} - \frac{1}{T_{peak}}\right)\right] \quad (13)$$

For the simulations involved with Figures 48 and 49, the equilibrium concentrations of soluble hydrogen at the colder ends were greater than TSSp and precipitation occurred. For the simulation involved with Figure 50, the equilibrium concentration of soluble hydrogen at the colder end was about equal to TSSp, precipitation kinetics had a negligible effect, and precipitation did not occur. For the simulations involved with Figures 51 and 52, the equilibrium concentrations of soluble hydrogen at the colder ends were less than TSSp, diffusion essentially stopped once equilibrium values were reached, and precipitation did not occur. The BISON Long Run presented in Figure 52 was done to ensure that the system reached equilibrium.

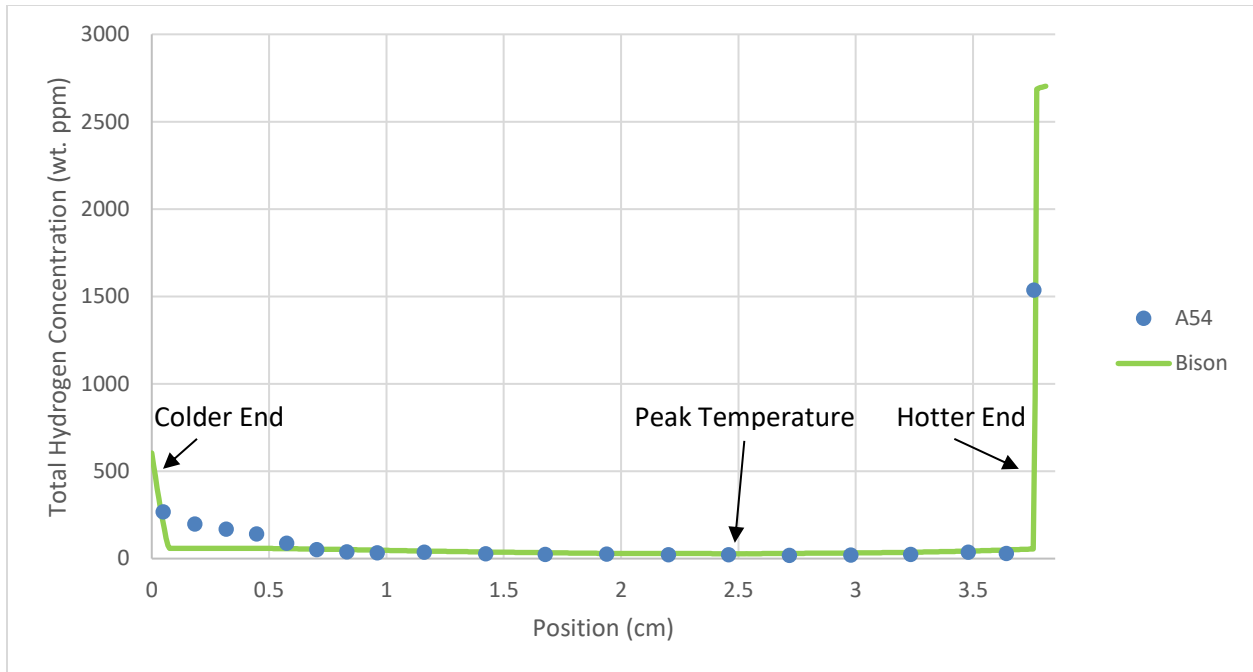


Figure 48: Specimen A54 annealed for 194 days in asymmetric 260°C-371°C-302°C temperature distribution (44°C/cm-54°C/cm) with initial homogeneous hydrogen concentration of 10 wt. ppm and hotter end hydride concentration of 2675 wt. ppm.

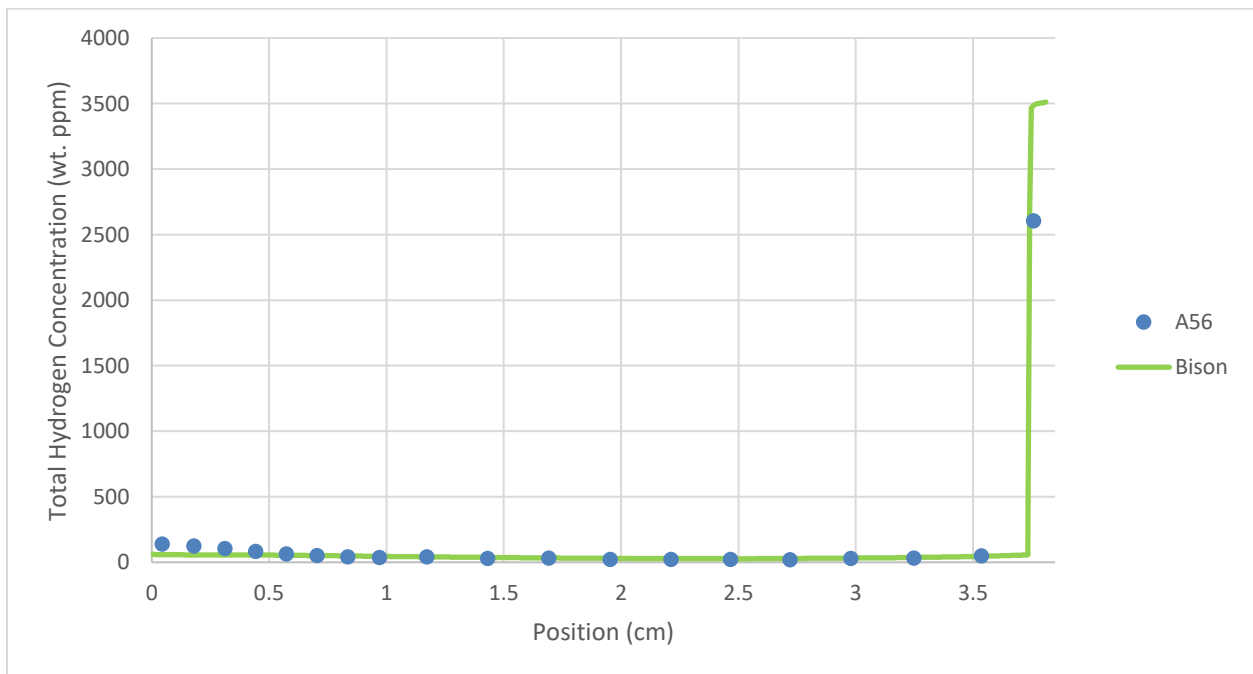


Figure 49: Specimen A56 annealed for 95 days in asymmetric 260°C-371°C-302°C temperature distribution (44°C/cm-54°C/cm) with initial homogeneous hydrogen concentration of 10 wt. ppm and hotter end hydride concentration of 3478 wt. ppm.

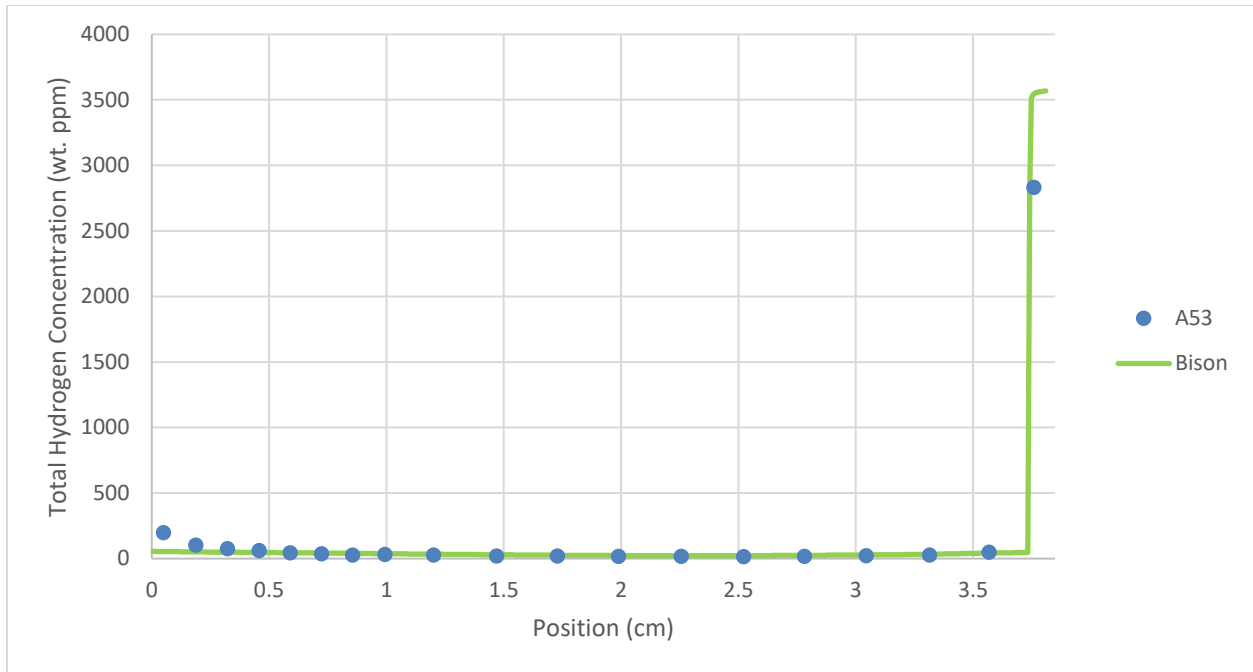


Figure 50: Specimen A53 annealed for 150 days in asymmetric 260°C-371°C-288°C temperature distribution (44°C/cm-65°C/cm) with initial homogeneous hydrogen concentration of 10 wt. ppm and hotter end hydride concentration of 3542 wt. ppm.

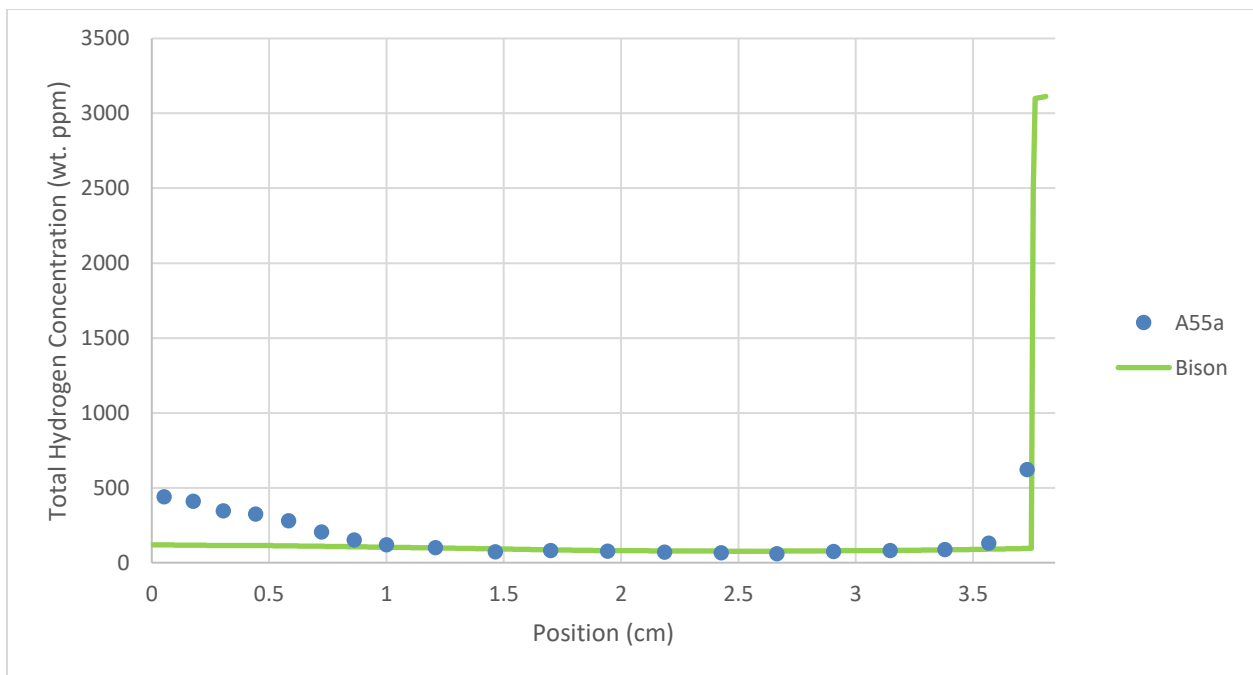


Figure 51: Specimen A55a annealed for 209 days in asymmetric 316°C-371°C-343°C temperature distribution (22°C/cm-22°C/cm) with initial homogeneous hydrogen concentration of 10 wt. ppm and hotter end hydride concentration of 3077 wt. ppm.

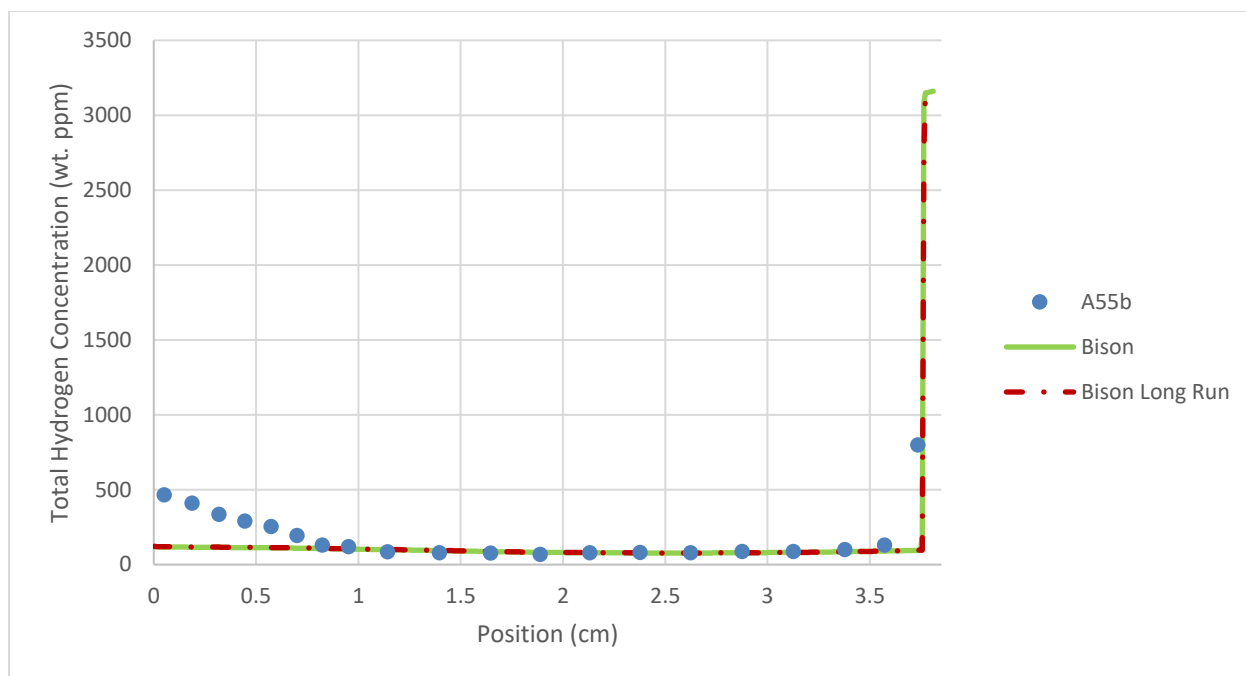


Figure 52: Specimen A55b annealed for 209 days in asymmetric 316°C-371°C-343°C temperature distribution (22°C/cm-22°C/cm) with initial homogeneous hydrogen concentration of 10 wt. ppm and hotter end hydride concentration of 3125 wt. ppm. BISON Long Run represents a simulation of 1000 days.

As seen in Figures 20 – 52, this empirical data does not completely agree with the accepted hypothesis that the presence of hydrides favors additional hydride precipitation. This hypothesis is based on the fact that zirconium hydride precipitation introduces hydrogen to the zirconium matrix, which causes particle volume increase, matrix strain, and lattice widening. The resulting elastic strain energy fields then act as nucleation sites for additional hydride precipitation. Therefore, this hypothesis explains why nanoscale hydride discs overlap in close proximity to form microscale platelets in areas such as the hydride rim [42].

However, the hypothesis does not account for a hydride concentration at which elastic strain energy fields supersaturate and further hydride precipitation becomes unfavorable. If the elastic strain energy fields did not supersaturate and neighboring hydride sites were always favorable for further nucleation, then the experimental data would better resemble simulation results. Specifically, in the linear temperature gradients, hydrides would only form in the coldest regions of the specimen, and in the asymmetric temperature gradients, hydrides would not depart from the hydride rim. However, the empirical data favors the idea that at a certain point, as hydride concentration increases, more hydrogen in solid solution is needed to cause further precipitation.

5. Conclusion and Future Work

The empirical data presented in this paper provides a deeper understanding of hydrogen behavior in unirradiated Zircaloy-4, Zircaloy-1% Niobium, and Zircaloy-2.5% Niobium in stress-free thermal environments. This experimental data compares well with existing literature and can be used to determine empirical values for the heat of transport, diffusion frequency factor, and diffusion activation energy, which are used in mathematical equations to describe thermal diffusion of hydrogen and precipitation of zirconium hydride.

This data was also used to validate and understand the applicability of the BISON code when predicting hydrogen behavior in zirconium alloys. The BISON code is a mathematical model that relies on empirical values. As seen from the results of this paper, BISON simulations perform well in steep thermal gradients but over predict the amount of hydrides in colder regions as the thermal gradient becomes more shallow. In order to mimic the gradual change in hydride concentration seen in experimentation, BISON users can manipulate a parameter called the clamping factor to reduce the maximum allowed concentration of hydrides. Because this parameter artificially controls hydrogen distribution and morphology, the clamping factor is not practical for real-world applications. As a result, more information is needed to understand the effects of microstructure and zirconium alloy composition on hydride precipitation. For instance, hydrogen in specimens containing niobium tended to precipitate at slightly lower concentrations than hydrogen in Zircaloy-4 specimens under the same conditions. Likewise, heat of transport values varied slightly with temperature and were slightly lower for zirconium specimens containing niobium. Further improvements can be made to the BISON software by altering hard-coded input parameters for different zirconium alloys and creating functions to describe how these input parameters change with temperature. Additional experimentation is needed to observe the effects of microstructure on hydride precipitation behavior. These experiments could be conducted by maintaining the zirconium alloy content and thermal gradient and varying the tightly controlled microstructure of the specimens.

6. Acknowledgments

I would like to thank Bruce Kammenzind for not only providing the data that made this paper possible but taking the time out of his busy schedule to be my project sponsor. Mr. Kammenzind has made enormous contributions to a variety of fields related to nuclear materials, and it was an honor to work and converse with him as the project developed. I would also like to thank Mr. Kammenzind's team for taking the time to provide user manuals and assistance when needed so that I could successfully model the experiments with the BISON code.

I would like to thank Dr. Arthur Motta for being my faculty advisor and providing an extensive list of background material that allowed me to gain the prerequisite knowledge necessary to complete this project. In my many years of undergraduate and graduate school at the Pennsylvania State University, Dr. Motta has been a continual source of inspiration through his countless contributions to the nuclear sciences and dedication to his students.

Finally, I would like to thank Dr. William Walters for taking the time to be a secondary reader and providing perspective that could only come from someone who specializes outside of the material sciences.

7. Appendix A

Experiment 1 Data Sets

Tables A1 - A14 present annealing data for specimens involved with experiment 1.

Table A1: Data for specimens A26a and A27, which were annealed for twenty-seven days in a linear temperature gradient that ranged from 260°C to 427°C.

Thermocouple Location (cm)	0.089	0.838	1.676	2.451
Average Thermocouple Temperature (°C)	260.9	317.0	387.1	431.0

A26a				
Sample ID	Sample Length (cm)	Midpoint Location (cm)	Midpoint Temperature (°C)	Hydrogen Concentration (wt. ppm)
H1	0.095	0.048	257.8	198
H2	0.092	0.183	267.9	86
H3	0.086	0.313	277.7	92
H4	0.087	0.441	287.2	93
H5	0.226	0.639	302.1	54
H6	0.211	0.899	322.1	53
H7	0.486	1.288	354.7	33
H8	0.478	1.812	394.8	25
H9	0.435	2.310	423.0	24
A27				
Sample ID	Sample Length (cm)	Midpoint Location (cm)	Midpoint Temperature (°C)	Hydrogen Concentration (wt. ppm)
H1	0.093	0.047	257.7	48
H2	0.098	0.180	267.7	100
H3	0.088	0.310	277.4	84
H4	0.086	0.434	286.7	83
H5	0.234	0.632	301.5	46
H6	0.206	0.889	321.2	51
H7	0.478	1.269	353.0	28
H8	0.469	1.780	393.0	20
H9	0.476	2.289	421.9	21

Table A2: Data for specimens A45 and A46, which were annealed for seventy-seven days in a linear temperature gradient that ranged from 260°C to 427°C.

Thermocouple Location (cm)	0.089	0.381	0.838	1.676	2.451
Average Thermocouple Temperature (°C)	260.8	282.1	310.4	382.5	435.0

A45				
Sample ID	Sample Length (cm)	Midpoint Location (cm)	Midpoint Temperature (°C)	Hydrogen Concentration (wt. ppm)
H1	0.086	0.043	257.4	1043
H2	0.097	0.175	267.1	232
H3	0.087	0.308	276.8	88
H4	0.087	0.436	285.5	59
H5	0.087	0.564	293.4	55
H6	0.085	0.691	301.3	48
H7	0.212	0.880	314.1	43
H8	0.212	1.133	335.8	33
H9	0.212	1.387	357.6	29
H10	0.212	1.640	379.4	24
H11	0.209	1.891	397.1	23
H12	0.214	2.144	414.2	21
H13	0.236	2.409	432.2	13
A46				
Sample ID	Sample Length (cm)	Midpoint Location (cm)	Midpoint Temperature (°C)	Hydrogen Concentration (wt. ppm)
H1	0.088	0.044	257.5	1215
H2	0.096	0.177	267.2	330
H3	0.089	0.310	276.9	210
H4	0.092	0.442	285.9	102
H5	0.086	0.572	293.9	50
H6	0.086	0.699	301.8	39
H7	0.226	0.896	315.4	26
H8	0.216	1.158	338.0	26
H9	0.209	1.412	359.8	25
H10	0.213	1.664	381.5	19
H11	0.202	1.913	398.6	15
H12	0.212	2.162	415.4	15
H13	0.218	2.418	432.8	21

Table A3: Data for specimens A26b and C13, which were annealed for fifty-four days in a linear temperature gradient that ranged from 260°C to 482°C.

Thermocouple Location (cm)	0.089	0.838	1.676	2.451
Average Thermocouple Temperature (°C)	259.0	350.9	428.3	478.3

A26b				
Sample ID	Sample Length (cm)	Midpoint Location (cm)	Midpoint Temperature (°C)	Hydrogen Concentration (wt. ppm)
H1	0.091	0.046	253.7	532
H2	0.090	0.175	269.5	92
H3	0.086	0.301	285.1	42
H4	0.096	0.431	300.9	45
H5	0.085	0.560	316.8	39
H6	0.085	0.684	331.9	35
H7	0.247	0.889	355.5	26
H8	0.210	1.156	380.2	20
H9	0.241	1.421	404.7	19
H10	0.213	1.687	428.9	17
H11	0.215	1.939	445.2	8
H12	0.147	2.158	459.4	8
H13	0.257	2.399	474.9	17
C13				
Sample ID	Sample Length (cm)	Midpoint Location (cm)	Midpoint Temperature (°C)	Hydrogen Concentration (wt. ppm)
H1	0.095	0.047	253.9	602
H2	0.085	0.176	269.7	55.5
H3	0.085	0.300	284.9	22
H4	0.090	0.426	300.3	33
H5	0.084	0.551	315.7	31
H6	0.226	0.745	339.4	29
H7	0.213	1.003	366.1	17
H8	0.219	1.258	389.7	14
H9	0.218	1.516	413.5	14
H10	0.239	1.783	435.2	22
H11	0.213	2.048	452.2	12
H12	0.335	2.360	472.4	21

Table A4: Data for specimens A09a and A10a, which were annealed for fifteen days in a linear temperature gradient that ranged from 316°C to 482°C.

Thermocouple Location (cm)	0.089	0.838	1.676	2.451
Average Thermocouple Temperature (°C)	308.5	366.4	433.7	483.6

A09a				
Sample ID	Sample Length (cm)	Midpoint Location (cm)	Midpoint Temperature (°C)	Hydrogen Concentration (wt. ppm)
H1	0.102	0.051	305.5	106
H2	0.100	0.192	316.5	104
H3	0.120	0.342	328.1	86
H4	0.128	0.507	340.8	73
H5	0.270	0.746	359.3	59
H6	0.511	1.177	393.6	34
H7	0.516	1.731	437.2	34
H8	0.499	2.278	472.5	33
A10a				
Sample ID	Sample Length (cm)	Midpoint Location (cm)	Midpoint Temperature (°C)	Hydrogen Concentration (wt. ppm)
H1	0.130	0.065	306.6	131
H2	0.110	0.226	319.1	122
H3	0.104	0.373	330.5	117
H4	0.110	0.520	341.8	105
H5	0.268	0.750	359.6	79
H6	0.523	1.185	394.3	55
H7	0.504	1.740	437.8	38
H8	0.495	2.280	472.6	40

Table A5: Data for specimens A09b and A10b, which were annealed for thirty-two days in a linear temperature gradient that ranged from 316°C to 482°C.

Thermocouple Location (cm)	0.089	0.838	1.676	2.451
Average Thermocouple Temperature (°C)	317.8	368.7	439.5	482.0

A09b				
Sample ID	Sample Length (cm)	Midpoint Location (cm)	Midpoint Temperature (°C)	Hydrogen Concentration (wt. ppm)
H1	0.097	0.048	315.1	764
H2	0.100	0.185	324.3	178
H3	0.097	0.322	333.6	146
H4	0.090	0.454	342.6	146
H5	0.231	0.652	356.0	110
H6	0.475	1.044	386.0	79
H7	0.482	1.561	429.7	58
H8	0.687	2.184	467.4	49
A10b				
Sample ID	Sample Length (cm)	Midpoint Location (cm)	Midpoint Temperature (°C)	Hydrogen Concentration (wt. ppm)
H1	0.100	0.050	315.2	136
H2	0.093	0.188	324.5	117
H3	0.100	0.327	334.0	114
H4	0.090	0.464	343.3	102
H5	0.242	0.672	357.4	75
H6	0.488	1.080	389.1	58
H7	0.481	1.607	433.7	45
H8	0.638	2.209	468.7	38

Table A6: Data for specimens A31 and C14a, which were annealed for twenty-six days in a linear temperature gradient that ranged from 316°C to 538°C.

Thermocouple Location (cm)	0.089	0.838	1.676	2.451
Average Thermocouple Temperature (°C)	316.5	402.1	485.4	529.9

A31				
Sample ID	Sample Length (cm)	Midpoint Location (cm)	Midpoint Temperature (°C)	Hydrogen Concentration (wt. ppm)
H1	0.086	0.043	311.3	2745
H2	0.098	0.178	326.7	245
H3	0.090	0.316	342.4	123
H4	0.099	0.454	358.2	108
H5	0.087	0.590	373.8	98
H6	0.091	0.723	389.0	77
H7	0.225	0.925	410.7	70
H8	0.213	1.188	436.8	58
H9	0.229	1.452	463.1	54
H10	0.211	1.715	487.6	46
H11	0.231	1.980	502.8	40
H12	0.389	2.333	523.1	55
C14a				
Sample ID	Sample Length (cm)	Midpoint Location (cm)	Midpoint Temperature (°C)	Hydrogen Concentration (wt. ppm)
H1	0.090	0.045	311.5	2051
H2	0.095	0.181	327.0	425
H3	0.086	0.314	342.2	91
H4	0.103	0.452	358.0	71
H5	0.081	0.586	373.3	57
H6	0.114	0.727	389.4	60
H7	0.202	0.928	411.1	51
H8	0.226	1.186	436.6	45
H9	0.214	1.449	462.8	41
H10	0.226	1.712	487.4	36
H11	0.209	1.972	502.4	35
H12	0.408	2.323	522.5	33

Table A7: Data for specimens B14 and C14b, which were annealed for thirty-two days in a linear temperature gradient that ranged from 316°C to 482°C.

Thermocouple Location (cm)	0.089	0.838	1.676	2.451
Average Thermocouple Temperature (°C)	316.7	373.5	437.9	480.0

B14				
Sample ID	Sample Length (cm)	Midpoint Location (cm)	Midpoint Temperature (°C)	Hydrogen Concentration (wt. ppm)
H1	0.089	0.045	313.3	997
H2	0.088	0.172	323.0	320
H3	0.092	0.301	332.7	176
H4	0.089	0.430	342.6	126
H5	0.216	0.622	357.1	70
H6	0.223	0.880	376.7	77
H7	0.347	1.203	401.6	51
H8	0.341	1.585	431.0	43
H9	0.346	1.968	453.7	36
H10	0.352	2.356	474.8	38
C14b				
Sample ID	Sample Length (cm)	Midpoint Location (cm)	Midpoint Temperature (°C)	Hydrogen Concentration (wt. ppm)
H1	0.094	0.047	313.5	668
H2	0.090	0.177	323.3	311
H3	0.093	0.306	333.1	108
H4	0.086	0.433	342.8	104
H5	0.229	0.628	357.6	76
H6	0.361	0.960	382.9	53
H7	0.350	1.353	413.1	37
H8	0.346	1.738	441.3	36
H9	0.239	2.067	459.2	41
H10	0.306	2.377	476.0	33

Table A8: Data for specimens A11a and A12a, which were annealed for nine days in a linear temperature gradient that ranged from 371°C to 538°C.

Thermocouple Location (cm)	0.089	0.838	1.676	2.451
Average Thermocouple Temperature (°C)	372.6	427.7	487.6	532.7

A11a				
Sample ID	Sample Length (cm)	Midpoint Location (cm)	Midpoint Temperature (°C)	Hydrogen Concentration (wt. ppm)
H1	0.128	0.064	370.8	359
H2	0.083	0.211	381.6	242
H3	0.105	0.348	391.7	208
H4	0.083	0.484	401.7	220
H5	0.242	0.688	416.7	174
H6	0.539	1.121	447.9	131
H7	0.504	1.684	488.0	107
H8	0.549	2.253	521.1	94
A12a				
Sample ID	Sample Length (cm)	Midpoint Location (cm)	Midpoint Temperature (°C)	Hydrogen Concentration (wt. ppm)
H1	0.146	0.073	371.5	870
H2	0.081	0.225	382.7	280
H3	0.134	0.372	393.4	245
H4	0.083	0.519	404.3	232
H5	0.235	0.717	418.9	199
H6	0.480	1.114	447.4	154
H7	0.502	1.644	485.2	127
H8	0.593	2.231	519.8	106

Table A9: Data for specimens B15 and C15a, which were annealed for fourteen days in a linear temperature gradient that ranged from 371°C to 538°C.

Thermocouple Location (cm)	0.089	0.838	1.676	2.451
Average Thermocouple Temperature (°C)	373.5	428.9	494.0	535.0

B15				
Sample ID	Sample Length (cm)	Midpoint Location (cm)	Midpoint Temperature (°C)	Hydrogen Concentration (wt. ppm)
H1	0.101	0.050	370.7	1090
H2	0.088	0.184	380.5	350
H3	0.098	0.316	390.3	197
H4	0.089	0.449	400.1	178
H5	0.232	0.648	414.8	140
H6	0.484	1.045	445.0	118
H7	0.477	1.565	485.4	100
H8	0.685	2.185	520.9	82
C15a				
Sample ID	Sample Length (cm)	Midpoint Location (cm)	Midpoint Temperature (°C)	Hydrogen Concentration (wt. ppm)
H1	0.100	0.050	370.7	595
H2	0.096	0.186	380.7	491
H3	0.103	0.324	390.9	176
H4	0.086	0.456	400.7	186
H5	0.232	0.654	415.2	148
H6	0.485	1.050	445.4	121
H7	0.488	1.575	486.2	102
H8	0.670	2.192	521.3	86

Table A10: Data for specimens A12b and C15b, which were annealed for eighteen days in a linear temperature gradient that ranged from 371°C to 538°C.

Thermocouple Location (cm)	0.089	0.838	1.676	2.451
Average Thermocouple Temperature (°C)	371.5	429.2	491.6	536.5

A12b				
Sample ID	Sample Length (cm)	Midpoint Location (cm)	Midpoint Temperature (°C)	Hydrogen Concentration (wt. ppm)
H1	0.096	0.048	368.3	918
H2	0.097	0.185	378.9	368
H3	0.086	0.318	389.1	241
H4	0.098	0.451	399.4	205
H5	0.212	0.647	414.5	156
H6	0.223	0.906	434.3	147
H7	0.214	1.166	453.6	132
H8	0.231	1.429	473.2	125
H9	0.218	1.694	492.6	111
H10	0.232	1.960	508.1	102
H11	0.410	2.323	529.0	92
C15b				
Sample ID	Sample Length (cm)	Midpoint Location (cm)	Midpoint Temperature (°C)	Hydrogen Concentration (wt. ppm)
H1	0.096	0.048	368.3	1074
H2	0.094	0.184	378.8	235
H3	0.079	0.312	388.7	210
H4	0.099	0.442	398.7	189
H5	0.211	0.637	413.8	153
H6	0.222	0.895	433.4	128
H7	0.209	1.150	452.5	120
H8	0.227	1.409	471.7	110
H9	0.223	1.674	491.4	99
H10	0.225	1.939	506.8	96
H11	0.435	2.310	528.3	89

Table A11: Data for specimens A11b and C18, which were annealed for twenty days in a linear temperature gradient that ranged from 371°C to 593°C.

Thermocouple Location (cm)	0.089	0.838	1.676	2.451
Average Thermocouple Temperature (°C)	376.4	453.2	530.6	582.2

A11b				
Sample ID	Sample Length (cm)	Midpoint Location (cm)	Midpoint Temperature (°C)	Hydrogen Concentration (wt. ppm)
H1	0.058	0.029	370.2	4378
H2	0.092	0.149	382.6	357
H3	0.087	0.284	396.4	162
H4	0.069	0.408	409.1	185
H5	0.214	0.595	428.3	188
H6	0.209	0.852	454.6	159
H7	0.175	1.090	476.5	133
H8	0.207	1.327	498.3	121
H9	0.215	1.583	522.0	118
H10	0.211	1.842	541.6	128
H11	0.233	2.110	559.4	106
H12	0.256	2.399	578.7	97
C18				
Sample ID	Sample Length (cm)	Midpoint Location (cm)	Midpoint Temperature (°C)	Hydrogen Concentration (wt. ppm)
H1	0.064	0.032	370.6	3274
H2	0.088	0.154	383.0	337
H3	0.060	0.273	395.3	192
H4	0.085	0.391	407.4	156
H5	0.190	0.574	426.2	130
H6	0.204	0.817	451.0	117
H7	0.208	1.068	474.5	97
H8	0.196	1.316	497.3	92
H9	0.213	1.566	520.4	84
H10	0.202	1.819	540.0	79
H11	0.224	2.077	557.2	77
H12	0.293	2.381	577.5	114

Table A12: Data for specimens A13a and A14, which were annealed for six days in a linear temperature gradient that ranged from 427°C to 621°C.

Thermocouple Location (cm)	0.089	0.838	1.676	2.451
Average Thermocouple Temperature (°C)	429.5	501.5	580.2	620.7

A13a				
Sample ID	Sample Length (cm)	Midpoint Location (cm)	Midpoint Temperature (°C)	Hydrogen Concentration (wt. ppm)
H1	0.084	0.042	425.0	3360
H2	0.091	0.170	437.3	400
H3	0.139	0.325	452.2	380
H4	0.091	0.480	467.0	381
H5	0.263	0.697	487.9	311
H6	0.505	1.121	528.1	231
H7	0.502	1.665	579.2	226
H8	0.571	2.242	609.7	206
A14				
Sample ID	Sample Length (cm)	Midpoint Location (cm)	Midpoint Temperature (°C)	Hydrogen Concentration (wt. ppm)
H1	0.086	0.043	425.1	436
H2	0.094	0.173	437.6	390
H3	0.087	0.304	450.2	383
H4	0.086	0.431	462.3	338
H5	0.122	0.575	476.2	326
H6	0.093	0.723	490.4	282
H7	0.231	0.926	509.7	247
H8	0.215	1.189	534.4	250
H9	0.213	1.443	558.3	236
H10	0.221	1.700	581.5	227
H11	0.213	1.957	594.9	218
H12	0.162	2.184	606.7	213
H13	0.222	2.416	618.9	174

Table A13: Data for specimens B16 and C16a, which were annealed for fourteen days in a linear temperature gradient that ranged from 427°C to 593°C.

Thermocouple Location (cm)	0.089	0.838	1.676	2.451
Average Thermocouple Temperature (°C)	424.4	479.8	544.1	582.6

C16a				
Sample ID	Sample Length (cm)	Midpoint Location (cm)	Midpoint Temperature (°C)	Hydrogen Concentration (wt. ppm)
H1	0.094	0.047	421.3	2480
H2	0.092	0.179	431.0	569
H3	0.220	0.373	445.4	245
H4	0.214	0.629	464.3	225
H5	0.266	0.907	485.1	212
H6	0.317	1.237	510.4	193
H7	0.339	1.604	538.5	173
H8	0.384	2.003	560.3	157
H9	0.310	2.388	579.4	142
B16				
Sample ID	Sample Length (cm)	Midpoint Location (cm)	Midpoint Temperature (°C)	Hydrogen Concentration (wt. ppm)
H1	0.089	0.045	421.1	3370
H2	0.094	0.175	430.8	883
H3	0.089	0.306	440.4	293
H4	0.094	0.436	450.1	301
H5	0.229	0.637	464.9	245
H6	0.213	0.897	484.3	212
H7	0.353	1.219	509.0	184
H8	0.368	1.618	539.6	164
H9	0.345	2.014	560.8	150
H10	0.313	2.382	579.1	143

Table A14: Data for specimens A13 and C16b, which were annealed for twelve days in a linear temperature gradient that ranged from 427°C to 649°C.

Thermocouple Location (cm)	0.089	0.838	1.676	2.451
Average Thermocouple Temperature (°C)	426.0	501.9	583.4	649.5

A13				
Sample ID	Sample Length (cm)	Midpoint Location (cm)	Midpoint Temperature (°C)	Hydrogen Concentration (wt. ppm)
H1	0.065	0.033	420.3	4460
H2	0.110	0.176	434.9	550
H3	0.084	0.329	450.4	344
H4	0.069	0.461	463.8	328
H5	0.214	0.659	483.8	306
H6	0.213	0.929	510.7	269
H7	0.211	1.197	536.7	240
H8	0.217	1.467	563.0	213
H9	0.210	1.736	588.5	197
H10	0.221	2.007	611.6	192
H11	0.354	2.350	640.9	182
C16b				
Sample ID	Sample Length (cm)	Midpoint Location (cm)	Midpoint Temperature (°C)	Hydrogen Concentration (wt. ppm)
H1	0.108	0.054	422.5	4823
H2	0.088	0.206	437.9	304
H3	0.084	0.346	452.1	278
H4	0.090	0.487	466.4	287
H5	0.219	0.696	487.5	267
H6	0.219	0.969	514.7	220
H7	0.210	1.238	540.8	199
H8	0.216	1.505	566.7	190
H9	0.209	1.772	591.5	170
H10	0.226	2.044	614.7	198
H11	0.316	2.369	642.5	188

Experiment 2 Data Sets

Tables A15 – A18 and Figures A1 – A4 present annealing data for specimens involved with experiment 2.

Table A15: Data for specimen A54, which was annealed for 194 days in an asymmetric 260°C -371°C-302°C temperature profile.

Thermocouple Location (cm)	0.089	0.254	0.508	0.762	1.334	1.905	2.540	3.175	3.493	3.721
Average Thermocouple Temperature (°C)	261.7	265.9	269.7	280.7	319.1	358.4	374.0	349.6	324.3	303.1

A54				
Sample ID	Sample Length (cm)	Midpoint Location (cm)	Midpoint Temperature (°C)	Hydrogen Concentration (wt. ppm)
H1	0.096	0.048	260.7	268
H2	0.090	0.184	264.1	198
H3	0.089	0.317	266.8	169
H4	0.084	0.446	268.8	141
H5	0.087	0.575	272.6	87.5
H6	0.083	0.703	278.2	51.5
H7	0.087	0.831	285.4	38
H8	0.086	0.961	294.1	33
H9	0.230	1.162	307.6	36
H10	0.207	1.424	325.3	27
H11	0.212	1.676	342.7	23
H12	0.225	1.938	359.2	25
H13	0.217	2.202	365.7	22
H14	0.207	2.458	371.9	22
H15	0.226	2.717	367.2	18
H16	0.212	2.979	357.1	21
H17	0.211	3.234	344.9	24
H18	0.192	3.479	325.4	36
H19	0.048	3.643	310.4	30
H20	0.100	3.760	299.5	1537

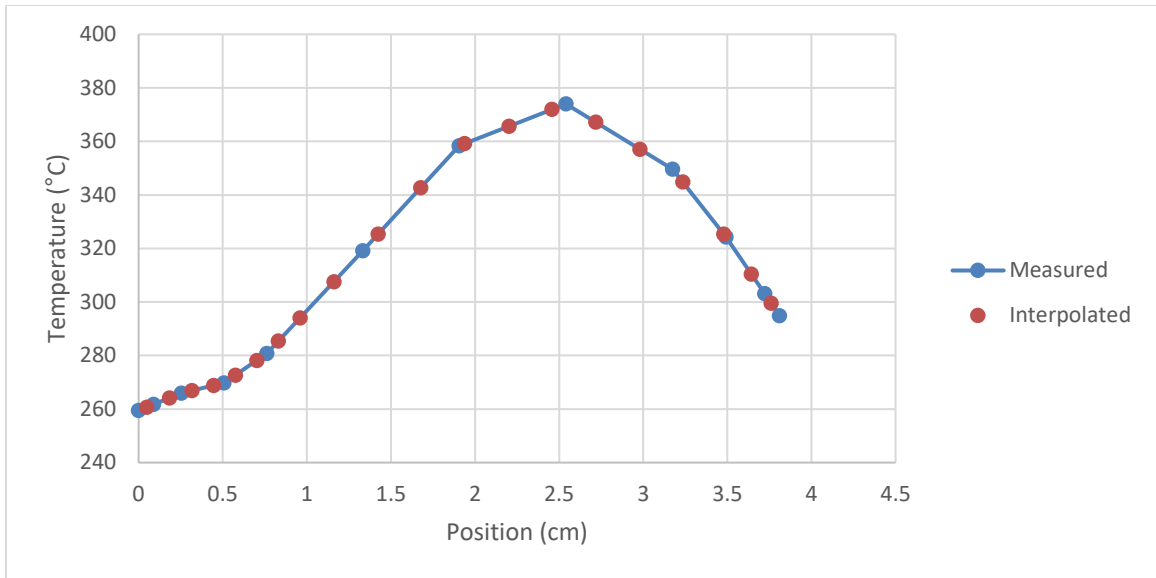


Figure A1: Specimen A54 temperature profile during annealing, as measured by the thermocouples and interpolated for each sample's midpoint.

Table A16: Data for specimen A56, which was annealed for 95 days in an asymmetric 260°C -371°C-302°C temperature profile.

Thermocouple Location (cm)	0.089	0.254	0.508	0.762	1.334	1.905	2.540	3.175	3.493	3.721
Average Thermocouple Temperature (°C)	261.1	264.7	268.1	279.1	314.6	352.3	374.9	350.1	326.9	303.3

A56				
Sample ID	Sample Length (cm)	Midpoint Location (cm)	Midpoint Temperature (°C)	Hydrogen Concentration (wt. ppm)
H1	0.089	0.045	260.1	138
H2	0.090	0.179	263.0	124
H3	0.084	0.312	265.5	104
H4	0.086	0.442	267.3	81.5
H5	0.085	0.573	271.0	64
H6	0.085	0.704	276.6	51
H7	0.086	0.835	283.6	41
H8	0.094	0.971	292.0	35
H9	0.217	1.172	304.5	42
H10	0.210	1.431	321.0	30
H11	0.220	1.691	338.2	31
H12	0.213	1.954	354.0	22
H13	0.213	2.212	363.2	21
H14	0.204	2.466	372.3	22
H15	0.212	2.720	367.9	20
H16	0.215	2.979	357.8	28
H17	0.234	3.248	344.7	31
H18	0.249	3.535	322.5	49
H19	0.105	3.758	299.5	2604

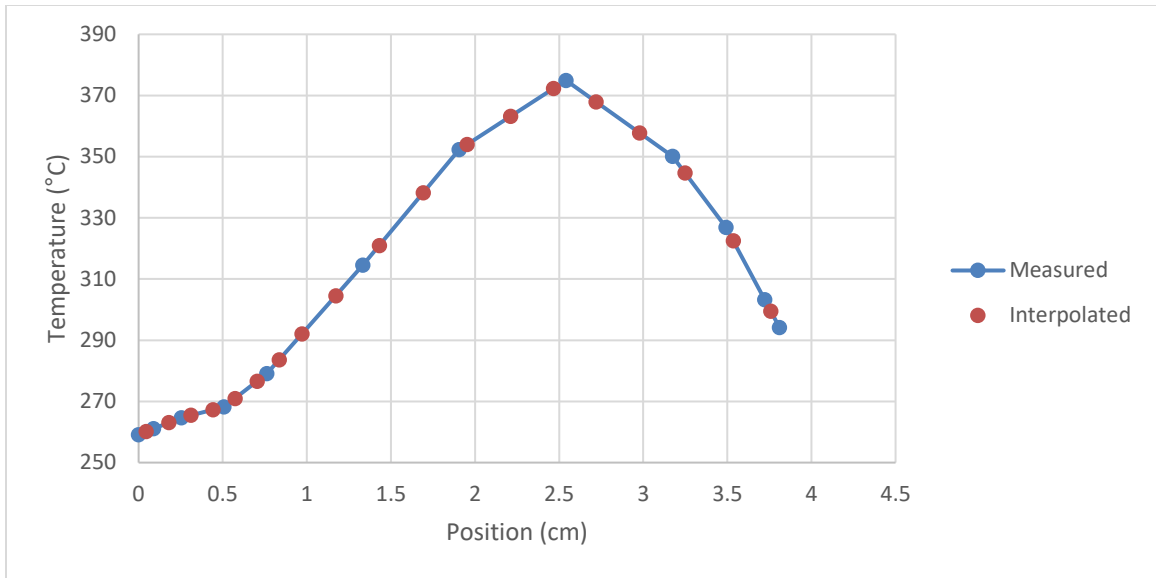


Figure A2: Specimen A56 temperature profile during annealing, as measured by the thermocouples and interpolated for each sample's midpoint.

Table A17: Data for specimen A53, which was annealed for 150 days in an asymmetric 260°C -371°C-288°C temperature profile.

Thermocouple Location (cm)	0.089	0.254	0.508	0.762	1.334	1.905	2.540	3.175	3.493	3.721
Average Thermocouple Temperature (°C)	260.9	267.9	276.6	286.7	320.1	360.9	371.4	337.5	305.7	289.1

A53				
Sample ID	Sample Length (cm)	Midpoint Location (cm)	Midpoint Temperature (°C)	Hydrogen Concentration (wt. ppm)
H1	0.101	0.050	259.3	197.5
H2	0.081	0.188	265.1	103
H3	0.095	0.323	270.3	75.5
H4	0.080	0.458	274.8	62
H5	0.091	0.590	279.9	43.5
H6	0.080	0.723	285.2	36.5
H7	0.092	0.856	292.2	28
H8	0.090	0.994	300.3	31
H9	0.230	1.201	312.3	28
H10	0.212	1.469	329.8	20
H11	0.213	1.729	348.3	19
H12	0.213	1.989	362.3	16
H13	0.227	2.256	366.7	17
H14	0.211	2.522	371.1	14
H15	0.214	2.781	358.5	18
H16	0.218	3.044	344.4	22
H17	0.227	3.314	323.5	27
H18	0.188	3.568	300.2	48
H19	0.101	3.760	286.3	2831

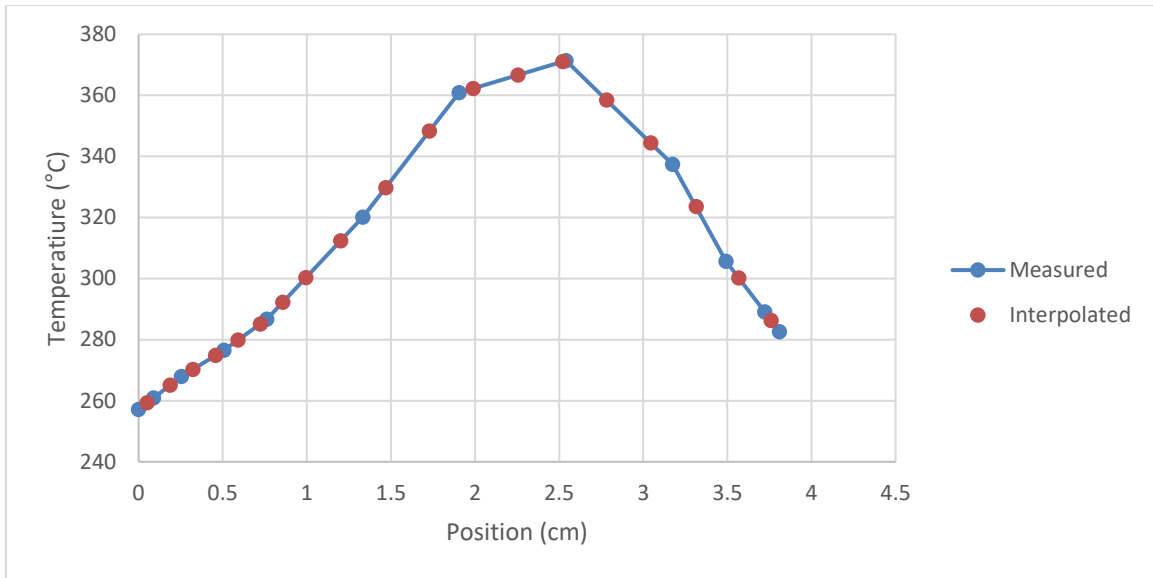


Figure A3: Specimen A53 temperature profile during annealing, as measured by the thermocouples and interpolated for each sample's midpoint.

Table A18: Data for specimens A55a and A55b, which were annealed for 209 days in an asymmetric 316°C -371°C-343°C temperature profile.

Thermocouple Location (cm)	0.089	0.254	0.508	0.762	1.334	1.905	2.540	3.175	3.493	3.721
Average Thermocouple Temperature (°C)	317.2	319.7	321.5	326.7	342.7	364.8	372.9	364.5	354.8	345.5

A55a				
Sample ID	Sample Length (cm)	Midpoint Location (cm)	Midpoint Temperature (°C)	Hydrogen Concentration (wt. ppm)
H1	0.104	0.052	316.6	440
H2	0.091	0.177	318.5	410
H3	0.110	0.305	320.0	345
H4	0.112	0.443	321.0	325
H5	0.113	0.582	323.0	280
H6	0.114	0.723	325.9	205
H7	0.110	0.863	329.5	150
H8	0.112	1.001	333.4	120
H9	0.249	1.208	339.2	100
H10	0.210	1.465	347.7	73
H11	0.208	1.701	356.9	81
H12	0.223	1.943	365.3	76
H13	0.209	2.186	368.4	70
H14	0.217	2.426	371.5	65
H15	0.205	2.664	371.3	60
H16	0.224	2.905	368.1	74
H17	0.206	3.147	364.9	80
H18	0.206	3.380	358.2	87
H19	0.114	3.567	351.7	130
H20	0.159	3.731	345.1	620
A55b				
Sample ID	Sample Length (cm)	Midpoint Location (cm)	Midpoint Temperature (°C)	Hydrogen Concentration (wt. ppm)
H1	0.102	0.051	316.6	465
H2	0.088	0.188	318.7	410
H3	0.089	0.318	320.1	335
H4	0.081	0.445	321.0	290
H5	0.089	0.573	322.8	255
H6	0.080	0.699	325.4	195
H7	0.085	0.824	328.4	130
H8	0.086	0.952	332.0	120
H9	0.212	1.143	337.4	86

H10	0.208	1.395	345.1	79
H11	0.210	1.646	354.8	76
H12	0.191	1.888	364.1	69
H13	0.210	2.131	367.7	78
H14	0.198	2.377	370.8	81
H15	0.212	2.624	371.8	79
H16	0.208	2.876	368.5	87
H17	0.207	3.126	365.2	88
H18	0.212	3.378	358.3	100
H19	0.091	3.572	351.5	130
H20	0.150	3.735	344.9	800

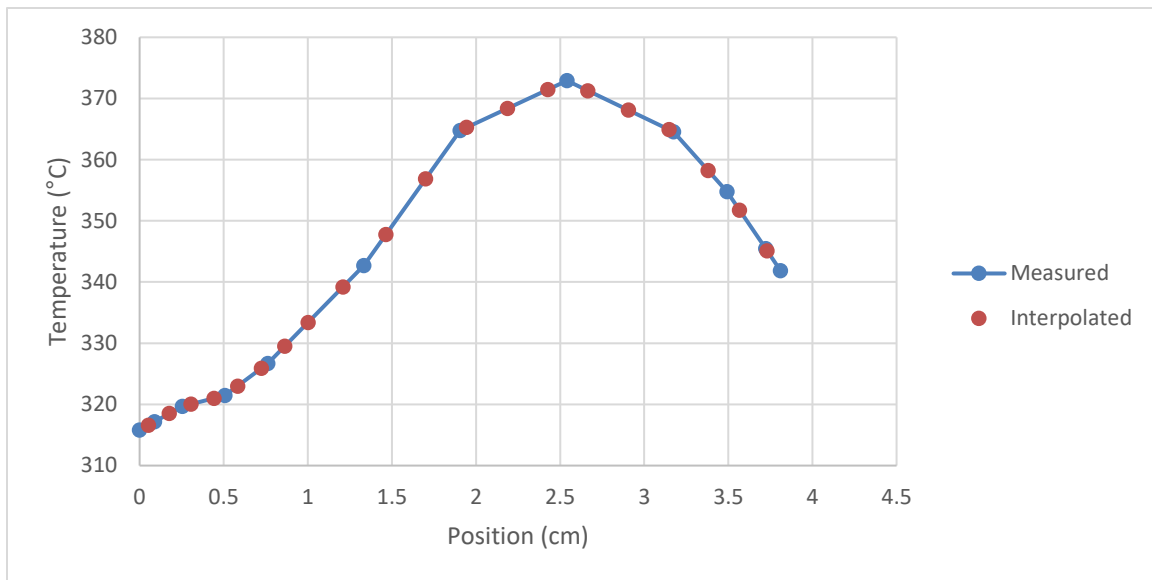


Figure A4: Specimen A55a and A55b temperature profile during annealing, as measured by the thermocouples and interpolated for each sample's midpoint.

8. References

- [1] U. E. I. Administration, "What is U.S. Electricity Generation by Energy Source?," EIA, 1 March 2019. [Online]. Available: <https://www.eia.gov/tools/faqs/faq.php?id=427&t=3>. [Accessed 1 February 2019].
- [2] J. J. Duderstadt and L. J. Hamilton, *Nuclear Reactor Analysis*, Wiley, 1976.
- [3] K. D. Kok, *Nuclear Engineering Handbook*, Boca Raton: Taylor & Francis Group, 2009.
- [4] M. Rafique, N. Mirza and S. Mirza, "Kinetic study of corrosion product activity in primary coolant pipes of a typical PWR under flow rate transients and linearly increasing corrosion rates," *Journal of Nuclear Materials*, vol. 364, no. 2-3, pp. 282-292, 2005.
- [5] H. Wang, J. Wang, T. Tan, H. Jiang, T. Cox, R. L. Howard, B. B. Bevard and M. Flanagan, "Development of U-frame bending system for studying the vibration integrity of spent nuclear fuel," *Journal of Nuclear Materials*, vol. 440, pp. 201-213, 2013.
- [6] D. O. Northwood, "The development and applications of zirconium alloys," *Materials & Design*, vol. 6, no. 2, pp. 58-70, 1985.
- [7] M. Griffiths, "A review of microstructure evolution in zirconium alloys during irradiation," *Journal of Nuclear Materials*, vol. 159, pp. 190-218, 1988.
- [8] A. T. Motta, A. Couet and R. J. Comstock, "Corrosion of zirconium alloys used for nuclear fuel cladding," *Annual Review of Materials Research*, vol. 45, pp. 311-343, 2015.
- [9] V. Tikare, P. Weck, P. Schultz, B. Clark and J. Mitchell, "Documentation of Hybrid Hydride Model for Incorporation into Moose-Bison and Validation Strategies," Sandia National Laboratories, 2014.
- [10] B. B. Bevard, J. C. Wagner, C. V. Parks and M. Aissa, "Review of Information for Spent Nuclear Fuel Burnup Confirmation," U.S. NRC, 2009.
- [11] A. T. Motta and C. Lemaignan, "Zirconium alloys in nuclear applications," *Materials Science and Technology*, vol. 10, pp. 1-51, 2006.
- [12] A. Couet, A. T. Motta and R. J. Comstock, "Hydrogen pickup measurements in zirconium alloys: relation to oxidation kinetics," *Journal of Nuclear Materials*, vol. 451, pp. 1-13, 2014.
- [13] O. Courty, A. T. Motta and J. D. Hales, "Modeling and simulation of hydrogen behavior in Zircaloy-4 fuel cladding," *Journal of Nuclear Materials*, vol. 452, no. 1-3, pp. 311-320, 2014.

- [14] C. R. Azevedo, "Selection of fuel cladding material for nuclear fission reactors," *Engineering Failure Analysis*, vol. 18, no. 8, pp. 1943-1962, 2011.
- [15] A. J. Breen, I. Mouton, W. Lu and S. Wang, "Atomic scale analysis of grain boundary deuteride growth front in Zircaloy-4," *Scripta Materialia*, vol. 156, pp. 42-46, 2018.
- [16] E. Schelzke, "Hydride orientation in Zircaloy tubes as a function of deformation texture and stresses," *Journal of Nuclear Materials*, vol. 30, p. 324, 1969.
- [17] R. S. Daum, Y. S. Chu and A. T. Motta, "Identification and quantification of hydride phases in Zircaloy-4 cladding using synchrotron radiation diffraction," *Journal of Nuclear Materials*, vol. 392, pp. 453-463, 2009.
- [18] R. S. Daum, D. W. Bates, D. A. Koss and A. T. Motta, "The influence of a hydride layer on the fracture of Zircaloy-4 cladding tubes," Argonne National Laboratories, 2002.
- [19] R. Dutton, K. Nuttall, M. Puls and L. A. Simpson, "Mechanisms of hydrogen induced delayed cracking in hydride forming materials," *Metallurgical and Materials Transactions A*, vol. 8A, pp. 1553-1562, 1977.
- [20] B. Cox and Y. M. Wong, "A hydrogen uptake micro-mechanism for Zr alloys," *Journal of Nuclear Materials*, vol. 270, pp. 134-146, 1999.
- [21] B. Cox and C. Roy, "The use of tritium as a tracer in studies of hydrogen uptake by zirconium alloys," Atomic Energy of Canada Ltd., Chalk River Nuclear Laboratories, 1965.
- [22] M. Harada and R. Wakamatsu, "The effect of hydrogen on the transition behavior of the corrosion rate of zirconium alloys," in *ASTM STP 1505 Zirconium in the nuclear Industry: 15th International Symposium*, 2008, p. 384.
- [23] D. O. Northwood and U. Kosasih, "Hydrides and delayed hydrogen cracking in zirconium and its alloys," *International Metals Reviews*, vol. 28, pp. 92-121, 1983.
- [24] J. Kearns, "Terminal solubility and partitioning of hydrogen in the alpha phase of zirconium, Zircaloy-2, and Zircaloy-4," *Journal of Nuclear Materials*, vol. 22, pp. 292-303, 1967.
- [25] B. F. Kammenzind, D. G. Franklin, H. R. Peters and W. J. Duffin, "Hydrogen pickup and redistribution in alpha-annealed Zircaloy-4," in *ASTM STP 1295 Zirconium in the Nuclear Industry: 11th International Symposium*, 1996, pp. 338-370.
- [26] A. Sawatzky, "The diffusion and solubility of hydrogen in the alpha phase of Zircaloy-2," *Journal of Nuclear Materials*, vol. 2, pp. 62-68, 1960.

- [27] C. E. Ells and C. J. Simpson, *Hydrogen in Metals*, ASM, 1974.
- [28] C. Korn and S. D. Goren, "NMR study of hydrogen diffusion in zirconium hydride," *Physical Review B*, vol. 33, pp. 68-78, 1986.
- [29] B. F. Kammenzind, B. M. Berquist, R. Bajaj, P. H. Kreyns and D. G. Franklin, "The long-range migration of hydrogen through Zircaloy in response to tensile and compressive stress gradients," in *Astm STP 1354 Zirconium in the Nuclear Industry: 12th International Symposium*, 2000, pp. 196-233.
- [30] A. McMinn, E. C. Darby and J. S. Schofield, "The terminal solid solubility of hydrogen in zirconium alloys," in *ASTM STP 1354 Zirconium in the Nuclear Industry: 12th International Symposium*, 2000, pp. 173-195.
- [31] E. Lacroix, A. T. Motta and J. D. Almer, "Experimental determinations of zirconium hydride precipitation and dissolution in zirconium alloy," *Journal of Nuclear Materials*, vol. 509, pp. 162-167, 2018.
- [32] K. Une and S. Ishimoto, "Terminal solid solubility of hydrogen in unalloyed zirconium by differential scanning calorimetry," *Journal of Nuclear Science and Technology*, vol. 41, pp. 949-952, 2004.
- [33] P. Vizcaino, A. D. Banchik and J. P. Abriata, "Solubility of hydrogen in Zircaloy-4: irradiation induced increase and thermal recovery," *Journal of Nuclear Materials*, vol. 304, pp. 96-106, 2002.
- [34] K. B. Colas, A. T. Motta, J. D. Almer, M. R. Daymond, M. Kerr and A. D. Banchik, "In situ study of hydride precipitation kinetics and re-orientation in Zircaloy using synchrotron radiation," *Acta Materialia*, vol. 58, pp. 6575-6583, 2010.
- [35] Z. L. Pan, I. G. Ritchie and M. P. Puls, "Terminal solid solubility of hydrogen and deuterium in Zr-2.5Nb alloys," *Journal of Nuclear Materials*, vol. 228, pp. 227-237, 1996.
- [36] R. S. Daum, S. Majumdar, D. W. Bates, A. T. Motta, D. A. Koss and M. C. Billone, "On the embrittlement of Zircaloy-4 under RIA-relevant conditions," in *ASTM STP 1423 Zirconium in the Nuclear Industry: 13th International Symposium*, 2002, pp. 702-718.
- [37] J. J. Kearns, "Laboratory Method for Adjusting Hydrogen Content of Zirconium, WAPD-TM-147," Bettis Plant, Pittsburgh, 1958.
- [38] A. Sawatzky, "Hydriding Zircaloy-2 by Electrolysis," Chalk River Laboratory, 1960.
- [39] A. Sawatzky, "The heat of transport of hydrogen in zirconium alloys," *Journal of Nuclear Materials*, vol. 9, p. 364, 1963.

- [40] J. D. Hales, K. A. Gamble, B. W. Spencer, S. R. Novascone and G. Pastore, Bison User Manual, Idaho National Laboratory, 2019.
- [41] D. S. Stafford, "Multidimensional simulations of hydrides during fuel rod lifecycle," *Journal of Nuclear Materials*, vol. 466, pp. 362-372, 2015.
- [42] H. Chung, M. Billone and R. V. Strain, "Characteristics of Hydride Precipitation and Reorientation in Spent-Fuel Cladding," 2000.